



HAL
open science

Development of a CMOS pixel sensor with on-chip artificial neural networks

Ruiguang Zhao

► **To cite this version:**

Ruiguang Zhao. Development of a CMOS pixel sensor with on-chip artificial neural networks. High Energy Physics - Experiment [hep-ex]. Université de Strasbourg, 2019. English. NNT : 2019STRAE050 . tel-02517257

HAL Id: tel-02517257

<https://theses.hal.science/tel-02517257>

Submitted on 24 Mar 2020

HAL is a multi-disciplinary open access archive for the deposit and dissemination of scientific research documents, whether they are published or not. The documents may come from teaching and research institutions in France or abroad, or from public or private research centers.

L'archive ouverte pluridisciplinaire **HAL**, est destinée au dépôt et à la diffusion de documents scientifiques de niveau recherche, publiés ou non, émanant des établissements d'enseignement et de recherche français ou étrangers, des laboratoires publics ou privés.

ÉCOLE DOCTORALE Physique et Chimie-Physique

Institut pluridisciplinaire Hubert Curien (IPHC) - UMR 7178

THÈSE

 présentée par :

Ruiguang ZHAO

soutenue le : 20 Décembre 2019

pour obtenir le grade de : **Docteur de l'université de Strasbourg**
Discipline/ Spécialité : Électronique, Microélectronique, Photonique

**Development of a CMOS pixel sensor
with on-chip artificial neural networks**

THÈSE dirigée par :

M. HU Yann

Professeur, Université de Strasbourg

RAPPORTEURS :

M. DE LA TAILLE Christophe

M. BERRY François

Directeur, Laboratoire OMEGA

Professeur, Institut PASCAL

AUTRES MEMBRES DU JURY :

M. PRIGENT Michel

Mme. COURTIN Sandrine

M. BESSON Auguste

Professeur, Institut XLIM

Professeur, Université de Strasbourg

Maître de Conférences, Université de Strasbourg

Contents

Contents	I
Acknowledgements	V
List of Figures.....	VII
List of Tables.....	XI
Résumé en Français	XIII
Introduction.....	XXIII
1 International Linear Collider.....	1
1.1 ILC Project.....	1
1.1.1 Physics Programs of the ILC	2
1.1.2 ILC Layout	4
1.2 ILC Experimental Conditions	5
1.2.1 Beam Structure	5
1.2.2 Beam Background	5
1.3 International Large Detector	6
1.3.1 Vertex Detector	7
1.3.2 Silicon Tracking Part	11
1.3.3 Time Projection Chamber.....	11
1.3.4 Calorimeter System	12
1.3.5 Muon System.....	12
1.3.6 Coil and Yoke System.....	12
1.4 Motivation.....	12

1.4.1	Challenges for Track Reconstruction	12
1.4.2	Trajectory of Charged Particles	14
1.4.3	Principle for Particle Recognition	17
1.5	Summary	18
1.6	Bibliography	19
2	Semiconductor Detectors	23
2.1	Carriers Generation	24
2.1.1	Carriers Generated by Photons	24
2.1.2	Carriers Generation by Charged Particles	25
2.2	Carriers Transport	26
2.2.1	Drift	26
2.2.2	Diffusion	26
2.3	P-N Junction.....	27
2.3.1	Forward Bias.....	28
2.3.2	Reverse Bias	28
2.4	Metal-Oxide-Semiconductor.....	29
2.5	Silicon Detector Types	30
2.5.1	Strip Detector.....	30
2.5.2	CCD	32
2.5.3	Hybrid Pixel Sensor.....	33
2.5.4	DEPFET Sensor.....	34
2.5.5	Monolithic Active Pixel Sensor	34
2.5.6	Conclusions	36
2.6	Summary	38
2.7	Bibliography	39
3	Artificial Neural Networks for Pattern Recognition.....	43
3.1	Pattern Recognition.....	43
3.2	Biological and Artificial Neuron.....	45
3.2.1	Biological Neurons	45
3.2.2	Artificial Neuron.....	46
3.2.3	Activation Function	47
3.3	Types of Artificial Neural Networks.....	49
3.3.1	Multi-Layer Perceptron (MLP)	50
3.4	Feature Extraction.....	51

3.5	ANN Supervised Learning.....	52
3.5.1	BP Algorithm.....	53
3.6	ANN in HEP.....	57
3.7	Challenges for ANN Implementation.....	59
3.8	Summary.....	60
3.9	Bibliography.....	61
4	FPGA Implementation of ANN for Reconstructing Incident Angles	65
4.1	Raw Data Acquisition System.....	66
4.1.1	CMOS Pixel Sensor.....	67
4.1.2	2 Rotations Support.....	68
4.1.3	Readout Chain.....	73
4.2	Implementations in the FPGA.....	74
4.2.1	Interface to Read in Raw Data.....	76
4.2.2	Cluster Search.....	79
4.2.3	Data Format Conversion.....	86
4.2.4	Feature Extraction.....	87
4.2.5	Normalized Features.....	93
4.2.6	ANN Implementation.....	93
4.2.7	DeNormalized Module.....	96
4.2.8	Interface to Output.....	97
4.3	Test results.....	99
4.3.1	Analysis and Discussion.....	100
4.4	Summary.....	102
4.5	Bibliography.....	103
5	An On-chip Algorithm for Cluster Search.....	105
5.1	Motivation.....	105
5.2	Algorithm for Cluster Search.....	106
5.2.1	Algorithm for One Column.....	107
5.2.2	Steps for a Cluster.....	110
5.2.3	Supplementary Explanation.....	112
5.3	Simulation Results.....	115
5.3.1	Cluster Windows.....	115
5.3.2	Seed Thresholds.....	117
5.3.3	Algorithm in the FPGA VS. Algorithm Proposed.....	118

5.4	Discussion	120
5.4.1	Large Clusters	120
5.4.2	Separated Parts	122
5.4.3	Overlap Parts	123
5.5	Algorithm Implementation.....	124
5.5.1	Implementation of the 64-column Algorithm.....	124
5.5.2	Timing.....	127
5.5.3	Simulation of the 256-column Implementation.....	129
5.5.4	Synthesized Result of the 64-column Implementation.....	130
5.6	Summary	132
5.7	Bibliography	133
6	Conclusions and Perspectives.....	135

Acknowledgements

I would like to thank China Scholarship Council (CSC) for the financial support during my doctoral study at University of Strasbourg, France and Institut Pluridisciplinaire Hubert Curien (IPHC), CNRS.

This thesis was made possible by the support of many individuals during my past four years in France. I would like to express my sincere gratitude to my supervisor Prof. Yann HU and Marc WINTER, the leader of the CMOS-ILC research group, for offering me the opportunity to work in IPhC. Their guidance has been helpful during my research and for writing this thesis. I sincerely appreciate Dr. Auguste BESSON for his guidance and fruitful suggestions throughout my doctoral study, the analysis of the simulation result, and providing the corrections and suggestions for this thesis.

I am grateful to Dr. Christine HU-GUO, the director of the microelectronic group, for giving me insightful guidance for my design and providing exhaustive suggestions for my publications and posters.

I would like to thank Prof. Michel PAINDAVOINE, in Electronics, Signal and Image Processing of Burgundy University, for communication and guidance at the beginning of my thesis. I would like to thank Luis alejandro PEREZ PEREZ and Mathieu GOFFE for their help in the whole process of the raw data acquisition and the ANN training. I am grateful to Kimmo JAASKELAINEN for his help in the FPGA system design. I would like to thank Claude COLLEDANI and Guy DOZIERE for providing help and offering encouragements during my doctoral period.

I would also like to thank all my colleagues in IPhC: Jerome BAUDOT, Frederic MOREL, Abdelkader HIMMI, Gregory BERTOLONE, Isabelle VALIN, Maciej KACHEL, Gilles CLAUS, Mathieu SPECHT, Christian ILLINGER, Andrei

Acknowledgements

DOROKHOV, Pham Thanh HUNG and Yu ZHANG for their kind help and technical support in my work.

I would like to express my respect to doctoral candidates, Julian HEYMES and Yue ZHAO, of our group. We got together to share ideas, discussed processes and analysed results.

I am so appreciated to my friends Jiahui FAN, Siyu LU who gave me faithful supports during the whole stage of my thesis.

Last but not least, I would like to thank my parents for raising me and making me be surrounded by unconditional support, understanding and love. I am very grateful to my future girlfriend, thanks for her absence during my doctoral period and did not hurt my heart.

List of Figures

Figure 1: International Grand Detector (ILD) et Silicon Detector (SiD).	XIV
Figure 2: Les formes de cluster générées par des particules du processus physique VS. l'arrière-plan de faisceau.....	XV
Figure 3: L'ANN implémentée dans le FPGA.....	XVI
Figure 4: . Le résultat du test de 500 trames de données brutes dans chaque angle d'incidence donné.	XVII
Figure 5: La description de la procédure de l'algorithme.	XIX
Figure 6: Structure de l'algorithme implémenté dans une matrice à 64 colonnes.	XX
Figure 1.1: Schematic layout of the ILC in the 250 GeV staged configuration [18].....	4
Figure 1.2: Beam structure of the ILC.....	5
Figure 1.3: Illustration of the pinch effect and generation of beamstrahlung photons in bunch collisions.....	6
Figure 1.4: Two detectors and the "push-pull" mode [25].....	7
Figure 1.5: Quadrant view of the ILD detector concept. Dimensions are in mm [26].	7
Figure 1.6: Impact parameter resolution (a) Finite single point resolution (b) Multiple scattering.	8
Figure 1.7: Impact parameter resolution as a function of the particle momentum.....	9
Figure 1.8: Vertex detector scheme of the ILD.	10
Figure 1.9: ILD schemes of the silicon tracking system.	11
Figure 1.10: Beam background features simulation [29].	13
Figure 1.11: Schematic diagram of tracks generated by particles, one is created by a particle with high momentum (blue) and others are created by particles with low momenta.	13
Figure 1.12: Helix trajectory of charged particles under the effect of the magnetic field.	14
Figure 1.13: Trajectory projection of a charged particle on the transverse plane.....	14
Figure 1.14: Incident angle θ_T as a function of the particle transverse momentum (P_T).	16
Figure 1.15: Trajectory projection of a charged particle on the parallel plane.....	17
Figure 1.16: Schematic diagram of an incident angle on the vertex detector.....	17
Figure 1.17: Cluster shapes generated by particles from the physics process and particles from the beam background.....	18

Figure 2.1: Typical semiconductor detector system.	23
Figure 2.2: Generation of electrons and holes by absorption of photons, the energy loss= E_g , $>E_g$, and $<E_g$ [5]......	25
Figure 2.3: P-N junction (a) Depletion region (b) Energy band diagram.....	27
Figure 2.4: P-N junction under forward bias (a) Depletion region (b) Energy band diagram.	28
Figure 2.5: P-N junction under reverse bias (a) Depletion region (b) Energy band diagram.	28
Figure 2.6: N-type Metal-Oxide-Semiconductor structure.....	29
Figure 2.7: An n-type MOS under accumulation, depletion and inversion conditions [10]..	29
Figure 2.8: Single-sided strip detector (a) DC coupled strip detector (b) AC coupled strip detector [13].	31
Figure 2.9: Operation principle of a double-sided strip detector [17].	32
Figure 2.10: Timing diagram of voltage schemes to transport charge through a three-phase CCD.....	32
Figure 2.11: A simplified schematic diagram of a single pixel in a hybrid silicon detector, it is composed of a sensor part and a readout electronics part [24]......	33
Figure 2.12: Schematic layout of the DEPFET [27].	34
Figure 2.13: Schematic of the first-generation MAPS structure.	35
Figure 2.14: Schematic of the second-generation MAPS structure.....	35
Figure 2.15: Typical in-pixel readout circuit [30].	36
Figure 3.1: Examples of cluster shapes (a) Cluster shape generated by charged particles from the physics event (b) Cluster shape generated by charged a charged particle from the beam background.	44
Figure 3.2: Connections between two biological neurons.....	45
Figure 3.3: Computational model of artificial neurons.	46
Figure 3.4: McCulloch-Pitts model of an artificial neuron.	47
Figure 3.5: Sigmoid activation functions.	48
Figure 3.6: Taxonomy of feedforward and feedback network architectures [13].	49
Figure 3.7: Connection architectures of Multi-Layer Perceptron.....	50
Figure 3.8: Training and test phase [25]......	52
Figure 3.9: Signal-flow graph of output neuron j.....	55
Figure 3.10: Signal-flow graph of hidden neuron j.	56
Figure 3.11: Basic coincidence electric circuit.....	58
Figure 4.1: Main procedures of the offline methodology. The training and the test process in TMVA have been accomplished by my colleague Luis alejandro PEREZ PEREZ.	65
Figure 4.2: Schematic diagram of the raw data acquisition system.	66
Figure 4.3: CMOS pixel sensor MIMOSA 18 (a) Layout of MIMOSA 18 (b) The pixel structure of the MIMOSA18 [3]......	67
Figure 4.4: Schematic of the 2 rotations support.....	68
Figure 4.5: Simulation result of the correlation between incident angle φ , θ and α , β	72
Figure 4.6: Schematic diagram of the MIMOSA 18 readout chain [4].	73
Figure 4.7: FPGA development board (Nexys Video Artix-7 FPGA) used in our study.....	74
Figure 4.8: Main procedures and timing in the FPGA device.	75

Figure 4.9: Frame format stored in a binary file (256×256 pixels).	77
Figure 4.10: Timing waveform to read in raw data of an example from PC to the FPGA device.	79
Figure 4.11: Incident angles of charged particles.	80
Figure 4.12: Algorithm for cluster search implemented in the FPGA device.	81
Figure 4.13: Steps of searching neighbour pixels around seed pixel.	82
Figure 4.14: Cluster counts found by algorithms with different cluster windows.	84
Figure 4.15: Cluster counts of an elongated cluster found by the three algorithms.	85
Figure 4.16: Simulation of cluster counts and effective surface.	85
Figure 4.17: Format of Single-precision floating-point [10].	86
Figure 4.18: Stopping power for positive muons in copper Straggling functions in silicon for 500MeV pions, normalized to unity at the most probable value $\Delta p/x$ [12].	88
Figure 4.19: The main axis of a cluster.	88
Figure 4.20: Position of a fired pixel in a cluster.	90
Figure 4.21: Correlation between two coordinate systems.	91
Figure 4.22: Structure of the artificial neural network.	93
Figure 4.23: Digital circuit of the artificial neural network.	95
Figure 4.24: Reconstructed information format of a cluster.	97
Figure 4.25: Timing of transporting the output result of one memory cell.	98
Figure 4.26: Reconstructed results of a frame of raw data (a) The content of reconstructed results (b) First cluster shape (c) Second cluster shape.	99
Figure 4.27: Difference between the mean value of reconstructed angles and the incident angle.	100
Figure 4.28: Distribution of reconstructed angles θ_{rec} versus incident angles θ_{inc} .	101
Figure 5.1: Definition of a seed pixel in a cluster.	107
Figure 5.2: Flowchart of the algorithm proposed.	108
Figure 5.3: Comparison between the data [3] and the max_value register.	109
Figure 5.4: Comparison between the column seed pixel and the neighbour max_value registers.	109
Figure 5.5: Information of an example cluster.	110
Figure 5.6: Processing steps of the example cluster.	111
Figure 5.7: Two "seed pixels" in the same column, pixel A is the seed pixel, pixel B is a part of the cluster.	114
Figure 5.8: Two "seed pixels" in the same row, pixel A is the seed pixel, pixel B is a part of the cluster.	114
Figure 5.9: Simulation results of cluster counts found by algorithms proposed in this chapter with different cluster windows (7×7 and 5×5 cluster window).	116
Figure 5.10: Simulation results of the percentage of lost cluster counts between algorithms with the 7×7 and the 5×5 cluster window.	117
Figure 5.11: Simulation results of cluster counts by algorithms with different seed thresholds.	118
Figure 5.12: Simulation results of cluster counts found by the algorithm proposed VS.	

implemented in the FPGA device.....119

Figure 5.13: Example of a large cluster in a matrix of 7×9 pixels. 121

Figure 5.14: Example of separated parts in a matrix of 7×7 pixels..... 122

Figure 5.15: Example of overlap parts in a matrix of 8×7 pixels..... 123

Figure 5.16: Schematic of the algorithm implemented in 64 columns..... 125

Figure 5.17: Implementation of the cluster search unit..... 126

Figure 5.18: Timing of generating two seed pixels at one row..... 128

Figure 5.19: Simulation of cluster counts found by the algorithm with different modules.. 129

Figure 5.20: Schematic of MCA and ANN modules implemented for modules of the 32-column matrix. 131

Figure 6.1: Schematic diagram of a seed pixel in a 3×3 cluster window. A cluster is composed of one seed pixel (P0) and 4 fired pixels. Two possible seed pixels (P0 and P1) are compared with their 8 neighbours in the 3×3 cluster window. Due to charge of P1 is fewer than P0, just pixel P0 is defined as a seed pixel in the 3×3 cluster window..... 141

Figure 6.2: Schematic diagram of a seed pixel in a 5×5 cluster window. Charges of the 3 fired pixels in the 3×3 cluster window are replaced by seed pixel charge. Processed by step 4, charges of the fired pixels are larger than their neighbours, pixel P0 is extracted as the seed pixel in the 5×5 cluster window. 141

Figure 6.3: Schematic structure of a pixel for cluster search. 142

Figure 6.4: Steps of on-chip feature extraction. 142

Figure 6.5: Example of on-chip feature extraction. The convolution operation is processed between the four operators and a cluster at a step of 2 pixels. Four submatrices are created and presented in level 1. The convolution operation is processed again between the four operators and these submatrices at a step of 1 pixel. 16 values are produced in level 2. Convolution procedures of three values in submatrix in level 1 is shown. 143

List of Tables

Table 1-1: Major physics processes to be studied by the ILC [17].	3
Table 1-2: Parameter a and b for detectors.	9
Table 1-3: Parameters of the design composed of three layers of double-sided ladders [26].	10
Table 1-4: Minimum transverse momentum of a particle to arrive different layers (R_{layer} is the radius of the vertex detector and R is the radius of the particle trajectory).	15
Table 2-1: Advantages and disadvantages of these detector technologies [6].	37
Table 4-1: The setting of the angle θ , φ , and α , β .	73
Table 5-1: Simulation results of the occupied surface and power consumption of the 64-column implementation.	130

Résumé en Français

A. Introduction

Le modèle standard de la physique des particules est un cadre théorique utilisé pour décrire les particules fondamentales constituant la matière ordinaire et les forces fondamentales. Les expériences de physique des hautes énergies (HEP) sont conçues pour rechercher des particules fondamentales via des collisions parmi une grande quantité de particules de haute énergie. Divers détecteurs sont équipés autour du point d'interaction pour détecter et enregistrer les informations relatives aux collisions. L'ILC (International Linear Collider) est un projet d'accélérateur linéaire de particules proposé pour les expériences HEP, en complément du LHC (Large Hadron Collider) au CERN. En raison de leur courte durée de vie, de l'ordre de plusieurs picosecondes, les quarks lourds doivent être reconnus par les trajectoires partant du vertex de la décroissance secondaire. Le détecteur de vertex (VTX) sera situé près du point d'interaction.

Dans les expériences HEP, différents types de détecteurs à semi-conducteurs ont été utilisés pour la détection et la mesure de la position du passage des particules. Les capteurs à pixels CMOS (CPS) également appelés capteurs monolithiques à pixels actifs (MAPS) et proposés par des chercheurs de l'IPHC-Strasbourg (Institut Pluridisciplinaire Hubert Curien), intègrent sur un même substrat l'électronique pour la détection et la lecture des signaux. Les CPS constituent un candidat naturel pour l'équipement du VTX, car ils offrent un très bon compromis entre la granularité, le budget de matière, la tolérance au rayonnement et la vitesse de lecture. Ils ont été utilisés pour la jouvence du détecteur PiXeL (PXL) de l'expérience STAR au RHIC et

sont actuellement en phase de production pour la mise à jour de l'ITS (Inner Tracking System) de l'expérience ALICE-LHC. Comme le montre la figure 1, Le point d'interaction est entouré de deux détecteurs , (International Grand Detector (ILD) et Silicon Detector (SiD)), qui fonctionnent selon un schéma push-pull pour partager la même luminosité.

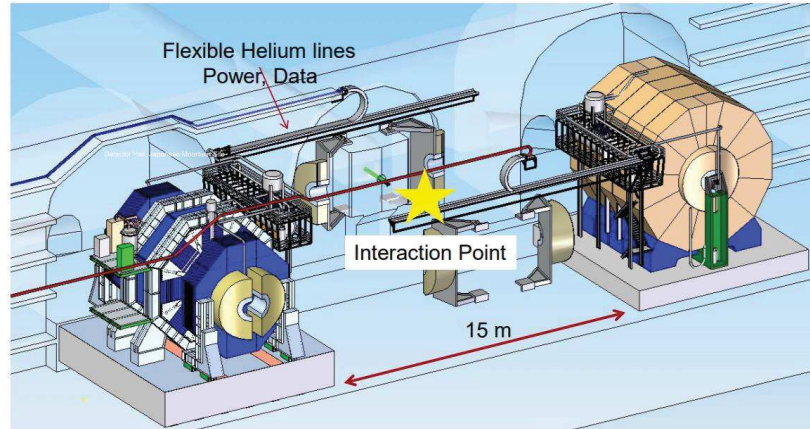


Figure 1: International Grand Detector (ILD) et Silicon Detector (SiD).

Dans le détecteur de vertex de l'ILC, la simulation Monte-Carlo montre qu'un nombre élevé d'impacts supplémentaires seront générés par des électrons résultant de processus liés au bruit de fond des faisceaux. Leur impulsion se trouve typiquement dans la gamme de 10-100 MeV/c, et est généralement à celle des particules issues d'événements associés à des processus physiques.

Sous l'effet du champ magnétique dans le détecteur, les électrons provenant du bruit de fond, en raison de leur faible impulsion, traversent les détecteurs avec un grand angle d'incidence par rapport à la normale au plan des détecteurs. Les paires électrons-trous, environ ~ 80 e-h/ μm , sont créées par le processus d'ionisation lorsque les particules chargées traversent la couche épitaxiale. Les électrons sont collectés par la diode de collection implantée dans chaque pixel. Les amas de pixels (clusters) générés par les électrons issus du bruit de fond présentent des formes plutôt allongés comme le montre la figure 2. En considérant les réseaux neuronaux artificiels (ANNs) qui ont été largement utilisés dans le domaine de la reconnaissance de motifs, notre groupe à l'IPHC a proposé d'explorer le concept d'un capteur à pixels CMOS avec des ANNs intégrés pour marquer et supprimer les pixels touchés (hits) générés par ces électrons.

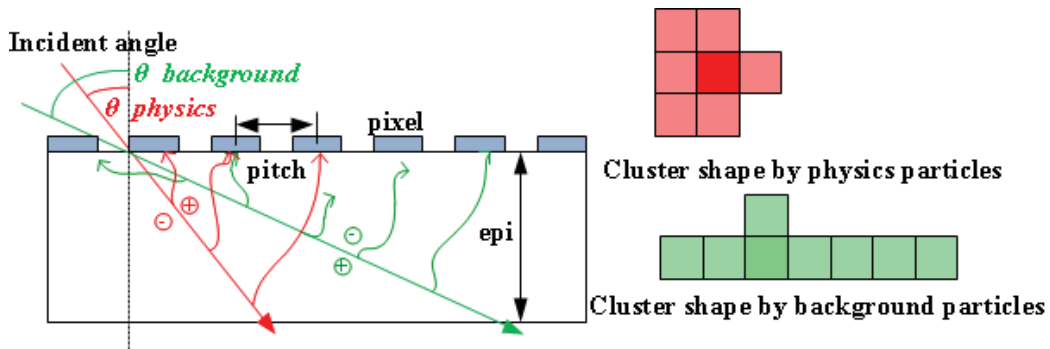


Figure 2: Les formes de cluster générées par des particules du processus physique VS. l'arrière-plan de faisceau.

Au cours de ma thèse de doctorat, je me suis concentré sur l'étude d'un capteur à pixels CMOS avec des ANNs intégrés portant sur les aspects suivants :

- I. L'implémentation de modules de prétraitement et d'un ANN dans un composant FPGA pour l'étude de faisabilité ;
- II. Un algorithme pour la recherche de clusters, qui fait partie des modules de prétraitement, a été proposé en vue d'être intégré dans la conception de l'ASIC (Application-Specific Integrated Circuit).

B. Travail Doctoral

1) L'implémentation dans un FPGA

Pour concevoir le capteur à pixels CMOS avec des réseaux neuronaux artificiels intégrés, la première étape est l'étude de faisabilité qui consiste à comparer la mise en œuvre de l'ANN dans le FPGA à celui mise en œuvre dans un software. Les deux implémentations sont exploitées par une méthode offline, ce qui signifie que les données brutes utilisées sont acquises par un système indépendant.

Le système d'acquisition de données brutes a été mis en place pour recueillir des données brutes à partir d'un capteur existant, MIMOSA 18, illuminé par une source β^- de ^{90}Sr . Un support à 2 rotations est utilisé pour placer le CPS. Dans le cas où la source serait fixe, l'angle θ d'incidence des particules chargées peut être choisi en ajustant les angles entre le support et le plan de référence.

Dans la procédure d'apprentissage effectuée par le logiciel appelé Toolkit for Multivariate Data Analysis (TMVA), une grande quantité de données brutes a été recueillie pour chaque angle θ d'incidence donné (10 au total) afin de former les poids

de l'ANN.

Pour l'implémentation de l'ANN dans le FPGA, j'ai déterminé d'abord les entrées de l'ANN en utilisant des modules de prétraitement. Ensuite, j'ai implémenté ces modules de prétraitement et l'ANN dans une carte de développement NEXYS VIDEO FPGA en utilisant le langage de description matérielle. La procédure de test a été accomplie dans le FPGA. 500 trames de données brutes ont été échantillonnées pour chaque angle d'incidence donné afin de tester l'ANN. Les données brutes ont été introduites dans le FPGA puis traitées par CDS (Correlated Double Sampling) et des valeurs de pixel de 12 bits sont générées.

a. Modules de prétraitement

Les modules de prétraitement contiennent principalement la recherche de clusters et l'extraction de paramètres. Le module de recherche de clusters est utilisé pour trouver les pixels de départ et localiser les clusters dans la trame des valeurs de pixels. Les modules d'extraction de fonctionnalités sont utilisés pour produire des paramètres caractérisant un cluster. Quatre paramètres sont définis : la charge totale d'un cluster, la charge d'un pixel de départ, les écarts-types maximum et minimum. Le module MCA (Main Component Analysis) fait partie de l'extraction des fonctionnalités implémenté dans le FPGA et est utilisé pour calculer les écarts-types maximum et minimum.

b. ANN

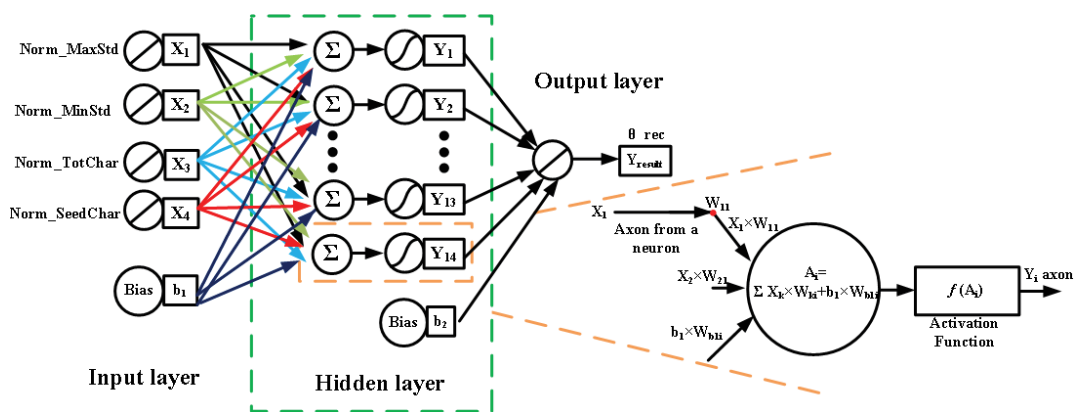
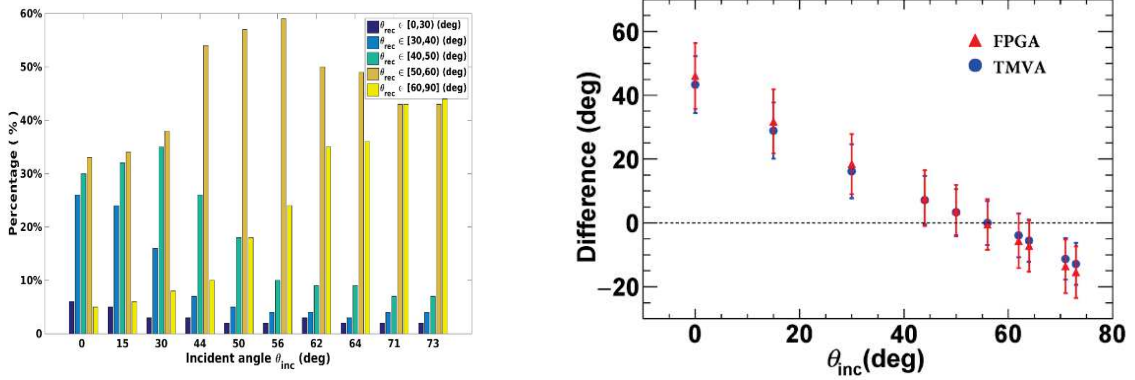


Figure 3: L'ANN implémentée dans le FPGA.

Ces quatre paramètres sont normalisés puis introduits dans l'ANN pour reconstruire l'angle d'incidence en fonction des poids de l'ANN. La structure de l'ANN est illustrée sur la figure 3. Elle se compose de la couche d'entrée, de la couche cachée

et de la couche de sortie. La couche d'entrée est composée de 4 neurones d'entrée et d'1 neurone de biais. La couche cachée qui vient après celle d'entrée a 14 neurones de calcul et 1 neurone de biais. Le nombre de neurones de la couche cachée est déterminé par la procédure d'apprentissage dans le software, en prenant en compte un équilibre entre la complexité et les performances de la structure de l'ANN. La fonction d'activation utilisée dans l'ANN est une tangente hyperbolique.

c. Résultats



(a). La distribution de l'angle reconstruit θ_{rec} par le FPGA.

(b). La différence entre la valeur moyenne des angles reconstitués ($\overline{\theta_{rec}}$) et l'angle incident θ_{inc} .

Figure 4: . Le résultat du test de 500 trames de données brutes dans chaque angle d'incidence donné.

Dans la procédure de test, j'ai enregistré et analysé les angles d'incidence reconstruits. La figure 4(a) présente la distribution des angles reconstruits (θ_{rec}). Au fur et à mesure que l'angle d'incidence (θ_{inc}) augmente, le pourcentage d'angles reconstruits (θ_{rec}) entre 60 et 90 degrés augmente alors que le pourcentage d'angles reconstruits (θ_{rec}) entre 30 et 50 degrés diminue. Compte tenu de l'application spécifique du détecteur, la gamme d'angles reconstruits d'intérêt est comprise entre 50 à 75 degrés. Tout d'abord, les formes de clusters générées par des particules d'angles d'incidence inférieurs à 50 degrés ne varient évidemment pas ou très peu. De plus, ces angles d'incidence peuvent être directement reconstruits à partir des informations des hits données par une échelle double-face (double-sided ladder). D'autre part, en raison de la limitation de la fenêtre 7×7 , les entrées ANN extraites des clusters présentent des caractéristiques similaires si l'angle d'incidence est supérieur à 78 degrés.

La figure 4(b) représente la différence « D », voir dans la formule (1), entre la valeur moyenne des angles reconstruits ($\overline{\theta_{rec}}$) et l'angle d'incidence (θ_{inc}) ; notons que

les résultats reconstruits par le FPGA sont présentés en rouge et ceux reconstruits par le logiciel TMVA en bleu. On remarque que les angles reconstruits par les deux méthodes ont la même valeur moyenne, ce qui valide l'étude de faisabilité. Cependant, ils ne coïncident pas complètement en raison de la différence dans la précision des données entre le hardware et le software.

$$D = \overline{\theta_{rec}} - \theta_{inc} = \frac{1}{n} \sum_{i=1}^n (\theta_{rec_i}) - \theta_{inc} . \quad (1)$$

De plus, les différences entre $\overline{\theta_{rec}}$ et θ_{inc} , que ce soient pour le FPGA ou pour le TMVA, n'ont pas encore atteint un niveau de précision permettant de prédire l'angle d'incidence réel car la structure de l'ANN et la procédure de formation doivent encore être optimisées. Idéalement, la différence entre $\overline{\theta_{rec}}$ et l'angle d'incidence (θ_{inc}) devrait se situer près de l'axe X ($y=0$).

Même si l'ANN n'a pas permis une reconstruction très précise, comme indiqué, les résultats reconstruits présentent clairement la même tendance que la variété d'angles d'incidence. En outre, la preuve du principe que les particules laissent une "signature" qui dépend de l'angle d'incidence a été établie.

2) Un algorithme sur l'ASIC pour la recherche de cluster:

Le module de recherche de cluster implémenté dans le FPGA ne peut pas être transplanté directement dans la conception ASIC. En premier lieu, un grand nombre de mémoires serait nécessaire pour stocker une trame entière de valeurs de pixels; en second lieu, beaucoup de ressource calcul et de temps seraient nécessaires pour détecter les pixels voisins. J'ai proposé propose un algorithme pour la recherche de cluster qui peut être intégré dans le capteur à pixels CMOS et collecter des clusters en temps réel.

a. Algorithm

Au lieu de rechercher des pixels de départ dans une matrice pixel par pixel, l'algorithme recherche un pixel de départ en temps réel dans le processus de lecture de la valeur de pixel ligne par ligne. Le pixel de départ est admis en comparant les pixels situés au-dessus et en dessous de celui-ci et les pixels les plus grands situés dans les colonnes gauche et droite d'une certaine plage de fenêtres. La procédure de l'algorithme est illustrée à la figure 5.

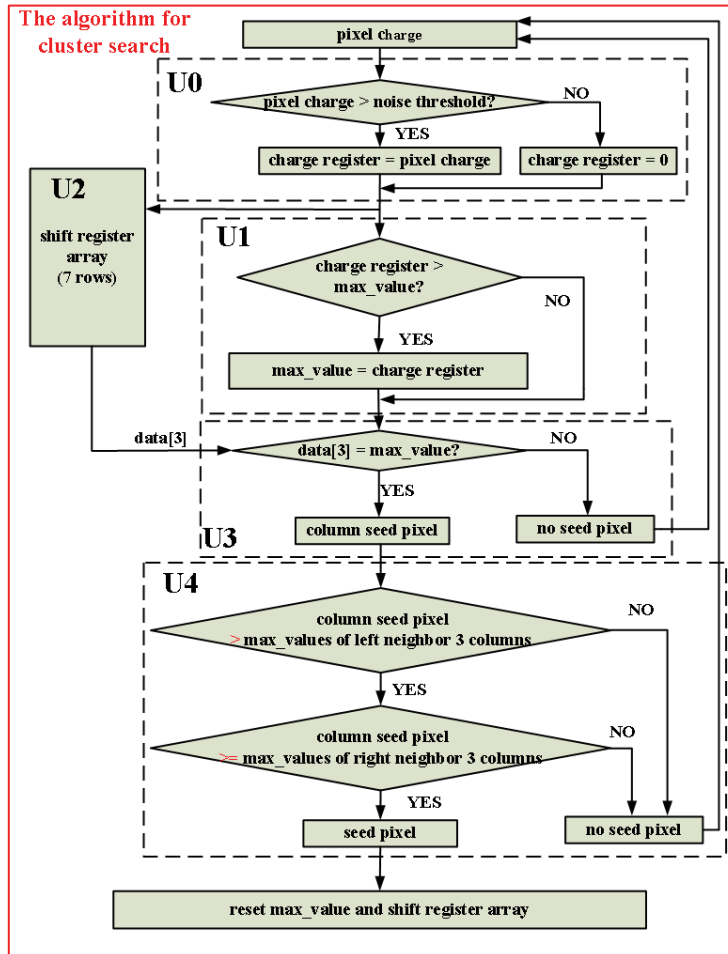


Figure 5: La description de la procédure de l'algorithme.

b. Simulation

J'ai élaboré l'algorithme en code C et l'ai simulé. 500 trames de données brutes pour chaque angle d'incidence donné sont utilisées pour tester ces algorithmes. Le résultat montre que l'algorithme atteint le même niveau de comptage des clusters que les autres algorithmes, y compris celui implémenté dans le FPGA.

c. Implémentation

La mise en oeuvre de l'algorithme est basée sur une matrice à modulo 2^N -colonnes. La figure 6 montre un exemple de deux modules de 32 colonnes ($N=5$). Les entrées de l'implémentation sont les sorties des 64 ADC de colonne. Le niveau 1 se compose de 32 unités, chacune implémentant l'algorithme de recherche de cluster. Le niveau 2 a sept (pour la fenêtre de 7×7) multiplexeurs 32-1. Le nombre de multiplexeurs est déterminé par la taille de la fenêtre dans l'algorithme.

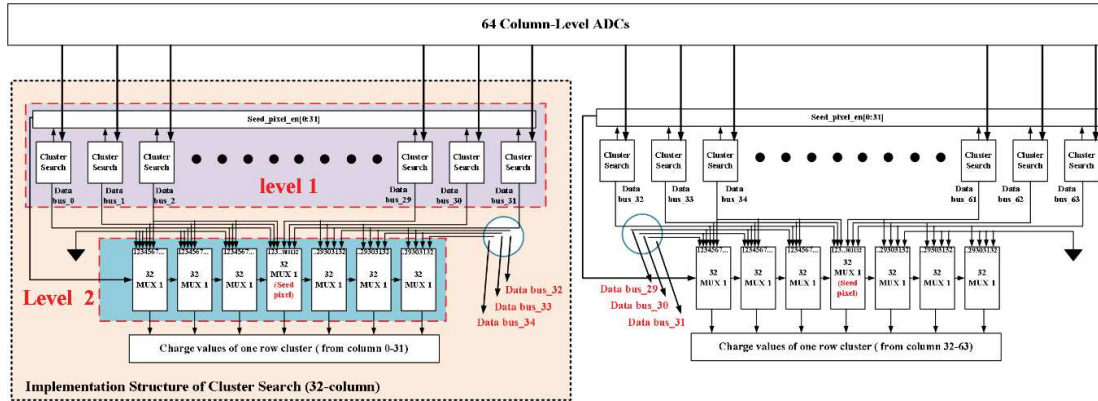


Figure 6: Structure de l'algorithme implémenté dans une matrice à 64 colonnes.

J'ai implémenté la structure à 64 colonnes avec différents paramètres et effectué la synthèse de ces implémentations en ciblant la technologie CMOS TowerJazz 0,18 μm . Il n'y a pas de différence significative entre les implémentations dans une matrice à modulo de 16 colonnes ($N=4$), 32-colonnes ($N=5$) et 64 colonnes ($N=6$) en termes de surface occupée et de puissance dissipée. Toutefois, compte tenu de l'extraction des fonctionnalités et du module ANN qui suivent la mise en œuvre de la recherche de cluster, une surface occupée et une dissipation de puissances accrues sont nécessaires si le modulo de 16 colonnes est utilisé. Ces deux paramètres d'évaluation peuvent être diminués en utilisant la fenêtre de 5×5 au lieu de celle de 7×7 . Ceux-ci pourraient encore être améliorés avec une horloge à basse fréquence ou un ADC de basse résolution. Si l'on choisit la technologie CMOS 65 nm, la densité d'intégration augmente impliquant une diminution de la surface occupée et de la puissance consommée. Si l'on utilise un substrat présentant une couche épitaxiale de haute résistivité, une fenêtre de cluster plus petite peut alors être utilisée car les formes de cluster générées par les particules sont réduites.

C. R&D

Sur la base des recherches de la thèse, le concept d'un capteur à pixels CMOS avec des ANNs intégrés sera étudié plus avant en mettant l'accent sur les deux aspects suivants :

Optimiser l'ANN pour améliorer la précision de reconstruction:

L'architecture ANN doit être optimisée, telle que le nombre de neurones d'entrée. Plusieurs fonctionnalités peuvent être introduites pour présenter un cluster. L'ANN pourrait recevoir en entrée davantage de données brutes pour optimiser les poids afin

d'accroître la précision de la reconstruction.

Développer des modules fonctionnels sur puce pour réaliser la conception matérielle complète

Une solution pour diminuer la dissipation de puissance de cette conception sera d'optimiser le système de contrôle grâce à la technique dite de Power Gating qui permet de couper l'alimentation des modules non utilisés. Pour la couche épitaxiale à haute résistivité, la consommation d'énergie et les surfaces occupées du module seront réduites grâce à l'application d'une petite fenêtre en clusters (5×5). En plus, un algorithme sera proposé pour l'extraction des paramètres des clusters et intégré dans l'ASIC.

Si la technologie CMOS 65 nm est utilisée à l'avenir, la surface occupée sera réduite car une densité de circuit plus élevée est fournie; une réduction significative de la consommation d'énergie pourra être obtenue en raison de la faible source de courant. La technologie d'intégration 3D pourrait également être appliquée pour intégrer des ANN dans le capteur à pixels CMOS. La matrice de pixels et les modules de traitement numérique (recherche de cluster, extraction de caractéristiques et ANN) pourraient alors être séparés en différents niveaux.

Introduction

High Energy Physics (HEP) experiments are established to extend and improve the understanding of the universe. In machines of HEP experiments, physics particles are accelerated and then taken into collisions. Various detectors equipped are used to record and measure the products of the collisions. The International Linear Collider (ILC) as a complementary experiment to the Large Hadron Collider (LHC) has been proposed. The current program of the ILC for a 125 GeV Higgs boson will be processed at a centre-of-mass energy of 250 GeV. The International Large Detector (ILD) and the Silicon Detector(SiD) are two detector concepts that will be installed around the interaction point and operated in a push-pull scheme to share the same luminosity. Vertex detectors are located at the most inner part of a detector to measure the primary interaction vertex and secondary vertices from decay particles under cooperation from other tracking detectors. The vertex detector of the ILD consists of a cylindrical concentric multi-layer structure to achieve an excellent spatial point resolution. On the vertex detector, a large number of hits will be generated by electrons coming from the beam background. These extra hits will increase the data flow and reduce the bandwidth of the system. The momentum of these electrons coming from the beam background typically lie in the range of 10-100 MeV/c, which is lower than that of particles coming from physics events. Due to the effect of multiple scattering, the reconstruction of tracks generated by low momentum particles is significantly degraded.

In order to tag and remove the extra hits generated by background particles, this thesis aims to make contributions to the development of a CMOS pixel sensor with on-chip artificial neural networks.

Electron-hole pairs about ~ 80 e-h/ μm are created by the ionization process when a charged particle passes through the epitaxial layer of CMOS pixel sensors. Because of diffusion, electrons generated are collected by two or more independent pixels that constitute a charge cluster which expresses hit information. Under the effect of the magnetic field in the detector, electrons from the beam background, owing to low momenta, will cross the vertex detector with a large incident angle. Clusters generated by these electrons (large incident angles) present rather elongated shapes.

CMOS pixel sensors (CPS), also named Monolithic Active Pixel Sensors (MAPS) are monolithic devices that integrate signal sensing and readout electronics on the same substrate. They offer an attractive balance among granularity, material budget, radiation tolerance and readout speed. CMOS pixel sensors have been used in the PiXeL detector (PXL) upgrade of the STAR experiment at RHIC and now are being built for the upgrades of the Inner Tracking System (ITS) of the ALICE-LHC experiment.

Artificial Neural Networks (ANNs) are computational modules that are inspired by the biological neural network. An ANN consists of processing units and connections between these units. It has been proved that ANNs are suitable for pattern recognition in a wide variety of field.

In this thesis, we study the feasibility of integrating ANNs within CPS to reconstruct incident angles of particles. In addition, an algorithm for cluster search is proposed to integrate into the CPS for real-time preprocessing.

The thesis is organized as follows,

- In chapter 1, ILC physics processes and layout are introduced briefly. Then, major experimental conditions including beam structure and beam background are presented. ILD, especially the vertex detector part, is presented. Finally, due to challenges existing for multi-layer vertex detector targeting at low momentum particles, the motivation of a CMOS pixel sensor with on-chip artificial neural networks is provided. The trajectory of charged particles under the effect of the magnetic field is projected on both the transverse and parallel plane respectively and described.
- In chapter 2, the principle of carriers generation and transport in semiconductors are introduced. Then, structures and bias modes of P-N junctions and Metal-Oxide-Semiconductors are expressed. Lastly, several types of silicon detectors are presented and compared.
- In chapter 3, pattern recognition is introduced firstly. The biological and

artificial neuron structure and principle are explained. Then, a multi-layer perceptron structure is presented. Next, the feature extraction procedure and supervised learning procedure of ANN is outlined. ANN' applications in the HEP are presented.

- In chapter 4, the feasibility study of the CMOS pixel sensor with on-chip ANNs, which is achieved by the off-line method, is described in detail. Firstly, a raw data acquisition system, including CMOS pixel sensor, 2 rotations support and readout china is illustrated. Then, the entire design implemented in a Field Programmable Gate Array (FPGA) development board is introduced in detail, including the cluster search module, the feature extraction module and the ANN structure. Lastly, the reconstruction results of incident angles by the ANN are compared and analysed.
- In chapter 5, an on-chip algorithm for cluster search is proposed and presented. Firstly, the motivation for the algorithm is given. Secondly, the algorithm is illustrated in detail, including the principle description and detail step demonstration. Then, simulation results are presented. Next, the discussion of the algorithm is provided targeting at three cases of the cluster shape. Finally, the implementation of the algorithm is expressed and the synthesized result of the implementation is analysed.
- In conclusions, the results obtained in this thesis are summarized. In the end, perspectives for the CPS integrated with ANNs are presented, including an in-pixel algortihm for cluster search and an structure for feature extraction.

1 International Linear Collider

The ILC was proposed for the High Energy Physics (HEP) and encouraged by requirements on the precision measurement of the Higgs Boson. The International Linear Collider (ILC) is introduced briefly in the chapter, and the development motivation of a CMOS Pixel Sensor (CPS) with on-chip Artificial Neural Networks (ANNs) is also illustrated. Firstly, physics programs and the baseline of the ILC are presented. Secondly, ILC experimental conditions and the International Large Detector (ILD) are illustrated. The chapter ends with a description of the motivation for developing a CMOS pixel sensor with on-chip ANNs, that is tagging and removing hits generated by charged particles coming from the beam background based on the cluster shapes.

1.1 ILC Project

Everything in the universe is found to be made from fundamental particles. A lot of scientists are devoted to experimental and theoretical efforts, in order to explore the nature of fundamental particles. The Standard Model (SM) is a theoretical framework, which is proposed to explain the principle of fundamental particles constituents of ordinary matter and related forces (including electromagnetic, weak, and strong interactions, excepting the gravitational force). The current Standard Model was finalized in the early 1970s, which has explained almost all results of HEP experiments to date. For instance, the model has forecast the existence of quarks, the top quark, and the tau neutrino and been confirmed. The Standard Model has become established as a

well-tested physics theory [1][2].

HEP experiments are designed to research fundamental particles via collisions and conversion among a large amount of high-energy particles. In machines, two beams of particles are moved in opposite directions and accelerated, then brought into collisions at the interaction point. Various detectors are equipped around the interaction point to detect and record information of collisions [3][4].

In the past, a large number of high energy physics experiments and equipment have been designed and established by physicists [5]. In 2012, a particle with a mass of about 125GeV was discovered by the ATLAS and CMS Collaborations at the Large Hadron Collider (LHC) which is located at Geneva Switzerland [6]. Many properties of the particle are in accordance with the postulated Higgs boson of the Standard Model. Details of the Higgs boson and the presence or not of other anticipated new particles need to be studied to complete the Standard Model framework. More precise measurements of the Higgs boson can be achieved by lepton colliders which provide the well-defined initial state of collisions and clean background level [7][8][9][10].

In 2001, a common conclusion was proposed by all three regional organizations (ACFA in Asia, HEPAP in North America, and ECFA in Europe) of the HEP field: The next major project in the HEP would be an electron-positron linear collider with a centre-of-mass energy of 500 GeV named International Linear Collider [11][12]. In autumn 2012, the Japanese high-energy physics community proposed to locate the ILC in Japan. In 2013, after the discovery of the Higgs boson, the Technical Design Report (TDR) for the ILC accelerator was published. The machine was designed to achieve a centre-of-mass energy of 500 GeV [13][14].

According to the recommendation from the Japan Association of High Energy Physicists (JAHEP) [15], the initial program of the ILC for a 125 GeV Higgs boson would be started with a centre-of-mass energy of 250 GeV [7]. The ILC project is divided into three phases, the preparation phase (2019/20-2022/2023), the construction phase (foreseen from 2023) and the commissioning phase (foreseen 2031-2032) [16].

1.1.1 Physics Programs of the ILC

Major physics processes to be studied at various centre-of-mass energies (from 90 GeV to 1000 GeV) in the ILC are shown in table 1-1, Standard Model reactions and physics goals are presented.

Table 1-1: Major physics processes to be studied by the ILC [17].

Energy	Reaction	Physics goal
91 GeV	$e^+e^- \rightarrow Z$	Ultra-precision electroweak
160 GeV	$e^+e^- \rightarrow WW$	Ultra-precision W mass
250 GeV	$e^+e^- \rightarrow Zh$	Precision Higgs couplings
350-400 GeV (Upgrade)	$e^+e^- \rightarrow t\bar{t}$	Top quark mass and couplings
	$e^+e^- \rightarrow WW$	Precision W couplings
	$e^+e^- \rightarrow \nu\bar{\nu}h$	Precision Higgs couplings
500 GeV (Upgrade)	$e^+e^- \rightarrow f\bar{f}$	Precision search for Z'
	$e^+e^- \rightarrow t\bar{t}h$	Higgs coupling to top
	$e^+e^- \rightarrow Zhh$	Higgs self-coupling
	$e^+e^- \rightarrow \bar{x}x$	Search for supersymmetry
	$e^+e^- \rightarrow AH, H^+H^-$	Search for extended Higgs states
700-1000 GeV (Upgrade)	$e^+e^- \rightarrow \nu\bar{\nu}hh$	Higgs self-coupling
	$e^+e^- \rightarrow \nu\bar{\nu}VV$	Composite Higgs sector
	$e^+e^- \rightarrow \nu\bar{\nu}t\bar{t}$	Composite Higgs and top
	$e^+e^- \rightarrow \bar{t}t^*$	Search for supersymmetry

In the ILC, electrons and their antiparticles (positrons) are accelerated and collided at high energy. The physics process of the ILC at a centre-of-mass energy of 250 GeV is the reaction $e^+e^- \rightarrow Zh$. The current program of the ILC (250 GeV) will focus on high-precision and model-independent measurements of the Higgs boson coupling. In addition, it will search for direct new physics in exotic Higgs decays and in pair-production of weakly interacting particles, even exploration of beyond the Standard Model physics.

In the future, the ILC will be upgraded for raising the centre-of-mass energy to 500 GeV even 1 TeV. With the raising of the centre-of-mass energy, the ILC can be used to take precision studies of the top quark and measurement of the top Yukawa coupling, to determine the strength of the Higgs boson's nonlinear self-interaction and to search for new particles.

1.1.2 ILC Layout

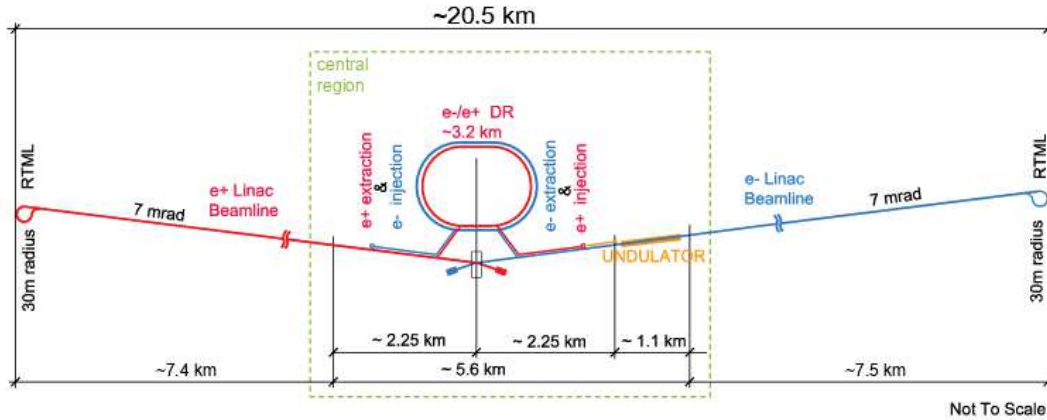


Figure 1.1: Schematic layout of the ILC in the 250 GeV staged configuration [18].

The schematic layout of the ILC in the current 250 GeV configuration is shown in figure 1.1. It is composed of two linear accelerators that face each other, stretching approximately 20.5 kilometres in length. Main parts of the ILC system are expressed as [7]:

1. Electrons (e-) and Positrons (e+) Sources. They are designed to produce 5 GeV beam pulses.
2. Damping Ring (DR). There are two oval DRs housing in a common tunnel, operating at a beam energy of 5 GeV. Each oval DR has 3.2 km circumference. They are used to accept electron and positron beams with large emittances and produce the low-emittance beams, to dampen the incoming beam jitter to provide highly stable beams and to delay bunches from the source.
3. Main Linac. Two main linacs are used to accelerate beams from 5 GeV to the maximum 125 GeV. Each main linac is comprised of two parts. The first part is a two-stage bunch compressor system. Beams are accelerated to 15 GeV in the second stage and the bunch length is reduced from 6 mm to 0.33 mm. The second part following the two-stage bunch compressor is the main linac which is about 6 km.
4. Ring To Main Linac (RTML). It is the connection part between the DR and the entrance of the main linac. It is used to transport of the beams from the DR to upstream ends of the main linac, collimate the beam halo generated in the DR.
5. Beam Delivery System (BDS). Two BDSs are used to transport and focus beams from two main linacs to the interaction point, then take beams into

collisions. Each BDS is 2254 m long from the end of the main linac to the interaction point.

1.2 ILC Experimental Conditions

Major experimental conditions of the ILC are introduced in the section, including the beam structure and the beam background. Experimental conditions determine some requirements for design of the detector.

1.2.1 Beam Structure

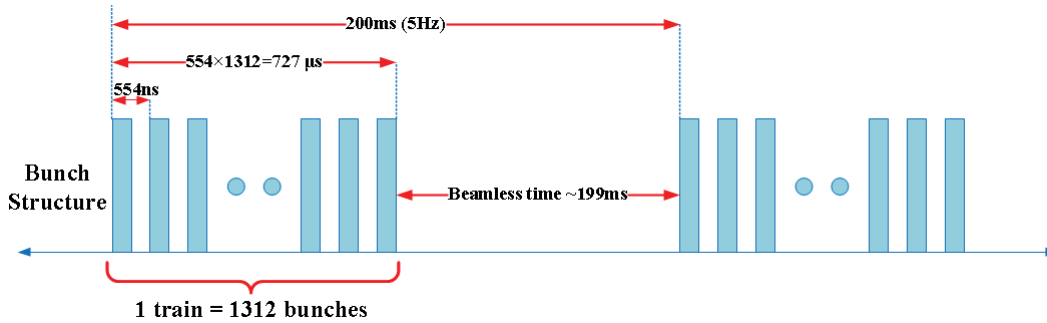


Figure 1.2: Beam structure of the ILC.

As presented in figure 1.2, the beam structure of the ILC is composed of trains at a frequency of 5 Hz (5 trains/second). Each train maintains about $727 \mu\text{s}$ constituted by 1312 bunches. A bunch is separated from the other by $\sim 554 \text{ ns}$. Between two trains there is a period of $\sim 199 \text{ ms}$ named beamless time [7][13].

The beam structure is related to the design of detectors in the ILC. Average power consumption of detectors can be reduced by switching off during beamless time which occupies about 99% period. The known interval between every two bunches and trains makes a possible to achieve detectors without triggers. The read-out strategy and sequence are can be implemented between two bunches or after a train [19].

1.2.2 Beam Background

Beamstrahlung is the most important background in the ILC which is created via the bunch interacting with the electromagnetic field of another bunch. In the approach procedure of electron and positron bunches which have strong electric fields, as the

small size of bunches indicates that they possess a very high space charge. As shown in figure 1.3, under the effect of the electromagnetic field of bunches, two beams from opposite directions do not point to each other directly, while towards the centre of the oncoming bunch, which is named the pinch effect. Beamstrahlung photons are generated by the beam-beam interaction to radiate the energy [20][21]. Electron-positron pairs with low momenta are released around the interaction point by beamstrahlung photons, which makes a major contribution to the machine-induced background [22][23].

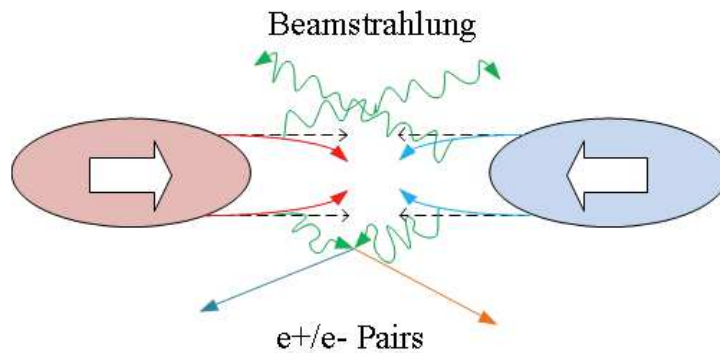


Figure 1.3: Illustration of the pinch effect and generation of beamstrahlung photons in bunch collisions.

Low momentum electrons and positrons produced by beamstrahlung photons hit on detectors and make an influence on physics measurements. Momenta of these particles typical lie in the range of $10\text{-}100\text{ MeV}/c$ [19]. These background particles are from the interaction region, forward region and even the detector region.

1.3 International Large Detector

High precision detectors will be equipped in the ILC to provide excellent vertexing and tracking capabilities. Two concepts of detectors, the Silicon Detector (SiD) and the ILD, are developed. The two detectors are swapped into the interaction point within the scheme named "push-pull", to achieve the sharing of the luminosity [17][24], as shown in figure 1.4.

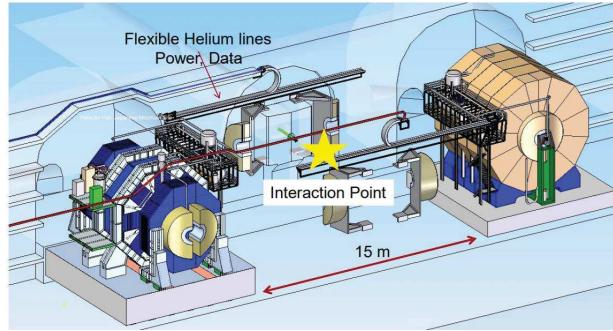


Figure 1.4: Two detectors and the "push-pull" mode [25].

The ILD is designed as a multi-purpose detector concept, which has been optimised on the respect of precision. As shown in figure 1.5, the concept schematic is composed of a vertex detector, a hybrid main tracking system, including a silicon tracking part and a Time Projection Chamber (TPC), a calorimeter system and the outer detector including a muon system and a coil and yoke system.

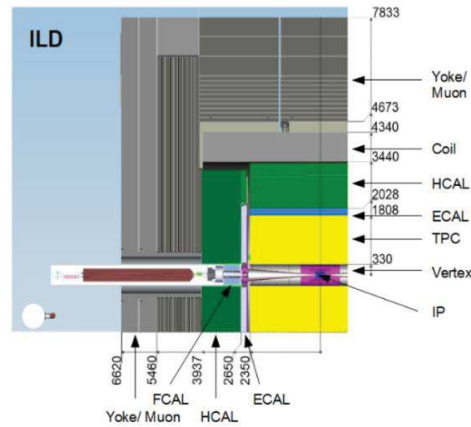


Figure 1.5: Quadrant view of the ILD detector concept. Dimensions are in mm [26].

1.3.1 Vertex Detector

The vertex detector is used to measure primary interaction vertices and secondary vertices from decay particles. It is located in the most inner layer around the interaction point of the ILD. For the physics program of the ILC, the vertex detector will play important role on flavour tagging, displaced vertex charge determination and tracking capability for the low momentum particles that cannot reach the main tracking system. The vertex detector is designed based on the ILC experimental conditions and some physics constraints (spatial resolution and material budget, etc.)

Impact Parameter Resolution

The performance of spatial resolution can be presented by the impact parameter resolution, which is written as [19]

$$\sigma_d = \sigma_{tracking} \oplus \sigma_{MS} = a \oplus \frac{b}{p \times \sin^2 \theta}, \quad (1-1)$$

where

p is the particle momentum.

θ is the polar angle with respect to the beam axis.

As shown in figure 1.6(a), when a charged particle traverses the vertex detector including two layers of detectors (Detector 1 and Detector 2), the reconstructed track has a discrepancy with the real track ($\sigma_{tracking}$). $\sigma_{tracking}$ is related to the detector geometry (R1 and R2) and the spatial resolution (σ_1 and σ_2 , $\sigma_1 = \frac{\text{Pixel pitch of vertex detector 1}}{\sqrt{12}}$). As shown in formula (1-2), $\sigma_{tracking}$ achieves the best precision with small values of radii and spatial resolutions.

$$\sigma_{tracking} = a = \frac{R1\sigma_1 \oplus R2\sigma_2}{R2-R1}. \quad (1-2)$$

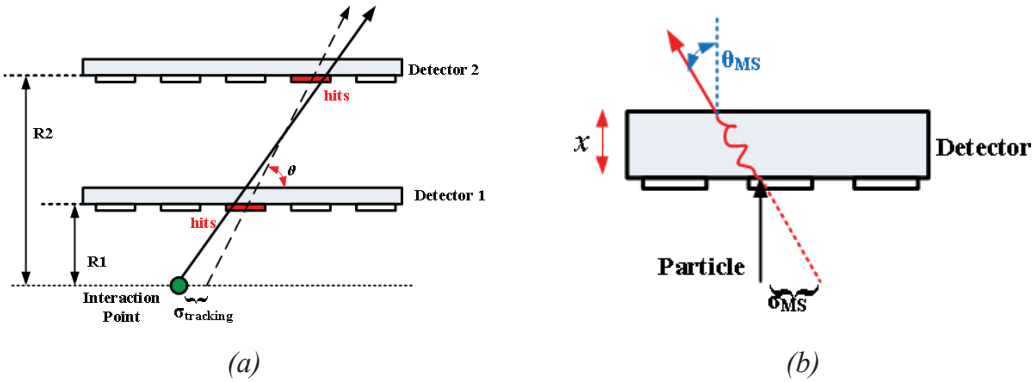


Figure 1.6: Impact parameter resolution (a) Finite single point resolution (b) Multiple scattering.

As shown in figure 1.6(b), for a single detector, when a charged particle traverses the detector, the particle undergoes small-angle deflections (θ_{MS}). σ_{MS} is the error of the impact parameter due to the multiple scattering effect. Parameter b depends on the distance of the first detector to the interaction point and the material budget (x/X_0),

¹ $x \oplus y = \sqrt{x^2 + y^2}$

where X_0 is the radiation length of the scattering medium.

$$b = R1 \times 13.6 \text{ (MeV)} \times \sqrt{\frac{x}{X_0}} \times \left[1 + 0.038 \ln \left(\frac{x}{X_0} \right) \right] \quad (1 - 3)$$

Some examples of parameter a and b in formula (1-1) for other experiments are shown in table 1-2. Parameter a and b are set as $\leq 5 \text{ } (\mu\text{m})$ and $\leq 10 \text{ } (\mu\text{m}\cdot\text{GeV})$ for the ILD.

Table 1-2: Parameter a and b for detectors.

	$a \text{ } (\mu\text{m})$	$b \text{ } (\mu\text{m}\cdot\text{GeV})$
LEP	25	70
SLD	8	33
LHC	12	70
RHIC-II	13	19
ILD	≤ 5	≤ 10

The impact parameter resolution of ILD ($a=5 \text{ } \mu\text{m}$ and $b=10 \text{ } \mu\text{m}\cdot\text{GeV}$) is simulated according to the formula (1-1). As shown in figure 1.7, the polar angle (θ) is fixed (30, 60, 90 degrees), the impact parameter resolution increases as the momentum of the charged particle decreases. The track generated by a low momentum charged particle will make larger deflection than that by a high momentum charged particle.

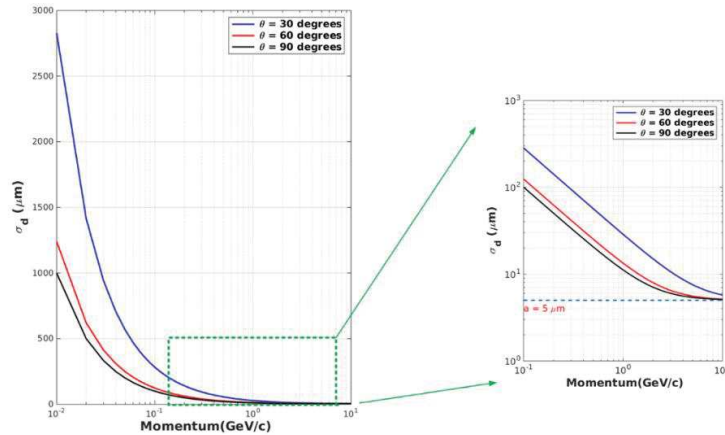


Figure 1.7: Impact parameter resolution as a function of the particle momentum.

Requirements

In order to meet experimental conditions and the impact parameter resolution of the ILC, requirements for the ILD are as follows:

- Read-out time $\sim 2\text{-}9 \mu\text{s}$
- Spatial resolution: $\leq 3 \mu\text{m}$ (corresponding to a pitch of $\sim 17 \mu\text{m}$);
- Material budget: $O(0.15\% X_0/\text{layer})$;
- A first layer located at a radius of $\sim 1.6 \text{ cm}$;
- Occupancy: $\sim 5 \text{ part}/\text{cm}^2/\text{BX}$.
- Radiation hardness: $O(100\text{kRad})$ and $O(1 \times 10^{11} n_{\text{eq}}(1\text{MeV})/\text{year (layer 1)})$.
- Power dispersion: $\sim 50 \text{ mW} / \text{cm}^2$.

Geometries

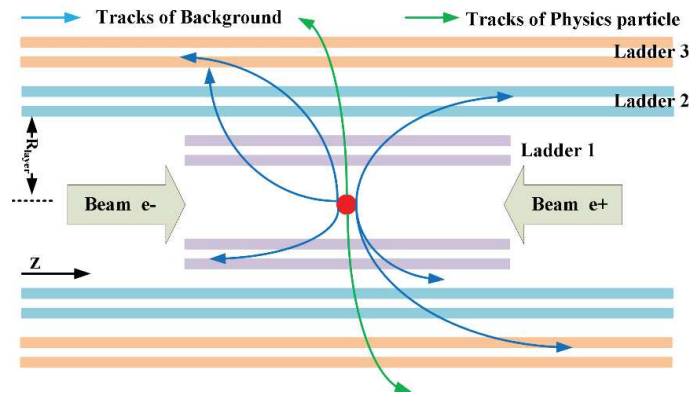


Figure 1.8: Vertex detector scheme of the ILD.

The vertex detector scheme (figure 1.8) of the ILD consists of three double-sided ladders which are equipped by CMOS pixel sensors on both sides ($\sim 2 \text{ mm}$ apart) [27]. Radii of the ladders range from 16 mm to 60 mm, Z position ranges from 62.5 mm to 125 mm, as presented in table 1-3. Six pieces of position information of a charged particle which traverses the detector are recorded and measured.

Table 1-3: Parameters of the design composed of three layers of double-sided ladders [26].

Barrel	layer	R_{layer} (mm)	Z (mm)
Ladder 1	Layer1	16	62.5
	Layer2	18	62.5
Ladder 2	Layer3	37	125
	Layer4	39	125
Ladder 3	Layer5	58	125
	Layer6	60	125

1.3.2 Silicon Tracking Part

The silicon tracking part is a complement component of the main tracking system for the track reconstruction capability. It is made up of four components to measure particles' momenta, including the Silicon Inner Tracker (SIT), the Silicon External Tracker (SET), the Forward Tracking Detector (FTD) and the Endcap Tracking Detector (ETD).

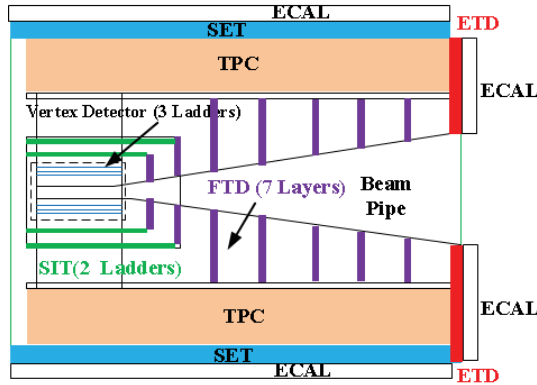


Figure 1.9: ILD schemes of the silicon tracking system.

As shown in figure 1.9, the SIT and the SET are barrel components. The SIT is positioned between the vertex detector and the TPC, and constituted by 2 double layers of CMOS pixels sensors. The SET is located between the TPC and the Electromagnetic CALorimeter (ECAL, see figure 1.5), it is composed of 2 layers of silicon strip detectors. The FTD consists of 7 tracking disks that are positioned between the beam pipe and the TPC, the first two disks which are closed to the vertex detector are pixel detectors and the other five disks are silicon strip detectors. The ETD is located between the TPC end plate and the ECAL, providing a precise point for tracks that go into the endcap [26][28].

1.3.3 Time Projection Chamber

The Time Projection Chamber (TPC) is a central component of the main tracking system. It is about 4.6 m in length, from 33 cm to 180 cm in radii. The TPC is optimised for 3-dimensional point resolution (better than 100 μm in $r\phi$, and about 1 mm in Z) which provides large accuracy for the reconstruction. For charged particles with momenta above 100 MeV, the tracking efficiency up to nearly 100% simulated realistically with full backgrounds. The TPC providing particle identification

capabilities by the specific energy loss (dE/dx).

1.3.4 Calorimeter System

Calorimeters are used to measure the energy of a particle. In the particle flow approach, all particles in an event are reconstructed individually. The calorimeter system for ILD consists of a nearly cylindrical barrel calorimeter and two large end cap calorimeters. Each calorimeter is composed of the ECAL and the Hadronic CALorimeter (HCAL), which is designed to identify photons and neutral hadrons respectively and measure their energy.

1.3.5 Muon System

The muon system is used to identify muons in the ILD by some measurement stations outside the solenoid coil. It is implemented by square tiles of $30 \times 30 \text{ mm}^2$ and a thickness of 10 mm, with the Silicon PhotoMultiplier (SiPM) readout.

1.3.6 Coil and Yoke System

A large volume superconduction coil surrounding calorimeters is used to supply the magnetic field for a nominal 3.5 T and maximum 4 T solenoidal central field. The iron yoke surrounding the coil is used to identify muons and catch tails of hadronic showers. It returns the flux of the magnetic and reduces the outside stray fields.

1.4 Motivation

There are a large amount of hits generated by charged particles coming from the beam background (low momentum). Our group in the IPHC proposed to integrate the Artificial Neural Network into CMOS pixel sensor to tag and remove hits generated by these particles. The motivation of the concept is described in the section.

1.4.1 Challenges for Track Reconstruction

For the ILC program at the centre-of-mass energy of 250 GeV, data rate

requirement for the vertex detector is ~ 3 Gbits/s with the safety factor of 3, which is $\sim 30\%$ - 50% data flow of the total system. A large fraction of the data flow is related to hits generated by particles coming from the beam background. As simulation result shown in figure 1.10, 10^4 hits are generated on the layer 1 of the vertex detector by particles with momenta of 10 MeV/c. Particles from the beam background have typical lower momenta (~ 10 - 100 MeV/c) [19] than particles coming from the physics process.

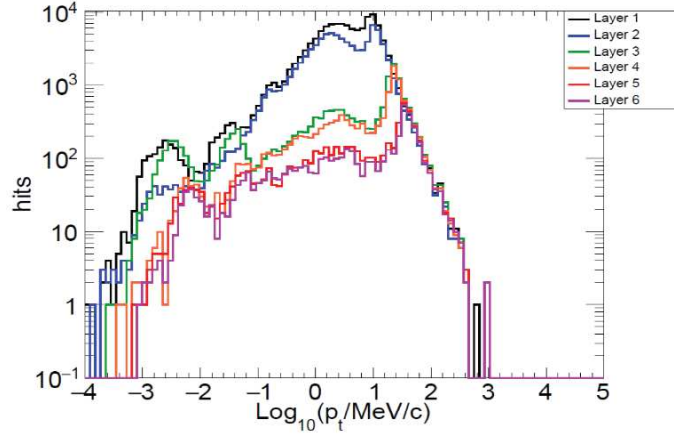


Figure 1.10: Beam background features simulation [29].

Track reconstruction for low-momentum particles is challenging. Due to the multiple scattering effect, particles with low momenta make obvious deflections when they are traversing a layer of the detector leading to the failure of reconstruction. In figure 1.11, hits and tracks of different momentum particles in a 6-layer detector are presented and compared. Firstly, these deflections formed by low momentum particles produce many segments of different layers, which cannot be merged. Secondly, low momentum particles creating large deflections on the track may hit only one layer of the detector (just a single hit), resulting in the lack of information for reconstruction.

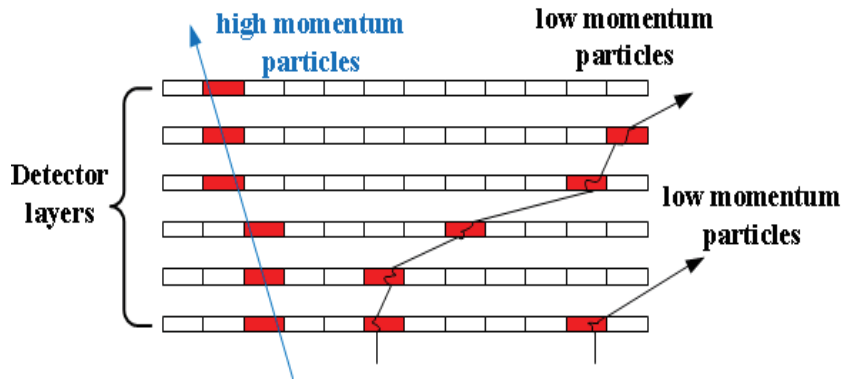


Figure 1.11: Schematic diagram of tracks generated by particles, one is created by a particle with high momentum (blue) and others are created by particles with low momenta.

1.4.2 Trajectory of Charged Particles

In detectors of the ILC, under the effect of the magnetic field, charged particles move along the helix trajectory. The helix trajectory is shown in figure 1.12. *Vertex* represents the vertex detector of the ILD, z presents the beam direction, the momentum (P) of the particle is decomposed into the transverse momentum (P_T) and the momentum along the Z -axis (P_Z).

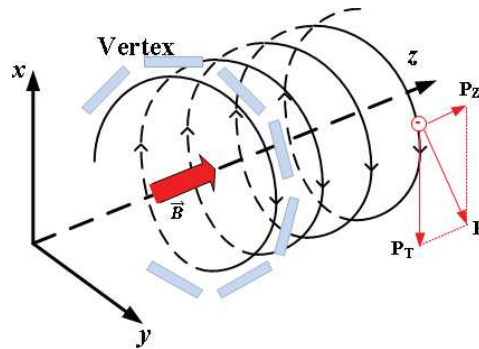


Figure 1.12: Helix trajectory of charged particles under the effect of the magnetic field.

The trajectory is projected on both the transverse and parallel plane respectively to illustrate and analyse.

Trajectory Projected on Transverse Plane

As indicated in figure 1.13, the trajectory of an electron (e^-) is projected on the transverse plane (plane xy) and presents a circle movement. The electron hits on the vertex detector and the incident angle projected is named θ_T .

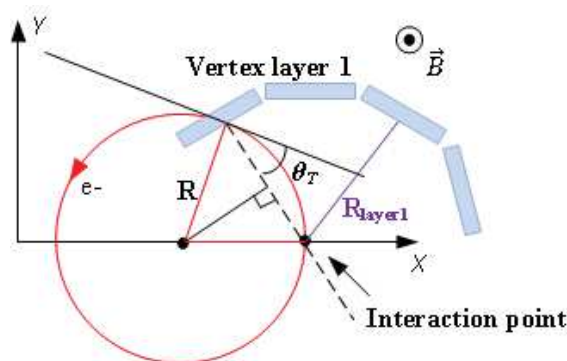


Figure 1.13: Trajectory projection of a charged particle on the transverse plane.

The centripetal force of the electron is supplied by the Lorentz force:

$$qvB = \gamma m \frac{v^2}{R}, \quad (1 - 4)$$

Where

v is the speed of the electron.

B is the magnetic field perpendicular to the direction of the electron, measured in *Tesla*.

q is the electron charge.

m is the rest mass of the electron.

γ is a constant value.

R is the radius of the trajectory measured in meter.

According to formula (1-4), the momentum of the electron in the magnetic field is expressed as

$$P = \gamma mv = qBR, \quad \left(\text{units: } kg \cdot \frac{m}{s} \right). \quad (1 - 5)$$

Applying unit conversion to the formula (1-5), the transverse momentum is

$$P_T \approx 0.3 \times B[T] \times R[m], \quad \left(\text{units: } \frac{GeV}{c} \right), \quad (1 - 6)$$

According to formula (1-6), the minimum transverse momentum required for an electron to arrive at different layers is as follows (without the influence of energy loss and scattering in the trajectory and $B = 3.5$ T):

Table 1-4: Minimum transverse momentum of a particle to arrive different layers (R_{layer} is the radius of the vertex detector and R is the radius of the particle trajectory).

Layer	$R_{\text{layer}}(\text{mm})$	$R(\text{mm})$	$P_T(\text{MeV}/c)$
1	16	8	8.4
2	18	9	9.5
3	37	19.5	19.5
4	39	19.5	20.5
5	58	29	30.5
6	60	30	31.5

In figure 1.13, incident angle θ_T is the angle between the tangent line at the hit point and the normal line of the vertex detector, calculated as

$$\theta_T = \frac{\pi}{2} - \arccos\left(\frac{R_{layer1}}{2 \times R}\right) = \frac{\pi}{2} - \arccos\left(\frac{0.3 \times B \times R_{layer1}}{2 \times P_T}\right), \quad (1 - 7)$$

where

R_{layer1} is the radius of the first layer vertex detector, which is 16mm [26].

According to formula (1-7), θ_T as a function of the transverse momentum is plotted in figure 1.14. θ_T decreases as the transverse momentum of the particle increases. Particles from the beam background (typical 10-100 MeV/c) [19] possess larger incident angles than particles from the physics event due to low momenta.

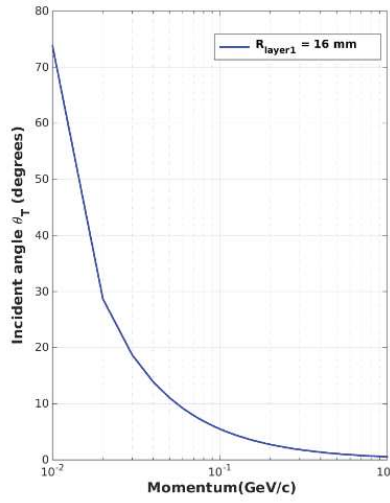


Figure 1.14: Incident angle θ_T as a function of the particle transverse momentum (P_T).

Trajectory Projected on Parallel Plane

In figure 1.15, the trajectory of the electron projected on a parallel plane, where Z -axis represents the beam line, *Vertex layer 1* presents the location of the ladder 1 whose $|Z|$ is 62.5 mm [26], b_e is the angle between the trajectory and Z -axis,

$$\theta_b = \arctan\left(\frac{R_{layer1}}{x}\right), \quad (1 - 8)$$

where

x is the distance along the Z -axis from the interaction point to the hit location.

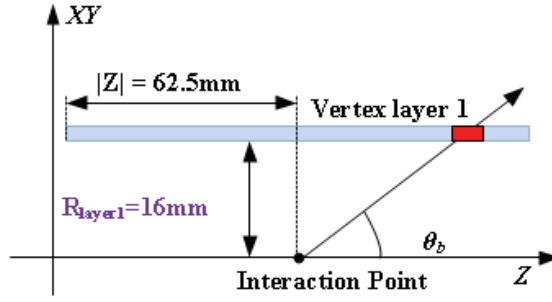


Figure 1.15: Trajectory projection of a charged particle on the parallel plane.

Minimum angle b_e that can generate a hit on the vertex detector is 14.36 degrees, calculated as

$$\theta_{bmin} = \arctan\left(\frac{R_{layer1}}{|z|}\right) = \arctan\left(\frac{16}{62.5}\right) = 14.36 \text{ (deg)}. \quad (1 - 9)$$

1.4.3 Principle for Particle Recognition

Considering the artificial neural network successfully applied in many fields of pattern recognition, our group in the IPHC proposed a CMOS pixel sensor with artificial neural networks to identify and remove hits generated by particles from the beam background for reducing the bandwidth (maximum rate of data transfer) of the data stream and improving tracking capability.

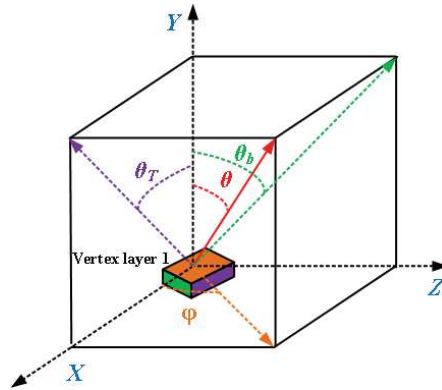


Figure 1.16: Schematic diagram of an incident angle on the vertex detector.

As shown in figure 1.16, angle θ_b and θ_T is the projection of the incident angle (θ) on two planes respectively. Under the situation that θ_b has a fixed value, the incident angle (θ) increases as the particle transverse momentum decreases (P_T). Particles from the beam background (typical lower momenta) possess larger incident angles into the vertex detector than those of particles from physics events.

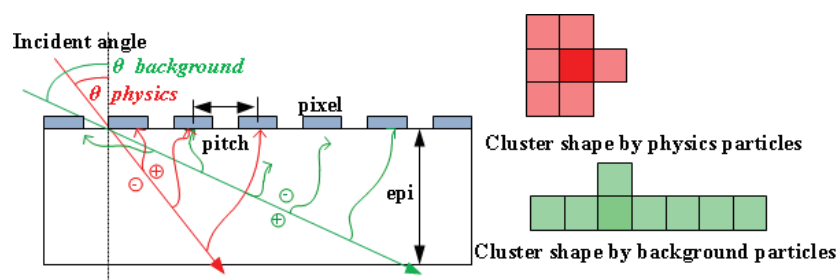


Figure 1.17: Cluster shapes generated by particles from the physics process and particles from the beam background.

When a charged particle passing through the epitaxial layer of the CPS vertex detector, electron-hole pairs are created by the ionization process about typical ~ 80 e-h/ μm . Electrons are collected by the diode in each pixel. If the hit is at nearby the border of pixels, electrons would be collected by two or more independent pixels. These independent pixels constitute a charge cluster which expresses hit information. Especially with the decrease in the size of the pixel geometry, the charge-sharing effect becomes more obvious and important [30][31][32]. In figure 1.17, the larger incident angle of a background particle leads to producing an elongated cluster shape. The difference in clusters generated by the two particles makes it possible to tag and remove hits generated by background particles using artificial neural networks.

1.5 Summary

The ILC project and the motivation of a CMOS pixel sensor with on-chip artificial neural networks are introduced in the chapter. In the ILC, a large amount of hits are generated by particles coming from the beam background which have low momenta. Due to the multiple scattering, tracks make large deflections for these particles, leading to the failure on the track reconstruction. Our group propose a CPS with on-chip ANNs to tag and remove hits generated by these particles. Under the effect of the magnetic field, particles with low momenta produce large incident angles on the vertex detector and create elongated cluster shapes. An ANN is implemented to reconstruct the incident angle and tag the hit.

The principle and technology of semiconductor detector will be introduced in the next chapter.

1.6 Bibliography

- [1]. <https://home.cern/science/physics/standard-model>
- [2]. Brau, James, Yasuhiro Okada, and Nicholas Walker. "Ilc reference design report volume 1-executive summary." *arXiv preprint arXiv:0712.1950* (2007).
- [3]. Edwards, Donald A., and Michael J. Syphers. *An introduction to the physics of high energy accelerators*. John Wiley & Sons, 2008.
- [4]. Wille, Klaus. *The physics of particle accelerators: an introduction*. Clarendon Press, 2000.
- [5]. <https://ilchome.web.cern.ch/ilc/project>
- [6]. <https://home.cern/science/accelerators/large-hadron-collider>
- [7]. Bambade, Philip, et al. "The International Linear Collider: A Global Project." *arXiv preprint arXiv:1903.01629* (2019).
- [8]. Barish, Barry, and James E. Brau. "The International Linear Collider." *International Journal of Modern Physics A* 28.27 (2013): 1330039.
- [9]. Behnke, Ties. "The international linear collider." *Fortschritte der Physik* 58.7-9 (2010): 622-627.
- [10]. Adams, T., et al. "Terascale physics opportunities at a high statistics, high energy neutrino scattering experiment: nuSONG." *International Journal of Modern Physics A* 24.04 (2009): 671-717.
- [11]. Loew, Gregory A. "Report from the international linear collider technical review committee." *Proceedings of the 2003 Particle Accelerator Conference*. Vol. 1. IEEE, 2003.
- [12]. Loew, Gregory. *International Linear Collider Technical Review Committee: Second Report, 2003*. No. SLAC-R-606. Stanford Linear Accelerator Center, Menlo Park, CA (US), 2003.
- [13]. Adolphsen, Chris. *The International Linear Collider Technical Design Report-Volume 3. II: Accelerator Baseline Design*. No. arXiv: 1306.6328; ILC-REPORT-2013-040; ANL-HEP-TR-13-20; BNL-100603-2013-IR; IRFU-13-59; CERN-ATS-2013-037; COCKCROFT-13-10; CLNS-13-2085; DESY-13-062; FERMILAB-TM-2554; IHEP-AC-ILC-2013-001; INFN-13-04-LNF; JAI-2013-001; JINR-E9-2013-35; JLAB-R-2013-01; KEK-REPORT-2013-1; KNU-CHEP-ILC-2013-1; LLNL-TR-635539; SLAC-R-1004; ILC-HIGRADE-REPORT-2013-003. Argonne National Lab.(ANL),

- Argonne, IL (United States); Thomas Jefferson National Accelerator Facility (TJNAF), Newport News, VA (United States); Brookhaven National Laboratory (BNL), Upton, NY (United States); SLAC National Accelerator Lab., Menlo Park, CA (United States); Fermi National Accelerator Lab.(FNAL), Batavia, IL (United States), 2013.
- [14]. Adolphsen, Chris. *The International Linear Collider Technical Design Report-Volume 3. I: Accelerator & in the Technical Design Phase*. No. arXiv: 1306.6353; ILC-REPORT-2013-040; ANL-HEP-TR-13-20; BNL-100603-2013-IR; IRFU-13-59; CERN-ATS-2013-037; COCKCROFT-13-10; CLNS-13-2085; DESY-13-062; FERMILAB-TM-2554; IHEP-AC-ILC-2013-001; INFN-13-04-LNF; JAI-2013-001; JINR-E9-2013-35; JLAB-R-2013-01; KEK-REPORT-2013-1; KNU-CHEP-ILC-2013-1; LLNL-TR-635539; SLAC-R-1004; ILC-HIGRADE-REPORT-2013-003. Argonne National Lab.(ANL), Argonne, IL (United States); Thomas Jefferson National Accelerator Facility (TJNAF), Newport News, VA (United States); Brookhaven National Laboratory (BNL), Upton, NY (United States); SLAC National Accelerator Lab., Menlo Park, CA (United States); Fermi National Accelerator Lab.(FNAL), Batavia, IL (United States), 2013.
- [15]. Japan Association of High Energy Physicists (JAHEP), “*A proposal for a phased execution of the international linear collider project,*” http://www.jahep.org/office/doc/201210_ILC_staging_e.pdf (2012).
- [16]. Bambade, Philip, et al. "The International Linear Collider. A European Perspective." *arXiv preprint arXiv:1901.09825*(2019).
- [17]. Baer, Howard, et al. "The International linear collider technical design report-volume 2: physics." *arXiv preprint arXiv:1306.6352* (2013).
- [18]. <https://cds.cern.ch/record/2655225/files/TDR-machine-layout-cartoon-staged-mirror.png>
- [19]. Besson, Auguste Guillaume. "The ILC Vertex Detector requirements." *PoS* (2017): 047.
- [20]. Vogel, Adrian. "Beam-induced backgrounds in detectors at the ILC." (2008).
- [21]. Yokoya, Kaoru, and Pisin Chen. "Beam-beam phenomena in linear colliders." *Frontiers of Particle Beams: Intensity Limitations*. Springer, Berlin, Heidelberg, 1992. 415-445.
- [22]. Chen, Pisin. *Disruption, beamstrahlung, and beamstrahlung pair creation*. No. SLAC-PUB-4822; CONF-8806243-31. Stanford Linear Accelerator Center, Menlo Park, CA (USA), 1988.
- [23]. Zolotarev, M. S., E. A. Kuraev, and V. G. Serbo. *Estimates of electromagnetic background processes for the VLEPP project*. No. SLAC-TRANS-0227. 1987.

- [24]. Parker, Brett, et al. *Functional Requirements on the Design of the Detectors and the Interaction Region of an e^+e^- Linear Collider with a Push-Pull Arrangement of Detectors*. No. SLAC-PUB-13657. 2009.
- [25]. Tim Barklow. *The SiD Detector at ILC*, The European Physical Society Conference on High Energy Physics (EPS-HEP) 2017, Venice, Italy, July 08, 2017.
- [26]. Behnke, Ties. *The international linear collider technical design report-volume 4: detectors*. No. arXiv: 1306.6329; ILC-REPORT-2013-040; ANL-HEP-TR-13-20; BNL-100603-2013-IR; IRFU-13-59; CERN-ATS-2013-037; COCKCROFT-13-10; CLNS-13-2085; DESY-13-062; FERMILAB-TM-2554; IHEP-AC-ILC-2013-001; INFN-13-04-LNF; JAI-2013-001; JINR-E9-2013-35; JLAB-R-2013-01; KEK-REPORT-2013-1; KNU-CHEP-ILC-2013-1; LLNL-TR-635539; SLAC-R-1004; ILC-HIGRADE-REPORT-2013-003. Argonne National Lab.(ANL), Argonne, IL (United States); Pacific Northwest National Lab.(PNNL), Richland, WA (United States); SLAC National Accelerator Lab., Menlo Park, CA (United States); Fermi National Accelerator Lab.(FNAL), Batavia, IL (United States), 2013.
- [27]. Simon, Frank. "Higgs Physics at future Linear Colliders-A Case for precise Vertexing." *arXiv preprint arXiv:1401.6302*(2014).
- [28]. The ILD Detector at the ILC, "Ties Behnke Deutsches Elektronen Synchrotron, DESY, Germany.https://indico.cern.ch/event/765096/contributions/3295752/attachments/1785276/2906298/ILD_European_Strategy_Document.pdf
- [29]. A. Perez , et al. "*Beamstrahlung background simulation status report*", AWLC 2017 workshop, June 30, 2017.
- [30]. Maj, P., et al. "Comparison of the charge sharing effect in two hybrid pixel detectors of different thickness." *Journal of Instrumentation* 10.02 (2015): C02006.
- [31]. Maj, P., et al. "Algorithms for minimization of charge sharing effects in a hybrid pixel detector taking into account hardware limitations in deep submicron technology." *Journal of Instrumentation* 7.12 (2012): C12020.
- [32]. Mathieson, K., et al. "Charge sharing in silicon pixel detectors." *Nuclear Instruments and Methods in Physics Research Section A: Accelerators, Spectrometers, Detectors and Associated Equipment* 487.1-2 (2002): 113-122.

2 Semiconductor Detectors

In the early 1980s, with the development of High Energy Physics (HEP), the lifetime of particles that needed to be measured reduced to the picosecond range. Bubble chambers and emulsions cannot catch up with the demand on the processing rate of a large amount of data; gas detectors cannot achieve the requirement on the spatial resolution. In 1983, semiconductor (silicon strip) detectors were used in the CERN's NA11/NA32 experiment for the first time. Semiconductor detectors measured the lifetime of particles and ultimately completed the identification and tagging of heavy quarks. Nowadays, semiconductor detectors are widely used in HEP experiments [1][2][3][4].

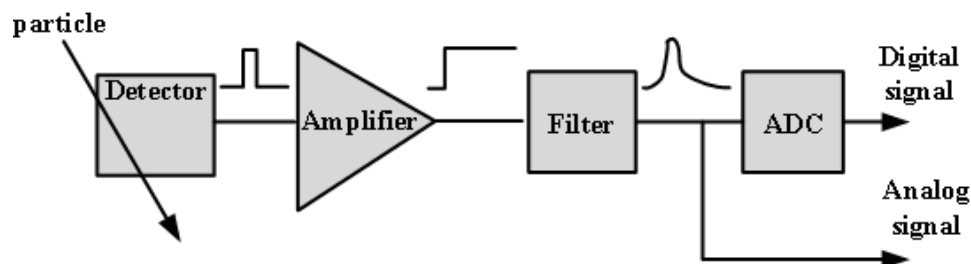


Figure 2.1: Typical semiconductor detector system.

A typical semiconductor detector system is shown in figure 2.1. Electron-hole pairs are created by the ionizing radiation effect between incident particles and the detector material. *Detector* is used to convert the energy deposited to an electrical signal. *Amplifier* is used to amplify the electrical signal. *Filter* is used to improve the signal-to-noise ratio of the system, then the electrical signal is digitized by Analog-to-Digital Converter (*ADC*).

Silicon detectors have following important advantages.

- Low ionization energy
Average 3.6 eV energy is needed to generate one electron-hole pair in silicon detectors. 30 eV energy is needed for gas detectors to generate one electron-ion pair.
- High density
Due to the high density of silicon material, the number of electron-hole pairs are large. For a Minimum Ionizing Particle (MIP), the number of ionized electron-hole pairs is about 80 e-/um, the average energy loss is about 300 eV/ μm (3.6 eV/e-h).
- Fast signal speed
Compared with liquid or gas detectors, silicon detectors process the electrical signal fast.

Basic properties and types of semiconductor detectors (*Si* detector) are described in the chapter. Firstly, generation and transportation of carriers in semiconductor detectors are described. Then, basic components of semiconductor detectors, the P-N junction and the MOS structure, are introduced. Finally, various kinds of semiconductor detectors are given and compared.

2.1 Carriers Generation

In this section, the generation of carriers is described based on two types of particles: photons and charged particles.

2.1.1 Carriers Generated by Photons

An incident photon is absorbed or scattered when it passes through semiconductor detectors. The energy loss of the incident photon is produced since the physical process including the Photoelectric effect, the Compton effect and the Electron-Positron pair production. Contributions of different physical processes depend on the photon energy and the material.

As illustrated in figure 2.2, if the energy loss of the photon is greater or equal to the energy of the band gap (E_G), an electron will be lifted to the conduction band and a hole will be left in the valence band. If the energy loss is less than the energy of the band gap

(E_G), it is possible that the photon would be absorbed since local states in the band gap due to lattice imperfections exist [5].

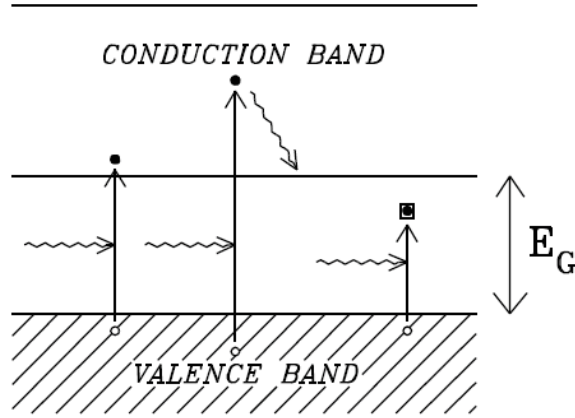


Figure 2.2: Generation of electrons and holes by absorption of photons, the energy loss = E_g , $>E_g$, and $<E_g$ [5].

2.1.2 Carriers Generation by Charged Particles

A charged particle passes through semiconductor detectors, due to the ionization effect, electron-hole pairs will be created around the track. The average energy of the charged particle used to create an electron-hole pair is 3.6 eV which is about three times larger than the band gap of 1.1 eV. The average energy loss of the charged particle can be calculated as the Bethe-Bloch formula (2-1):

$$-\frac{dE}{dx} = 4\pi N_A r_e^2 m_e c^2 z^2 \frac{Z}{A\beta^2} \left(\frac{1}{2} \ln \frac{2m_e c^2 \beta^2 \gamma^2 T_{max}}{I^2} - \beta^2 - \frac{1}{2} \delta(\gamma) \right). \quad (2-1)$$

In formula (2-1), N_A is the Avogadro's number ($6.0221415 \times 10^{23} \text{ mol}^{-1}$), r_e is the classical electron radius, m_e is the electron mass, c is the velocity of light, z is the charge of the incident particle. Z is the atomic number of the absorber. T_{max} is the maximum kinetic energy that can be imparted to a free electron in a single collision, I is the mean excitation energy, β is the relativistic boost and the γ is the Lorentz factor. The term δ is a density correction. The unit of results is $\text{MeV g}^{-1} \text{ cm}^2$ [6][7].

2.2 Carriers Transport

In semiconductor detectors, currents are generated by the movement of free carriers. Two types of currents are introduced to describe the transportation of free carriers in the semiconductor: The drift current and the diffusion current.

2.2.1 Drift

The drift current is formed due to an external electric field applied to semiconductor detectors. Free carriers (electrons and holes) are forced by the electric field in different directions.

$$J_n^{drift} = qn\mu_n E . \quad (2 - 2)$$

$$J_p^{drift} = qp\mu_p E . \quad (2 - 3)$$

The density of the electron and hole drift current (A/cm^2) is expressed as formula (2-2) and (2-3), respectively: p and n are the number of holes and electrons per cubic centimetre; q is the elementary charge ($1.602 \times 10^{-19} C$); μ_n and μ_p are the mobility of electrons and holes, with the unit of $cm^2/V \cdot s$; E is the electric field with the unit of V/cm .

The total density of the drift current is:

$$J_{drift} = qn\mu_n E + qp\mu_p E . \quad (2 - 4)$$

2.2.2 Diffusion

The diffusion current is formed thanks to the variation of the carrier concentration. Free carriers move from the high concentration region to the low concentration region when there is a difference between concentration gradients of the two regions. The density of the diffusion current (A/cm^2) is expressed in formula (2-5) and (2-6), respectively: D_p and D_n are diffusion coefficients for holes and electrons; p and n are the number of holes and electrons per cubic centimetre; q is the elementary charge.

$$J_n^{diff} = qD_n \frac{dn}{dx} . \quad (2 - 5)$$

$$J_p^{diff} = -qD_p \frac{dp}{dx} \tag{2 - 6}$$

The total density of the diffusion current is:

$$J_{diff} = qD_n \frac{dn}{dx} - qD_p \frac{dp}{dx} \tag{2 - 7}$$

2.3 P-N Junction

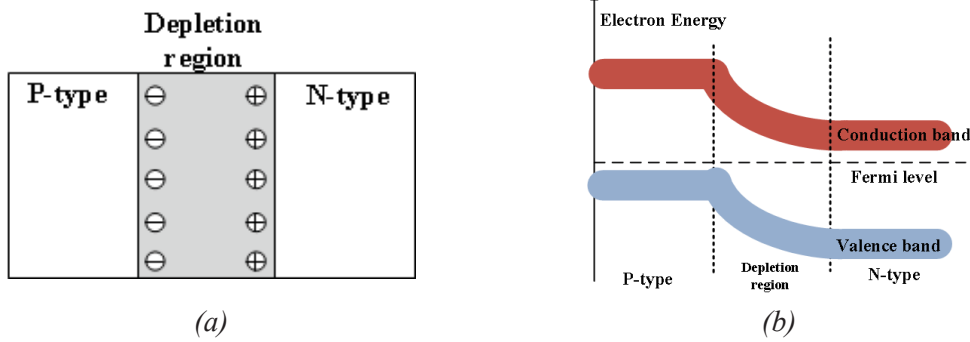


Figure 2.3: P-N junction (a) Depletion region (b) Energy band diagram.

P-N junctions are basic structures of semiconductor electronics. A P-N junction (figure 2.3 (a)) is produced by joining together the N-type and P-type semiconductor.

The principle of the P-N junction is described as follows: Firstly, free electrons in the N-type side diffuse to the P-type side and overcome the junction. Then, the free electrons recombine with holes nearby the junction in the P-type side. Donor ions left in the N-type side are positively charged and acceptor ions left in the P-type side are negatively charged. As a result, a built-in electric field pointing from N-type to P-type is created. The built-in electric field rejects the diffusion of carriers and keeps the dynamic equilibrium of the concentration.

No free charge carriers can rest in the region located around the junction between two sides, which is named the depletion region. According to the energy band schematic shown in figure 2.3 (b), it implies that extra energy is needed to transport an electron to overcome the depletion region.

The state of the P-N junction will be changed if the extra bias is applied. States under the forward bias and the reverse bias are described. The drift current in the P-N junction is not changed with the variety of the bias voltage as the number of minority charge carriers is limited [8][9].

2.3.1 Forward Bias

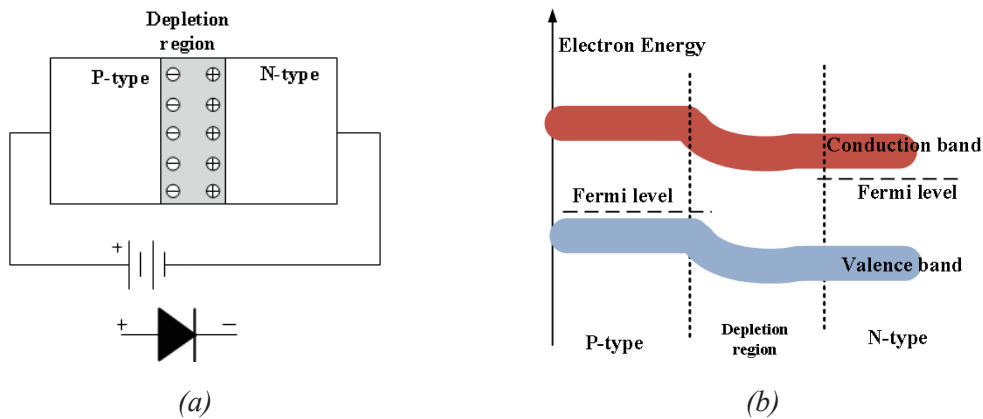


Figure 2.4: P-N junction under forward bias (a) Depletion region (b) Energy band diagram.

In figure 2.4 (a), a forward bias is applied to the P-N junction, which means that the P-type side is connected to a positive voltage and the N-type side is connected to a negative voltage. The negative voltage pushes free electrons in the N-type side move to the depletion region and recombine with holes, leading to the depletion region thinner and the built-in electric field weakened. In figure 2.4 (b), the barrier of the depletion region decreases, and the energy required to transport an electron reduces under the forward bias.

2.3.2 Reverse Bias

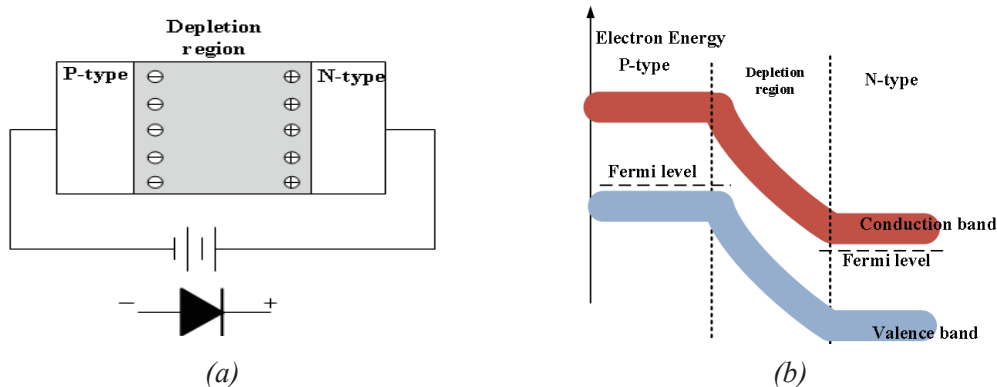


Figure 2.5: P-N junction under reverse bias (a) Depletion region (b) Energy band diagram.

In figure 2.5 (a), a reverse bias is applied to the P-N junction. Electrons nearby the junction are attracted by the positive voltage applied to the N-type side, move away from the depletion region, leading to the depletion region wider and the built-in electric field strengthened. In figure 2.5 (b), the barrier of the depletion region is increased

under reversed bias and the energy used to transport electrons from the N-type side to the P-type side becomes large.

2.4 Metal-Oxide-Semiconductor

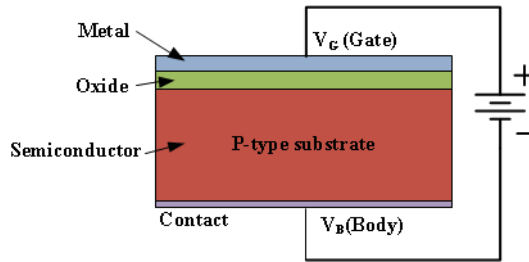


Figure 2.6: *N-type Metal-Oxide-Semiconductor structure.*

The Metal-Oxide-Semiconductor (MOS) diode is a basic structure used in the semiconductor device. It is composed of three layers, an oxide layer, a metal layer called gate (G) and a P-type or N-type semiconductor layer named substrate or body (B). An N-type channel MOS structure is shown in figure 2.6. Heavily doped polysilicon layers are often used instead of gate metal. Typically, voltages are applied to the gate (V_G) and body contact (V_B).

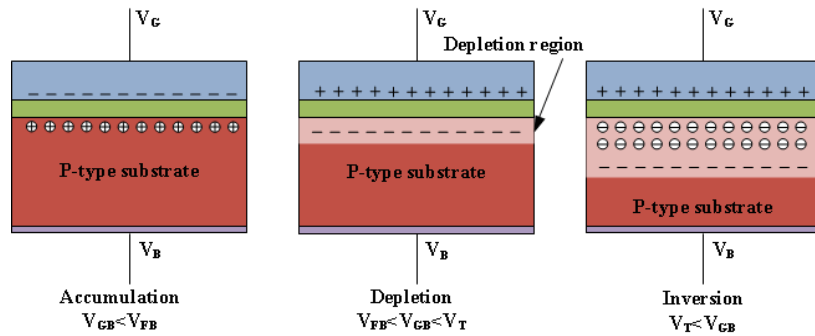


Figure 2.7: *An n-type MOS under accumulation, depletion and inversion conditions [10].*

Three bias modes (accumulation, depletion and inversion, see figure 2.7) and corresponding capacitance of the MOS diode are varied with the bias voltage applied to the gate and the body (V_{GB}). V_{FB} is the flat band voltage which makes the energy band of the semiconductor side present horizontally. The flat band indicates that there is no charge present in the oxide or at the oxide-semiconductor interface. In traditional MOSFET models, V_T is defined as the gate voltage that will drive the channel under the gate into strong charge inversion cases [11].

Accumulation

In the case of accumulation, the voltage applied to the gate and body contact is less than the flatband voltage ($V_{GB} < V_{FB}$). Carrier densities change accordingly in its surface region. Negative and positive charges are induced in the gate and the body, respectively. Holes are accumulated under the oxide-semiconductor interface.

Depletion

In the case of depletion, the voltage applied to the gate and body contact is larger than the flat band voltage and less than the threshold voltage ($V_{FB} < V_{GB} < V_T$). Positive charges are produced at the interface between the metal gate and the oxide. Holes in the body are repelled and a depletion region is created.

Inversion

In the case of inversion, the voltage applied to the gate and substrate contact is larger than the threshold voltage ($V_T < V_{GB}$). With the voltage V_{GB} increases, negative charges created at the interface become more and the depletion region is wider, leading to the surface of semiconductor inverts to N-type, an inversion layer is formed.

2.5 Silicon Detector Types

With the development of physics and the improvement for various HEP experiments, several types of silicon detectors have been proposed and established. Including strip detectors, Charged Coupled Devices (CCDs), hybrid pixel detectors, DEPLETED Field Effect Transistor (DEPFET) detectors and Monolithic Active Pixel Sensors (MAPS) are introduced.

2.5.1 Strip Detector

With the introduction of the planar process proposed by *Krammer* in 1980 to replace the technology of surface barrier, high-quality silicon detectors that have extremely low reverse currents can be implemented [12]. Thanks to the technology of photolithography, requirements on resolution and rate can be achieved by dividing the sensor into segments. Single-sided and double-sided strip detectors are described.

Single-sided strip detector

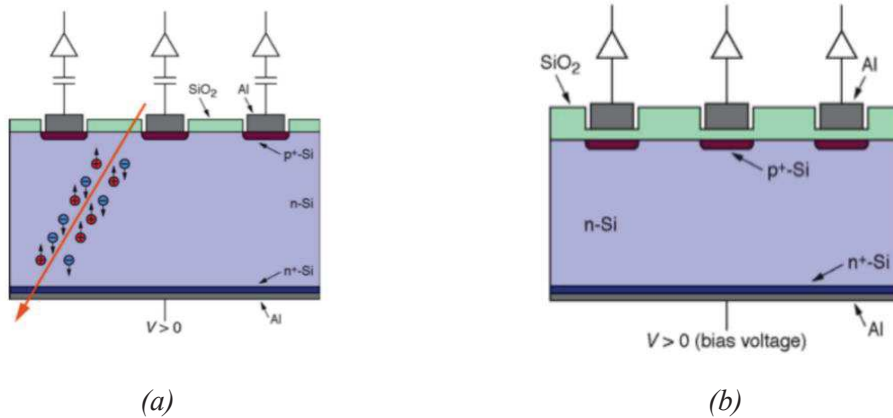


Figure 2.8: Single-sided strip detector (a) DC coupled strip detector (b) AC coupled strip detector [13].

The single-sided strip detector shown in figure 2.8 is composed of strips shaped P+-implantation. Electron-hole pairs will be created when a charged particle goes through the N-type silicon depletion zone. The single-sided strip detector can measure the position on one coordinate.

As shown in figure 2.8 (a), a charge sensitive amplifier connected directly (*DC coupling*) to strip is used to read out and process the signal. But it is difficult to use an amplifier that can achieve such a wide range of input current since the input current contains a part of leakage current which is larger than the signal current. The leakage current depends on the applied bias voltage and radiation damage [14]. In figure 2.8 (b), a capacitor is used to filter the digital current signal component from the input current (*AC coupling*) which is also known as capacitive coupling. The capacitor is generated by deposition of SiO₂ between the p+-implantation strip and aluminium strip. The capacitance depends on oxide thickness and strip width [15].

Double-sided strip sensor

In order to achieve the measurement of two-dimensional positions, additional strips are applied to the backside, which is called a double-sided strip detector. As shown in figure 2.9, on the backside of detectors, N-strips are connected with the amplifiers of the read-out structure and orthogonal to P-strips on the front side.

In 1990, double-sided silicon strip detectors were first used in the ALEPH silicon vertex detector [16].

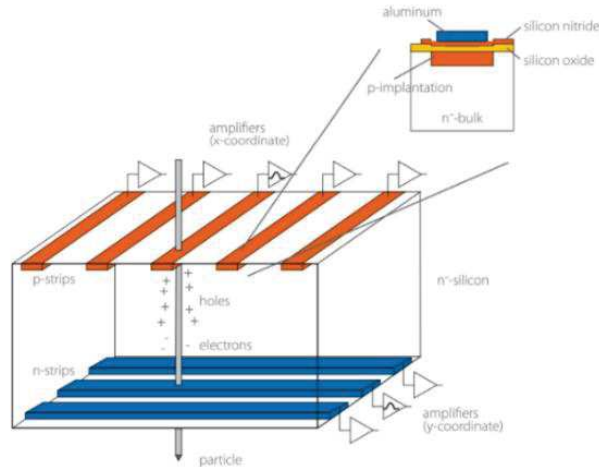


Figure 2.9: Operation principle of a double-sided strip detector [17].

2.5.2 CCD

CCDs are built in a pixel array structure based on blocks of MOS capacitors. As shown in figure 2.10, each pixel is subdivided into three parts by gate elements. Positive voltages are applied to gates to generate potential wells in the substrate. Electrons created by incident particles are stored in potential wells, which is illustrated as a collection of grey. The charge is transferred along each column from pixel to pixel to the read-out node via controlling voltages of gates.

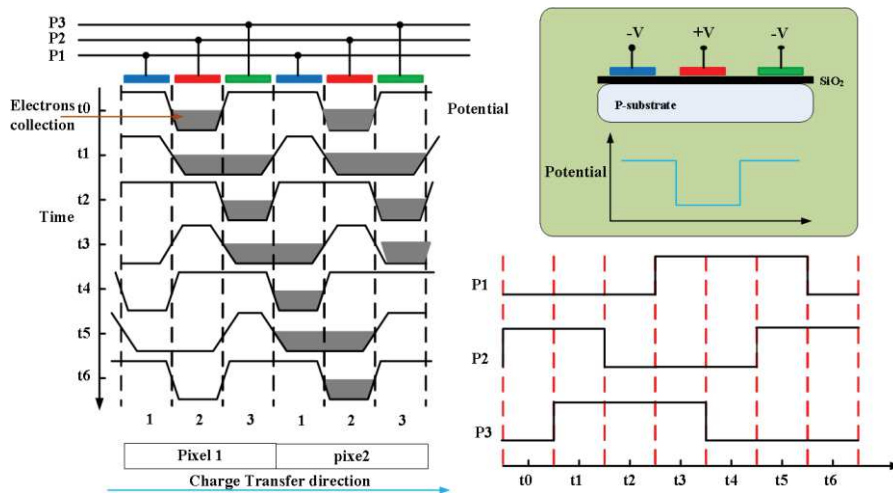


Figure 2.10: Timing diagram of voltage schemes to transport charge through a three-phase CCD.

The timing diagram to transport charges through a three-phase CCD system is shown in figure 2.10. Three gates in each pixel are controlled by the clock signal P1, P2

and P3, respectively. All pulsed of three clock signals have a duty cycle of 50% and their mutual phase shift is 120 degree. At $t(0)$, signal P1 and P3 are held low while signal P2 is held high. A potential well is created under the gate controlled by P2 of pixel 1. At $t(1)$, signal P3 is lifted to the high level to make the charge transport from the gate to the next one [18][19].

CCD structures were first used in the vertex detector of the NA32 experiment in 1983, and then 96 two-dimensional CCDs with a total of 307 Mpixel were used in the SLD's upgraded vertex detector [20].

2.5.3 Hybrid Pixel Sensor

Gaalema proposed a readout chip that can be used with the *Ge* PIN array to perform X-ray inspection, which is the first demonstration of the concept of a hybrid detector [21][22]. A schematic diagram of a single pixel of a hybrid detector is shown in figure 2.11, where a sensor part is connected to a readout electronics part by using the bump-bonding process. In the sensor part, electrons and holes are separated by a bias voltage applied to electrodes. Charge signals are converted and processed in the read-out electronic part. The material and manufacturing processes of the two parts can be optimized separately targeting at different applications [23].

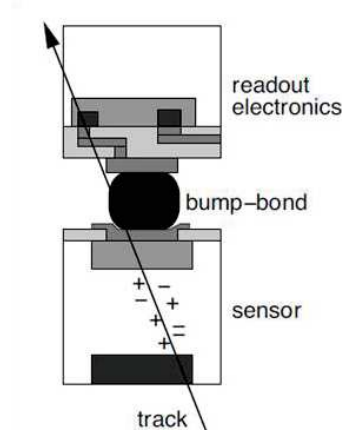


Figure 2.11: A simplified schematic diagram of a single pixel in a hybrid silicon detector, it is composed of a sensor part and a readout electronics part [24].

In 1992, hybrid detectors were first successfully tested in the heavy-ion experiment WA94 [25]. Four experiments installed on the Large Hadron Collider (LHC) collider from 1998 to 2006 were equipped with hybrid pixel detectors [26].

2.5.4 DEPFET Sensor

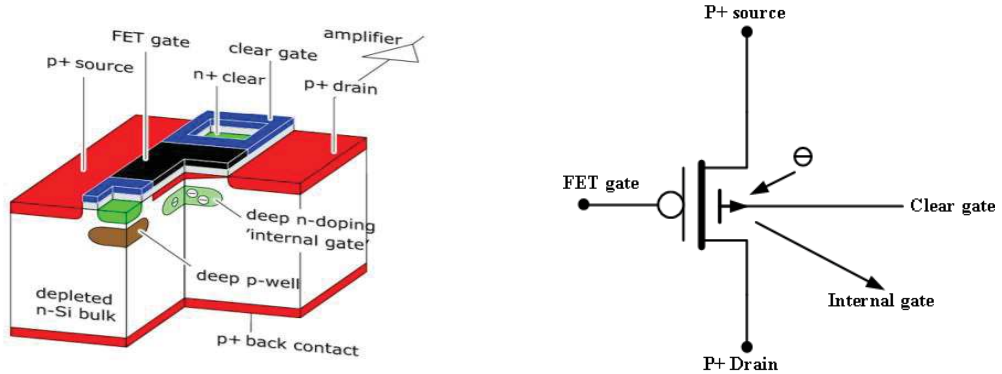


Figure 2.12: Schematic layout of the DEPFET [27].

DEPFET structures were proposed in 1980 by *J.Kemmer* and *G.Lutz* [28]. The schematic layout of a DEPFET is shown in figure 2.12. A Field Effect Transistor (FET) is integrated on the N-type depleted silicon bulk. There is a deep N-doping region under the FET gate named the internal or the second gate. Electrons generated by incident particles are collected by the internal gate. Modulation of the transistor channel current is generated as the potential of the internal gate varies. A positive voltage pulse is applied to the clear gate to reset electrons [3][27][29].

Vertex detectors in the BELLE II being installed will contain two layers of highly granular DEPFET Pixel Detector (PXD) [2]. The requirement of spatial resolution is 15 μm , the PXD will have pixel sizes of $50 \times 50 \mu\text{m}^2$ (Layer 1) and $50 \times 75 \mu\text{m}^2$ (Layer 2) in order to achieve the resolution.

2.5.5 Monolithic Active Pixel Sensor

In 2000, researchers of the *LEPSI* and *IReS* proposed a Monolithic Active Pixel Sensor (MPAS) for charged particle tracking and imaging [30]. The MAPS structure integrates signal sensing and readout electronics on the same substrate. They offer an attractive balance among granularity, material budget, radiation tolerance and readout speed [31].

Sensor diode

A schematic of the first-generation of MAPS structure is shown in figure 2.13. A photodiode is formed by the P-N junction generated between the N-well and the epitaxial layer (P-type). Doping levels of P-well (P+ type) and P-substrate (P++ type)

are higher than the epitaxial layer (P- type), leading to the generation of two potential barriers. A potential barrier is located at the boundary region between the epitaxial layer and the P-well. The other potential barrier is located at the boundary region between the epitaxial layer and the P-substrate.

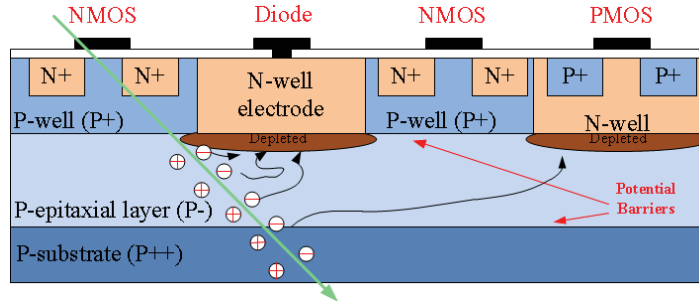


Figure 2.13: Schematic of the first-generation MAPS structure.

A charged particle traverses the MAPS detector, the energy released by the particle are converted and typically ~ 80 electron-hole pairs are generated per micron. Electrons created in the epitaxial layer diffuse thermally and gather at the N-well collection electrode. Due to the high level of the P-type doping, more of electrons generated in the substrate are recombined, just few electrons can drift to the epitaxial layer and be collected by the collection electrode.

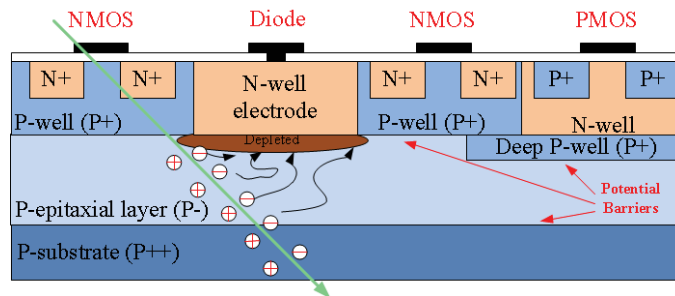


Figure 2.14: Schematic of the second-generation MAPS structure.

In the first-generation MAPS structure, only NMOS transistor can be used in a pixel. An N-well which is used to host PMOS transistor would compete for charge collection with N-well/P-epi diodes. In order to avoid this situation, a deep P-well in the P-substrate is proposed to shield the N-well from the epitaxial layer or substrate in the second-generation structure, as shown in figure 2.14. The deep P-well prevents the N-well from collecting electrons, therefore allowing the use of full complementary CMOS in the pixel [30][32][33].

In pixelated detectors, the electrons diffusion leads to the charge can be shared by two or more pixels. Especially for smaller pixel size detectors, the effect of charge

sharing will be more prominent.

Read-out circuit

A typical in-pixel readout circuit for MAPS structures is shown in figure 2.15, which is composed of three transistors. M1 is controlled by the signal RESET to reset the sensing diode. M2 connected to the sensing diode is an input transistor of a source follower. M3 is controlled by the signal ROW_SEL to select the row of pixel to output.

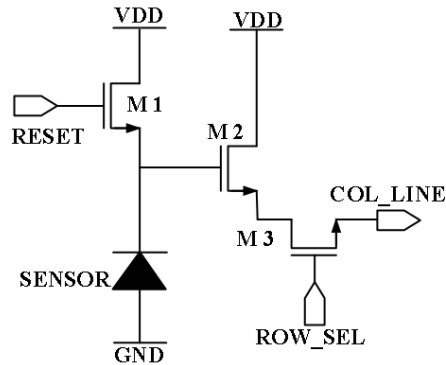


Figure 2.15: Typical in-pixel readout circuit [30].

The MAPS structure was first used in the vertex detector upgrade of the STAR (Solenoidal Tracker at RHIC) experiment at RHIC (Relativistic Heavy Ion Collider). The ALPIDE used in the ALICE experiment is a monolithic pixel sensor will be fabricated in the 180 nm CMOS imaging sensor process of TowerJazz. It achieves detection efficiency above 99%, the power consumption less than 40 mW/cm², a spatial resolution of around 5 μm. These features all have met even exceeded requirements of the ALICE experiment, even after neutron irradiation to 1.7×10^{13} 1 MeV n_{eq}/cm² [34].

2.5.6 Conclusions

Single-sided strip detector measures 1 coordinate, while Double-sided strip detector could give a 2-dimensional position of a particle track. However, the measurement will be ambiguous, Ghost hits, if more than one particle hits the strip. Due to the complicated manufacturing procedures, the expensive cost is needed for the Double-sided strip detector [35]. A limitation for CCD is low readout speed which depends on the size of the pixel matrix. The charge has to be transferred for long distances in columns of pixels before reaching the readout line. The Charge Transfer Efficiency (CTE) is used to measure the quality of the charge transported from one

pixel to another, which should be close to 1. CCD is sensitivity to radiation damage, which makes the charge transfer efficiency degradation. The hybrid pixel sensor provides low detector capacitance, low leakage current and large signal-to-noise ratio. Due to a large number of readout channels, large power consumption and expensive cost are needed [36]. The DEPFET provides an excellent low noise performance which can achieve a good spatial resolution and a fast readout speed [37]. The DEPFET detector is not used in a hadron collider since its performance can be destroyed by additional charges from the radiation damage [6]. Functions of the sensor and amplifier are combined in the detector. The MAPS structure is manufactured using standard CMOS technology, leading to some attractive features including low cost, low material budget, simple readout architecture, high spatial resolution, etc. And the technology makes it possible to integrate more processing module into circuit. Our concept is to integrate the ANN into a CMOS pixel sensor to reconstruct the incident angle and tag the hits generated by particles from the beam background.

Table 2-1: Advantages and disadvantages of these detector technologies [6].

<i>Technology</i>	<i>Advantages</i>	<i>Disadvantages</i>
<i>Strip detector</i>	Large area possible Fast speed	Expensive cost
<i>CCD</i>	Industry standard High spatial resolution Integrated amplification	Slow speed Not radiation hard Large power consumption Need different voltages
<i>Hybrid pixel</i>	low detector capacitance low leakage current large signal-to-noise ratio	Large channel number large power consumption Expensive cost
<i>DEPFET</i>	Integrated amplification Low power consumption Low noise Fast readout speed	Only small devices Not radiation hard High power at CLEAR No industry standard
<i>MAPS</i>	Standard IC process Integrated amplification Low noise Low power High spatial resolution	Only small devices

2.6 Summary

Basic properties and types of semiconductor detectors (Si detector) are described in the chapter. Generation and transportation of carriers are described. Basic components, the P-N junction and the MOS structure, also introduced. Typical silicon detectors used for HEP experiments are introduced and compared. Artificial neural networks will be introduced briefly in the next chapter.

2.7 Bibliography

- [1]. Knoll, Glenn F. *Radiation detection and measurement*. John Wiley & Sons, 2010.
- [2]. Hartmann, Frank. "Silicon tracking detectors in high-energy physics." *Nuclear Instruments and Methods in Physics Research Section A: Accelerators, Spectrometers, Detectors and Associated Equipment* 666 (2012): 25-46.
- [3]. Moser, Hans-Günther. "Silicon detector systems in high energy physics." *Progress in Particle and Nuclear Physics* 63.1 (2009): 186-237.
- [4]. Michael Moll, "An introduction to Silicon Detectors with focus on High Energy Physics applications, " *SIMDET 2016*, 05-07 September 2016, LPNHE Paris.
- [5]. Lütz, G. "Semiconductor radiation detectors: Device physics." (2007).
- [6]. Hartmann, Frank. *Evolution of silicon sensor technology in particle physics*. Vol. 231. Springer, 2008.
- [7]. Amsler, C., and Particle Data Group. "1 (2008) and 2009 partial update for the 2010 edition. PL B667." (2009).
- [8]. Neamen, Donald A. *Semiconductor physics and devices: basic principles*. New York, NY: McGraw-Hill,, 2012.
- [9]. Spieler, Helmuth. *Semiconductor detector systems*. Vol. 12. Oxford university press, 2005.
- [10]. Van Zeghbroeck, Bart. "Principles of semiconductor devices." *Colorado University* 34 (2004).
- [11]. Ortiz-Conde, Adelmo, et al. "Revisiting MOSFET threshold voltage extraction methods." *Microelectronics Reliability* 53.1 (2013): 90-104.
- [12]. Kemmer, Josef. "Fabrication of low noise silicon radiation detectors by the planar process." *Nuclear Instruments and Methods* 169.3 (1980): 499-502.
- [13]. Silvia Masciocchi, " Semiconductor detectors - 3", SS2017, Heidelberg June 14, 2017.
- [14]. <http://www.hephy.at/user/friedl/diss/html/node21.html>
- [15]. Vito Manzari, " Silicon Detectors Lecture 2" , *The 5th Egyptian School on High Energy Physics*, 14 – 19, November 2015 Egypt.
- [16]. Moser, Hans-Günther. "Experience with the ALEPH silicon vertex detector." *Nuclear Instruments and Methods in Physics Research Section A: Accelerators, Spectrometers, Detectors and Associated Equipment* 310.1-2 (1991): 490-492.
- [17]. "5. Silicon Strip Detectors, " MPI HLL

- [18]. Theuwissen, Albert J. *Solid-state imaging with charge-coupled devices*. Vol. 1. Springer Science & Business Media, 2006.
- [19]. Janesick, James R. *Scientific charge-coupled devices*. Vol. 117. Bellingham: SPIE press, 2001.
- [20]. Abe, Koya, et al. "Design and performance of the SLD vertex detector: a 307 Mpixel tracking system." *Nuclear Instruments and Methods in Physics Research Section A: Accelerators, Spectrometers, Detectors and Associated Equipment* 400.2-3 (1997): 287-343.
- [21]. Gaalema, Steve. "Low noise random-access readout technique for large PIN detector arrays." *IEEE Transactions on Nuclear Science* 32.1 (1985): 417-418.
- [22]. Heijne, Erik HM. "Semiconductor micropattern pixel detectors: a review of the beginnings." *Nuclear Instruments and Methods in Physics Research Section A: Accelerators, Spectrometers, Detectors and Associated Equipment* 465.1 (2001): 1-26.
- [23]. Awadalla, Salah. *Solid-state radiation detectors: technology and applications*. CRC Press, 2015.
- [24]. Wermes, Norbert. "Pixel detectors for charged particles." *Nuclear Instruments and Methods in Physics Research Section A: Accelerators, Spectrometers, Detectors and Associated Equipment* 604.1-2 (2009): 370-379.
- [25]. Beker, H., et al. "A hybrid silicon pixel telescope tested in a heavy-ion experiment." *Nuclear Instruments and Methods in Physics Research Section A: Accelerators, Spectrometers, Detectors and Associated Equipment* 332.1-2 (1993): 188-201.
- [26]. Delpierre, P. "A history of hybrid pixel detectors, from high energy physics to medical imaging." *Journal of Instrumentation* 9.05 (2014): C05059.
- [27]. M. Vos et al., DEPFET active pixel detectors, *PoS(VERTEX 2009)015*.
- [28]. Kemmer, J., and Gerhard Lutz. "New detector concepts." *Nuclear Instruments and Methods in Physics Research Section A: Accelerators, Spectrometers, Detectors and Associated Equipment* 253.3 (1987): 365-377.
- [29]. Wermes, Norbert, et al. "New results on DEPFET pixel detectors for radiation imaging and high energy particle detection." *IEEE Transactions on Nuclear Science* 51.3 (2004): 1121-1128.
- [30]. Turchetta, R., et al. "A monolithic active pixel sensor for charged particle tracking and imaging using standard VLSI CMOS technology." *Nuclear Instruments and Methods in*

Physics Research Section A: Accelerators, Spectrometers, Detectors and Associated Equipment 458.3 (2001): 677-689.

- [31]. Hu-Guo, Ch, et al. "CMOS pixel sensor development: a fast read-out architecture with integrated zero suppression." *Journal of Instrumentation* 4.04 (2009): P04012.
- [32]. Snoeys, W. "CMOS monolithic active pixel sensors for high energy physics." *Nuclear Instruments and Methods in Physics Research Section A: Accelerators, Spectrometers, Detectors and Associated Equipment* 765 (2014): 167-171.
- [33]. Cavicchioli, C., et al. "Design and characterization of novel monolithic pixel sensors for the ALICE ITS upgrade." *Nuclear Instruments and Methods in Physics Research Section A: Accelerators, Spectrometers, Detectors and Associated Equipment* 765 (2014): 177-182.
- [34]. Mager, M., and ALICE Collaboration. "ALPIDE, the Monolithic Active Pixel Sensor for the ALICE ITS upgrade." *Nuclear Instruments and Methods in Physics Research Section A: Accelerators, Spectrometers, Detectors and Associated Equipment* 824 (2016): 434-438.
- [35]. Thomas Bergauer. "Silicon Detectors in High Energy Physics", HEPHY Vienna.
http://www.hephy.at/fileadmin/user_upload/Lehre/Unterlagen/Detektoren_Bergauer/2018/VO-4-2018-SemiconductorDetectors.pdf
- [36]. Doris Eckstein. "Solid State Detectors.", DESY.
http://www.desy.de/~garutti/LECTURES/ParticleDetectorSS12/L6_SiliconLecture.pdf
- [37]. Richter, Rainer Helmut, et al. "Design and technology of DEPFET pixel sensors for linear collider applications." *Nuclear Instruments and Methods in Physics Research Section A: Accelerators, Spectrometers, Detectors and Associated Equipment* 511.1-2 (2003): 250-256.

3 Artificial Neural Networks for Pattern Recognition

Artificial Neural Networks (ANNs) are computational modules that are inspired by the biological neural network [1]. ANNs, consisting of processing units and connections (weights) between these units, have been proved to be universal approximators for a domain of boolean function by the logical calculus [2]. ANNs used nowadays are evaluated and developed on the basis of the computational model introduced by *Warren McCulloch* and *Walter Pitts* in 1943 [3] and have been used in a wide variety of field for pattern recognition successfully, including finance, weather, control, medicine, physics, etc [4][5][6][7].

My thesis propose to integrate ANNs into a CMOS pixel sensor for tagging and removing hits generated by particles from the beam background. In this chapter, firstly, the basic principle of artificial neurons are introduced; Next, the Multi-Layer Perceptron (MLP) which is employed in the thesis, is described; Then, ANN supervised learning modes and the Back Propagation (BP) algorithm are illustrated. Finally, ANN applications in the field of high energy physics (HEP) are reviewed briefly.

3.1 Pattern Recognition

Human beings can perform some tasks such as reading hand-written digits, recognizing traffic signals, etc. Decision processes made by human beings are related to the identification of patterns in the brain. Pattern recognition is an attempt to grasp the

mechanism of decision-making processes and build machines that can perform decisions like human beings [8][9].

“Pattern recognition is about assigning labels to objects. Objects are described by a set of measurements called also attributes or features” [10]

When a charged particle passes a CMOS pixel sensor, electrons generated are collected by several pixels. These pixel values constitute a cluster which presents hit information of the charged particle. As shown in the figure 3.1, each cluster shape is represented in a 5×5 pixels matrix. Due to the charged particle from the beam background have lower momentum than the particle from the physics event, resulting to generating an elongated cluster shape. We proposed to regress the incident angle of each cluster by the artificial neural network and then tag and remove hits generated by charged particles from the beam background.

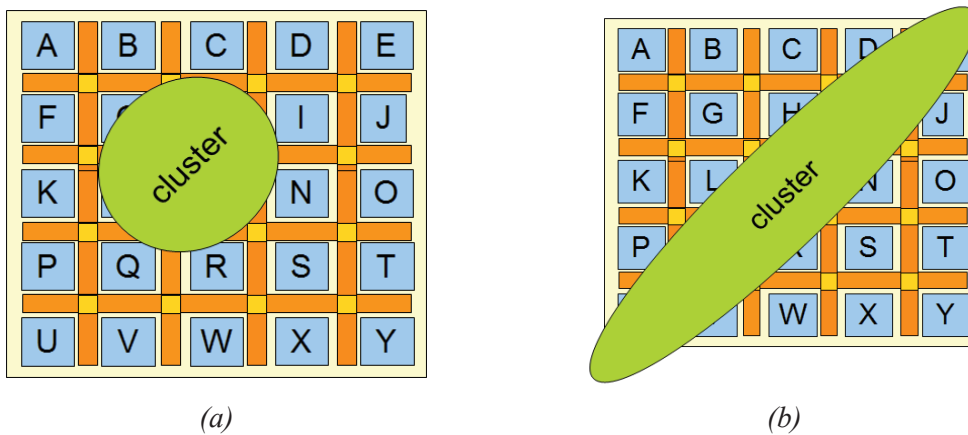


Figure 3.1: Examples of cluster shapes (a) Cluster shape generated by charged particles from the physics event (b) Cluster shape generated by charged a charged particle from the beam background.

Procedures of pattern recognition are divided into two phases: training and test. As for the example shown in figure 3.1, in the training phase, training datasets consisting of lots of cluster shapes and their corresponding incident angles are used to train parameters (weights) of the machine. Inputted cluster shapes are classed in advance and their incident angles are known. In the test phase, incident angles are recognized based on inputted cluster shapes and the weights of the artificial neural network.

In general, pattern recognition is separated into two categories (classification and regression) according to tasks: In classification tasks, inputs of the machine are assigned to discrete classes and outputs represent labels of discrete classes. In

regression tasks, outputs are values of continuous variables [11].

3.2 Biological and Artificial Neuron

In human brains, biological neural networks which perform decision-making processes consist of basic components of the biological neuron. Inspired by the biological neuron, artificial neuron models are proposed and developed as the basic unit of the ANN. Principles of biological neurons and artificial neurons are introduced in the section.

3.2.1 Biological Neurons

A human brain has an average of ~100 billion biological neurons that emerge a wide variety of shapes and sizes in different parts. Biological neurons are interconnected by synapses. For instance, the pyramidal cell is one of the most common types of cortical neurons, which can receive 10000 or more synapses [12].

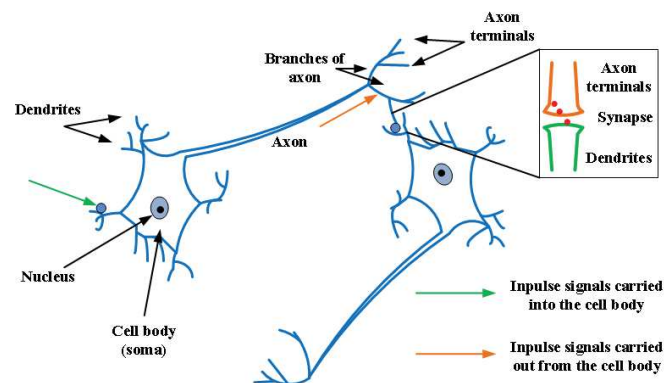


Figure 3.2: Connections between two biological neurons.

Two biological neurons are shown in figure 3.2. Every biological neuron is a single processing unit. A biological neuron consists of a cell body (soma), an axon and dendrites. The cell body contains a nucleus which is used to control the cell activity. Dendrites are used to carry impulse signals generated by other neurons into the cell body and the axon is used to take impulse signals out from the cell body [12]. The synapse between the dendrite and an axon terminal of another neuron is used to convert the electrical signal into a chemical signal, release a neurotransmitter.

The process of the signal generated and transported in a biological neuron as

follows: Firstly, neurotransmitters released by previous neurons diffuse across the synapse. Then, in the receiver neuron, according to the neurotransmitters, input impulse signals are generated and transmitted to the cell body. The receiver neuron will be activated if the sum of impulse signals exceeds a threshold. Finally, an output impulse signal is generated in the cell body and transmitted to the axon. The input impulse signals can be inhibitory or exciting by neurotransmitters depending on the type of a synapse. Synapses have the function to learn from activities that they have participated since their effectiveness is adjusted by impulse signals transported in cell bodies [13][14].

3.2.2 Artificial Neuron

Artificial neurons, basic components of ANNs, are designed and developed inspired by the biological neuron. According to the constitution and function, three elements of an artificial neuron model are identified as follows:

1. Weights. For a biological neural network, two neurons are connected by a synapse which can be trained by activities. For an artificial neuron, the effect of a synapse is embodied by the weight between two neurons.
2. A summing junction. For a biological neuron, input impulse signals are summed up and compared with the threshold. For an artificial neuron, inputs are weighted and then added together in a summing junction.
3. An activation function. For a biological neuron, a threshold function is used to determine the neuron is activated or not. For an artificial neuron, including threshold or other nonlinear functions can be used as activation functions.

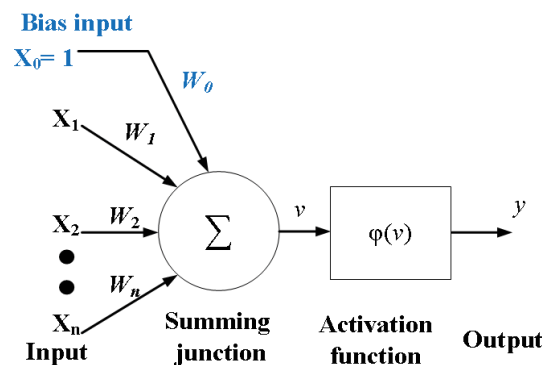


Figure 3.3: Computational model of artificial neurons.

A computational model of artificial neurons is shown in figure 3.3, where x_1, x_2, \dots, x_n are inputs, x_0 is a fixed bias input. w_0, w_1, \dots, w_n are corresponding weights. The value of the summing junction (v) is calculated as

$$v = \sum_{i=1}^n x_i \times w_i + x_0 \times w_0 . \quad (3 - 1)$$

Then, the value of the summing junction (v) is fed into the activation function ($\varphi(x)$), y is the output of the artificial neuron, expressed as

$$y = \varphi(v) . \quad (3 - 2)$$

3.2.3 Activation Function

Activation functions $\varphi(x)$ determine the output of an artificial neuron. In the section, two types of activation functions for artificial neuron models are described.

Threshold activation function

The threshold activation function is presented in formula (3-3). If the input is nonnegative, the output of the activation function is 1, otherwise, the output is 0.

$$\varphi(x) = \begin{cases} 1 & \text{if } x \geq 0 \\ 0 & \text{if } x < 0 \end{cases} \quad (3 - 3)$$

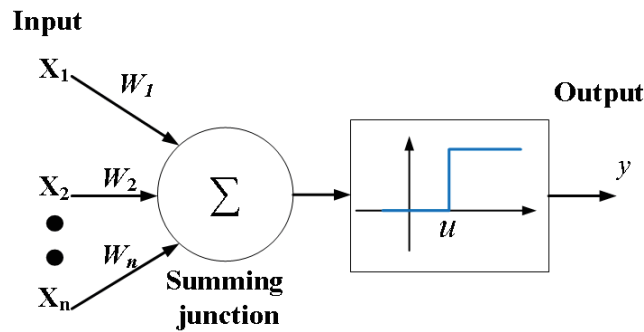


Figure 3.4: McCulloch-Pitts model of an artificial neuron.

The artificial neuron employed with the threshold activation function is named McCulloch-Pitts model which was proposed in 1943 by *McCulloch* and *Pitts*. As shown in figure 3.4, where X_1, X_2, \dots, X_n are inputs, y is the output, w_1, w_2, \dots, w_n are corresponding weights to inputs, $\varphi(x)$ is the threshold activation function, u presents a certain threshold. The output of the McCulloch-Pitts model is expressed as

$$y = \varphi \left(\sum_{i=1}^n w_i \times X_i - u \right). \quad (3-4)$$

The certain threshold (u) can be thought of as the product of the fixed bias input and its weight ($X_0 \times W_0$, see figure 3.3).

Sigmoid Activation Function

Sigmoid functions represent a category of activation functions whose shapes are letter "S" (see figure 3.5). They are most commonly used for nonlinear tasks and present a balance between linear and nonlinear behaviour [14]. Common sigmoid functions contain *Uni-polar sigmoid*, *Bi-polar sigmoid* and *Tanh*. Expressions of these sigmoid activation functions are shown in formula (3-5), (3-6) and (3-7) [15].

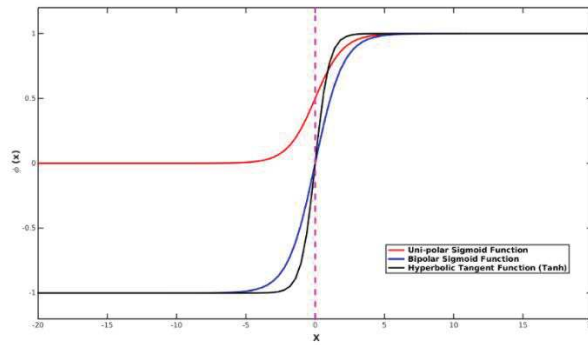


Figure 3.5: Sigmoid activation functions.

- Uni-Polar Sigmoid Function

$$\varphi(x) = \frac{1}{1 + e^{-x}}, \quad x \in (-\infty, \infty), \quad \varphi(x) \in (0,1). \quad (3-5)$$

- Bipolar Sigmoid Function

$$\varphi(x) = \frac{1 - e^{-x}}{1 + e^{-x}}, \quad x \in (-\infty, \infty), \quad \varphi(x) \in (-1,1). \quad (3-6)$$

- Hyperbolic Tangent Function (Tanh)

$$\varphi(x) = \tanh(x) = \frac{e^x - e^{-x}}{e^x + e^{-x}}, \quad x \in (-\infty, \infty), \quad \varphi(x) \in (-1,1). \quad (3-7)$$

3.3 Types of Artificial Neural Networks

The ANN is viewed as a computing system composed of many interconnected artificial neurons. In 1994, *Simon Haykin* provided a definition of a neural network which was adapted from *Aleksander and Morton* (1990): [8][14][16]

“A neural network is a massively parallel distributed processor made up of simple processing units that has a natural propensity for storing experiential knowledge and making it available for use. It resembles the brain in two respects:

1. *Knowledge is acquired by the network from its environment through a learning process.*
2. *Interneuron connection strengths, known as synaptic weights, are used to store the acquired knowledge.”*

According to connection architectures, ANNs can be grouped into two categories: Feedforward networks and Feedback networks, as shown in figure 3.6.

In the feedforward network, the signal flow is in the direction from input neurons to output neurons. The output of feedforward networks is independent of previous network states, which means that there is no signal loop and output is produced only based on inputs. Typical examples of feedforward networks contain the Single Layer Perceptron, the Multi-Layer Perceptron (MLP) and the Radial Basis Function Nets.

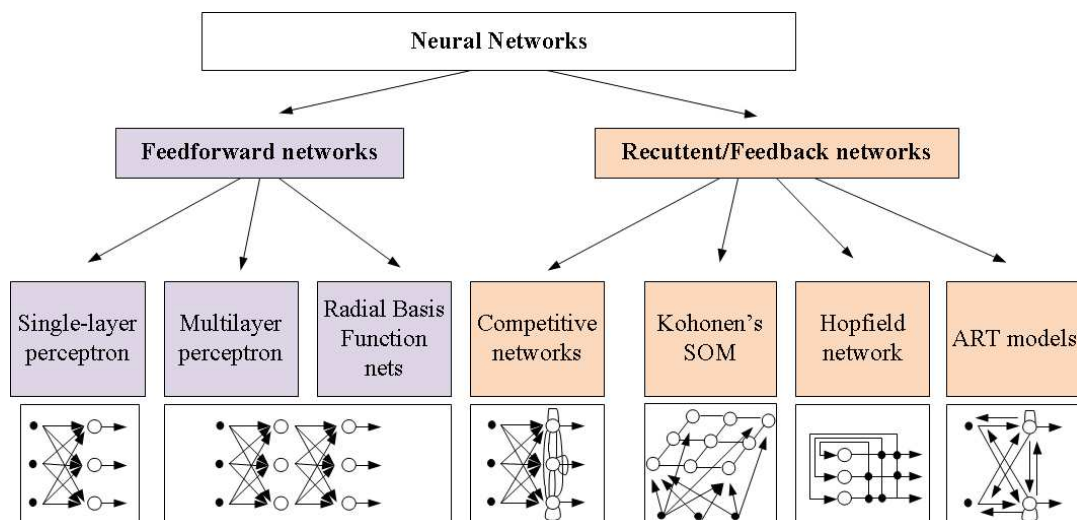


Figure 3.6: Taxonomy of feedforward and feedback network architectures [13].

In the feedback network, the output of one neuron is connected with inputs of neurons of previous layers. The output of feedback networks is produced based on inputs and the previous network state [17]. Typical examples of the feedback network contain Hopfield networks, Kohonen's SOM, ART model [13].

3.3.1 Multi-Layer Perceptron (MLP)

The Multi-Layer Perceptron (MLP) has been employed in a variety of applications, which is commonly composed of an input layer, an output layer and some hidden layers. The architectures of a typical MLP with a single hidden layer are presented in figure 3.7. A MLP structure was used in my thesis for reconstructing incident angles of charged particles. Neurons of the input layer take features extracted from an object into the system. Main calculation processes are accomplished in the hidden layer which is composed of artificial neurons. The weight between every two neurons in different layers are supplied according to the learning rule of the neural network [18][19]. The result of the output neuron indicates a class label (classification tasks) of the object or an accurate value (regression tasks).

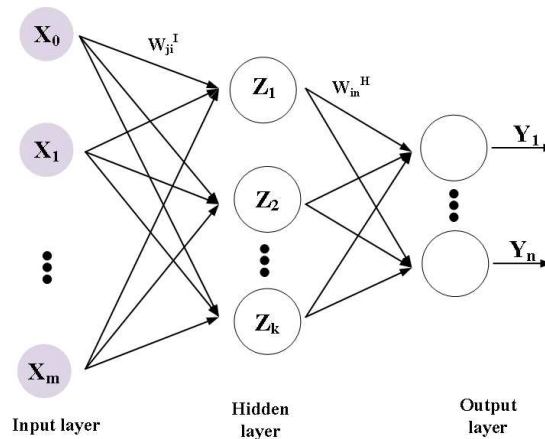


Figure 3.7: Connection architectures of Multi-Layer Perceptron.

An output (Y_n) of the MLP is calculated as shown in formula (3-8). In a hidden neuron, weighted inputs including the input bias connection ($W_{oi}^I \times X_0$) are summed up, then fed into an activation function module. In an output neuron, outputs of all hidden neurons are weighed, then only summed up [20] or then fed into an activation function. It can be found that there is no activation function achieved for output neurons in the formula.

$$Y_n = \sum_{i=0}^k \left(w_{in}^H \times \varphi \left(\sum_{j=0}^m (w_{ji}^I \times X_j) \right) \right), \quad (3 - 8)$$

where

w_{ji}^I is the weight connecting input neuron j to hidden neuron i .

w_{in}^H is the weight connecting hidden neuron i to output neuron n .

3.4 Feature Extraction

Feature extraction is one of preprocessing procedures for the ANN. In the issues of artificial neural networks, feature extraction makes important role in the regression or classification of data with a high dimension. In general, input variables of the artificial neural network have some correlations, the feature extraction make reduction on the dimensionality of inputs via producing a set of features. Simultaneously, these features should keep enough characteristics of input variables for the regression or classification problems [21][22].

We proposed to regress the incident angle of a charged particle by the MLP. As shown in figure 3.1, a cluster is composed by 5×5 pixels. If there is no procedure of feature extraction, values of the matrix (5×5 pixels) need to be fed into the artificial neural network as inputs.

In order to reduce the computational complication and to improve the generalization ability of classifiers, feature extraction is implemented in our design. The feature extraction procedure is applied to the original input variables, which reduces inputs by selecting and combing some original variables. The feature extraction procedure is considered as a mapping process from the n -dimensional space to a lower-dimension feature space [9][11][23]. Some features of a cluster shape are extracted to represent hit information. As shown in figure 3.8, the same feature extraction procedure is implemented in both the training and the test phase. The feature extraction process, including zooming, shaping, etc, reduces the complexity of input variables and speeds up the computation process of the system. It has been approved that the feature-based pattern recognition system operates much faster than a pixel-based system [24].

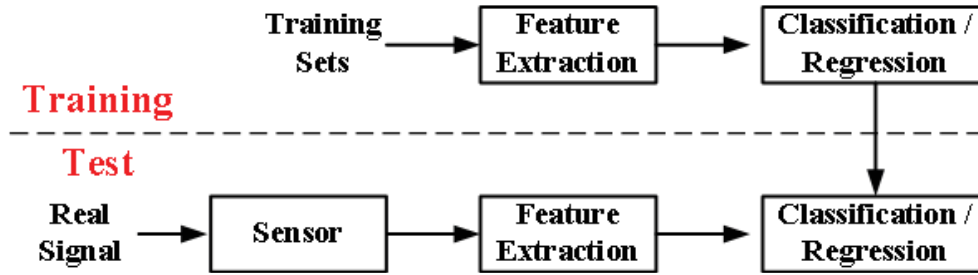


Figure 3.8: Training and test phase [25].

Principal component analysis (PCA), or Main Component Analysis (MCA), is a statistical method for feature extraction which has been used in various applications. It converts a set of possibly correlated variables into a set of linearly uncorrelated variables (principal components) by an orthogonal transformation. The targets of PCA are to extract the most important information from correlated variables, compress the size of the data set [26]. The principal components are linear combinations of variables with maximal variance. It means to find the “main axis” of the cluster shape. Projection on the principal axis explains more of the variance of the data than projection on any other axis [27].

3.5 ANN Supervised Learning

The ANN classifies labels or calculates values based on input variables and weights. There are two approaches to train weights of an ANN: supervised and unsupervised. And the supervised learning is employed in our design to train the ANN.

Supervised learning means that the ANN is trained with a "teacher". In the training dataset, input vectors and outputs (class labels or target results) of the ANN all are specified. The learning method is implemented for setting the weights of the artificial neural network. The errors of all artificial neurons are minimized continuously by iteration until the accuracy of output neurons are acceptable.

In the forward phase, initial weights between every two neurons are chosen randomly at the beginning of the training process. The signal is forward propagated from input neurons to output neurons. Inputs are fed into the ANN and the actual output is calculated based on initial weights.

In the backward phase, the error between the actual output and the specified target result is calculated. The weight is adjusted to generate a closer error between the

desired and the actual output for the next iteration.

This training procedure is finished until the ANN achieve an acceptable accuracy of actual outputs for a given input set. The supervised learning procedure is used in our design by software. The weights of the MLP will be settle down if the incident angle reconstructed by the MLP is acceptable compared with the real incident angle.

Training datasets should be large and enough to contain all the cluster information to train weights of the artificial neural network. The feature extraction module is used to choose and extract enough features of a cluster to represent hit information. In our design, features of each cluster are determined and optimized according to the training procedure implemented in the software [9][14][28].

3.5.1 BP Algorithm

For the approach of supervised learning, the Back-Propagation (BP) algorithm is the most efficient learning algorithm for the backward phase to minimize errors of all artificial neurons in the MLP due to its simplicity.

The mechanism of the BP algorithm was presented by *P. Werbos* in his Ph.D. thesis to make a learning algorithm for a network [29]. The term “back propagation” was developed after 1985 and popularized by a book entitled *Parallel Distributed Processing* [30][31][32].

The BP algorithm applied in the MLP performs as follows:

1. An MLP structure is designed, and weights are initialized;
2. A set of training example inputs are chosen and fed into the MLP;
3. The example inputs are propagated in the forward phase and obtained the actual output;
4. The error between specified target result and the actual output is calculated according to an error function, and then propagated in the backward phase layer by layer;
5. The gradient of the error function with respect to the weight is calculated. Weights are adjusted to minimize the overall error signal;
6. Above steps are repeated according to different example inputs to update weights until the error signal is satisfactorily small [33][34].

In the training procedure, gradient descent is used to optimize weights to minimize

the error function. Weights are adjusted iteratively by operating in many times to the training dataset. Weights are updated as the formula:

$$w(t) = w(t - 1) + \Delta w(t) , \quad (3 - 9)$$

where

t is one iteration in the training process.

w is the weight to be updated.

Weights are updated to find a local minimum result by applying correction $\Delta w(t)$ to $w(t)$. The correction is proportional to the negative of the gradient of the error function at the current point, it is calculated as follows:

$$\Delta w(t) = -\eta \frac{\partial \xi(n)}{\partial w(n)} , \quad (3 - 10)$$

where

$\xi(n)$ is the error function between the specified target result and the actual output.

$w(n)$ is the weight to be updated.

η is the learning rate parameter of the back-propagation algorithm. It represents the size of the steps taken and the minus signal in the formula means gradient descent in the weight space.

The error signal between the specified target result and the actual output of neuron j is calculated as

$$e_j(n) = d_j(n) - y_j(n) , \quad (3 - 11)$$

where

$d_j(n)$ is the specified target result of the neuron j for the training example number n .

$y_j(n)$ is the actual output of the neuron j for the training example number n .

The error function of neuron j is expressed as

$$\xi_j(n) = \frac{1}{2} e_j^2(n). \quad (3 - 12)$$

The error function of the whole ANN is calculated as

$$\xi(n) = \frac{1}{2} \sum_{j \in C} e_j^2(n), \quad (3 - 13)$$

where

C is the collection of all neurons in the output layer.

In the back phase for adjusting the network, the correction $\Delta w(t)$ presents the variety that will be applied on weights based on the error function. $\Delta w(t)$ of neuron j is calculated depending on the location of a neuron, divided into the output neuron and in the hidden neuron

Neuron j in the output layer

Corresponding connections of the output neuron j updated are shown in figure 3.9, where $X_0(n)$ is the input from the previous layer, $d_j(n)$ is the specified target result of the neuron, $\varphi(x)$ is the activation function, $v_j(n)$ is the value of the summing junction. For the output neuron j , the specified target result is supplied by the training dataset.

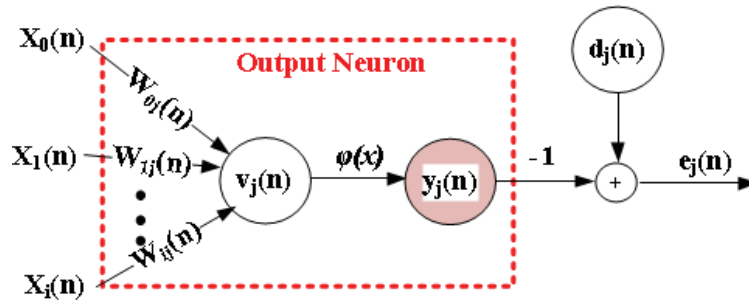


Figure 3.9: Signal-flow graph of output neuron j .

Value of the summing junction $v_j(n)$ in the neuron j is produced as

$$v_j(n) = \sum_{i=0}^m w_{ij}(n) \times x_i(n), \quad (3 - 14)$$

where

m is the number of inputs of neuron j .

$w_{ij}(n)$ is the weight between neuron i and neuron j . $w_{i0}(n)$ is the weight of the bias neuron in the previous layer.

The actual output value of the neuron j is calculated as

$$y_j(n) = \varphi_j(v_j(n)) , \quad (3 - 15)$$

where

φ_j is the activation function of the neuron j .

The back-propagation algorithm is used to minimize the error function $\xi(n)$ (see formula (3-13)). The gradient of the error function for weight is expressed as

$$\frac{\partial \xi(n)}{\partial w_{ij}(n)} = \frac{\partial \xi(n)}{\partial e_j(n)} \frac{\partial e_j(n)}{\partial y_j(n)} \frac{\partial y_j(n)}{\partial v_j(n)} \frac{\partial v_j(n)}{\partial w_{ij}(n)} = -e_j(n) \varphi'_j(v_j(n)) x_i(n) , \quad (3 - 16)$$

The correction $\Delta w_{ij}(n)$ applied to $w_{ij}(n)$ is expressed as

$$\Delta w_{ij}(n) = -\eta \frac{\partial \xi(n)}{\partial w_{ij}(n)} = \eta e_j(n) \varphi'_j(v_j(n)) x_i(n) . \quad (3 - 17)$$

Neuron j in the hidden layer

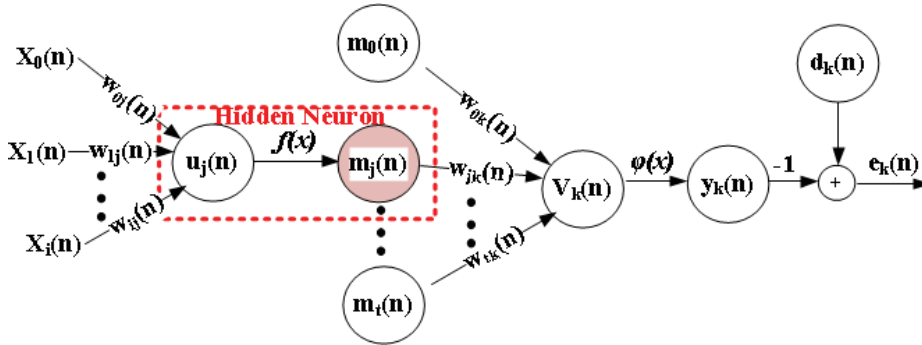


Figure 3.10: Signal-flow graph of hidden neuron j .

Corresponding connections of the hidden neuron j updated are shown in figure 3.10. Where $X_0(n)$ is the input from the previous layer, $d_k(n)$ is the specified target result of the output neuron k , $f(x)$ and $\varphi(x)$ are activation functions for the hidden neuron and the output neuron respectively, $m_j(n)$ and $V_j(n)$ are values of summing junctions in the hidden neuron and the output neuron respectively. For the hidden neuron, there is no specified target result, the error signal can be calculated recursively.

According to the definition of correction $\Delta w(t)$, it is calculated for the neuron j in the hidden layer as

$$\Delta w_{ij}(n) = -\eta \frac{\partial \xi(n)}{\partial w_{ij}(n)} = -\eta \frac{\partial \xi(n)}{\partial m_j(n)} \frac{\partial m_j(n)}{\partial u_j(n)} \frac{\partial u_j(n)}{\partial w_{ij}(n)} , \quad (3 - 18)$$

where

$$\frac{\partial m_j(n)}{\partial u_j(n)} = f_j'(u_j(n)). \quad (3-19)$$

$$\frac{\partial u_j(n)}{\partial w_{ij}(n)} = x_i(n). \quad (3-20)$$

$$\frac{\partial \xi(n)}{\partial m_j(n)} = \frac{\partial \xi(n)}{\partial e_k(n)} \frac{\partial e_k(n)}{\partial m_j(n)} = \sum_k e_k(n) \frac{\partial e_k(n)}{\partial v_k(n)} \frac{\partial v_k(n)}{\partial m_j(n)}. \quad (3-21)$$

The specified target result of neuron k is provided as $d_k(n)$. The error signal of the output neuron is calculated as

$$e_k(n) = d_k(n) - y_k(n) = d_k(n) - \varphi_k(v_k(n)). \quad (3-22)$$

$$\frac{\partial e_k(n)}{\partial v_k(n)} = -\varphi_k'(v_k(n)). \quad (3-23)$$

$v_k(n)$ for the output neuron k is calculated as

$$v_k(n) = \sum_{j=0}^t w_{jk}(n) \times m_j(n), \quad (3-24)$$

where

t is the number of inputs of output neuron k .

$w_{jk}(n)$ is the weight between hidden neuron j and output neuron t . $w_{0k}(n)$ is the weight of the bias neuron in the hidden layer.

$$\frac{\partial v_k(n)}{\partial m_j(n)} = w_{jk}(n). \quad (3-25)$$

3.6 ANN in HEP

ANNs were introduced in the field of HEP by *B. Denby* in 1988 [35], then they have been used for the physics study including finding tracks, data analysis and triggering applications, which widely used is the MLP based on the back-propagation algorithm [36].

Carsten Peterson proposed in the publication [37] that in the next generation of accelerators, very high multiplicity events need to be processed at an extremely rapid rate even after a low-level trigger. An ANN algorithm for finding tracks in high energy physics experiments was presented. Considering the development prospects of Very Large Scale Integration (VLSI), the author proposed to solve problems of particle trajectory search via the hardware implementation of the ANN structure.

In the offline data analysis, ANNs have been used for track and vertex reconstruction, particle identification and discrimination calorimeter energy estimation and jet tagging. An MLP neural network was the first used by a group from the DELPHI collaboration to classify decays of the Z into c , b , and s quarks. The MLP structure was composed of 19 input neurons, 25 hidden neurons and 3 output neurons that were used to encode the three classes of decays. Successful applications have prompted ANNs to play a role in the remaining three Large Electron-Positron (LEP) experiments [38][39]. In the Tevatron experiment, feedforward neural networks were used to measure the top quark mass or search leptoquarks. In the BaBar experiment, they were used to extract the result about the decay of B mesons [36][40][41].

The typical multilevel HEP trigger system is used to reject background events and obtain rare interesting events. The basic coincidence circuit is the component of a typical trigger system, which is similar to the Hopfield model of biological neurons. As shown in figure 3.11, a voltage divider circuit composed of four resistances converts the voltages from the four inputs voltage into a current I , and the current is converted to a voltage and presented. In the comparator, if the voltage (V_C) is above a threshold (V_{th}), a voltage level is expressed at the output of the unit. The weights of an ANN can be coded by the four resistor values (R_1 - R_4) in the voltage divider circuit [36].

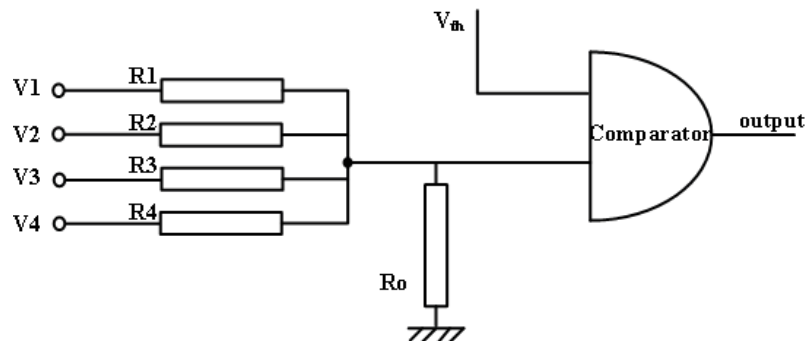


Figure 3.11: Basic coincidence electric circuit.

A commercial analog neural network chip named ETANN was tested by the group from the Fermilab. Track parameters of charged particles traversing a drift chamber

were found by the chip in real-time. The chamber was a prototype of the muon chamber for the D0 detector. There were 3 TVC voltages and 3 pad latch voltage as inputs, and 64 hidden neurons and 64 output neurons in the ANN structure. Since the limitation from the number of available neurons of the chip, track parameters obtained were not very efficient. However, it was not used in the actual physics experiment [42].

The experiments H1 in Hadron-Electron Ring Accelerator (HERA) was used to study the momentum distribution of constituents within the proton and measure the coupling strength of the gluon to the different quarks. A 4-level trigger system was used in order to reduce the high rate to about 100 Hz, in where the level-2 trigger was accomplished with a hardware ANN which was composed of 3 layers. The output of the neural network was used to separate physics events from the background. It was the first neural network trigger in a running HEP experiment [43].

In 2007, *E. Won* used a Xilinx SPARTAN XC3S4000 FPGA chip to implement an ANN structure [44], studied and discussed the feasibility for pattern recognition in the first-level trigger circuit. The 3-layer MLP structure contains 5 input neurons, 6 hidden neurons, and 1 output neuron. The ANN was trained completely on the software. Parameters, including the weight and threshold, are obtained. The ANN integrated with the FPGA hardware was tested. Due to a certain gap between the data width and the software, the accuracy of the recognition results of the ANN declined to some extent. However, the authors verified the possibility of applying the structure of the ANN to the trigger decision circuit of the first level. In the Belle experiment, the researchers applied ANN technology to the upgraded first-level full-trigger system [45][46].

3.7 Challenges for ANN Implementation

In our design, ANNs will be integrated into the hardware of a CPS for tagging and removing hits generated by particles from beam background. Challenges exist for implementing ANN into ASIC by digital circuit process.

Data precision. It is one important index for hardware implementation. For instance, low precision on weights means the design owes advantages on the power consumption, occupied surface and operation speed; high precision of weights leads to a highly reliable output by the final implementation. The final implementation is the result of a balance between performance and resource cost [47].

Mathematic unit. In the hardware implementation, mathematical units need to be achieved to perform complex calculation, including in feature extraction modules and activation function modules. For example, the sigmoid activation function needs complex mathematical units' implementation. Look-up-Table (LUT) method can be used in the hardware to present the mathematical unit, which means the low precision and long operation time. Or the mathematical method is alternative, which means approximates the nonlinear function by a combination of some linear functions. Inevitably, large power consumption and occupied surfaces are needed for implementing enough linear functions to reach a high-level precision. Mathematic unit implementations are a trade-off between power consumption, area and performance [48][49].

Learning procedure. Weights of the ANN can be trained by the off-chip or on-chip. By the off-chip method, weights are trained in the software and then transplanted into the hardware. The method can perform the training procedure fast and accurately. However, ANN structures and weights implemented in the hardware are fixed. By the on-chip method, the training procedure is processed by the hardware, which may result in low weight precision and large power consumption. However, compared to fixed weights generated by the off-chip solution, weights trained by on-chip can improve the real-time of the design [50].

3.8 Summary

In this chapter, relevant basic contents of ANNs are introduced, including the artificial neuron module and multi-layer perceptron structure. The feature extraction module is explained. Then the ANN supervised learning and back-propagation algorithm is illustrated. The ANN used in the high energy physics experiment is reviewed. The chapter is end up with the discussion of the challenges for ANN implementation in the ASIC.

In the next chapter, the ANN implementation in a FPGA device will be presented, the reconstructed results will be compared and analysed.

3.9 Bibliography

- [1]. van Gerven, Marcel, and Sander Bohte, eds. *Artificial neural networks as models of neural information processing*. Frontiers Media SA, 2018.
- [2]. Pospíchal, Jiří, and Vladimír Kvasnička. "70th Anniversary of Publication: Warren McCulloch & Walter Pitts-A Logical Calculus of the Ideas Immanent in Nervous Activity." *Emergent Trends in Robotics and Intelligent Systems*. Springer, Cham, 2015. 1-10.
- [3]. McCulloch, Warren S., and Walter Pitts. "A logical calculus of the ideas immanent in nervous activity." *The bulletin of mathematical biophysics* 5.4 (1943): 115-133.
- [4]. Sibanda, Wilbert, and Philip Pretorius. "Artificial neural networks-a review of applications of neural networks in the modeling of hiv epidemic." *International Journal of Computer Applications* 44.16 (2012): 1-9.
- [5]. Kamruzzaman, Joarder, ed. *Artificial neural networks in finance and manufacturing*. IGI Global, 2006.
- [6]. Devi, Ch Jyosthna, et al. "ANN approach for weather prediction using back propagation." *International Journal of Engineering Trends and Technology* 3.1 (2012): 19-23.
- [7]. Roe, Byron P., et al. "Boosted decision trees as an alternative to artificial neural networks for particle identification." *Nuclear Instruments and Methods in Physics Research Section A: Accelerators, Spectrometers, Detectors and Associated Equipment* 543.2-3 (2005): 577-584.
- [8]. Ripley, Brian D., and N. L. Hjort. *Pattern recognition and neural networks*. Cambridge university press, 1996.
- [9]. Fukunaga, Keinosuke. "Introduction to statistical pattern recognition." (1990).
- [10]. Kuncheva, Ludmila I. *Combining pattern classifiers: methods and algorithms*. John Wiley & Sons, 2004.
- [11]. Bishop, Christopher M. *Neural networks for pattern recognition*. Oxford university press, 1995.
- [12]. Agatonovic-Kustrin, S., and R. Beresford. "Basic concepts of artificial neural network (ANN) modeling and its application in pharmaceutical research." *Journal of pharmaceutical and biomedical analysis* 22.5 (2000): 717-727.

- [13]. Jain, Anil K., Jianchang Mao, and K. M. Mohiuddin. "Artificial neural networks: A tutorial." *Computer* 3 (1996): 31-44.
- [14]. Haykin, Simon S. *Neural networks and learning machines/Simon Haykin*. New York: Prentice Hall, 2009.
- [15]. Karlik, Bekir, and A. Vehbi Olgac. "Performance analysis of various activation functions in generalized MLP architectures of neural networks." *International Journal of Artificial Intelligence and Expert Systems* 1.4 (2011): 111-122.
- [16]. Haykin, Simon. *Neural networks: a comprehensive foundation*. Prentice Hall PTR, 1994.
- [17]. Kasabov, Nikola K. *Foundations of neural networks, fuzzy systems, and knowledge engineering*. Marcel Alencar, 1996.
- [18]. Ruck, Dennis W., Steven K. Rogers, and Matthew Kabrisky. "Feature selection using a multilayer perceptron." *Journal of Neural Network Computing* 2.2 (1990): 40-48.
- [19]. Pandey, P. C., and S. V. Barai. "Multilayer perceptron in damage detection of bridge structures." *Computers & structures* 54.4 (1995): 597-608.
- [20]. Kůrková, Věra. "Kolmogorov's theorem and multilayer neural networks." *Neural networks* 5.3 (1992): 501-506.
- [21]. Park, Myoung Soo, and Jin Young Choi. "Theoretical analysis on feature extraction capability of class-augmented PCA." *Pattern recognition* 42.11 (2009): 2353-2362.
- [22]. Rosipal, Roman, et al. "Kernel PCA for feature extraction and de-noising in nonlinear regression." *Neural Computing & Applications* 10.3 (2001): 231-243.
- [23]. Mao, Jianchang, and Anil K. Jain. "Artificial neural networks for feature extraction and multivariate data projection." *IEEE transactions on neural networks* 6.2 (1995): 296-317.
- [24]. Viola, Paul, and Michael J. Jones. "Robust real-time face detection." *International journal of computer vision* 57.2 (2004): 137-154.
- [25]. Nguyen, Hai Thanh, Katrin Franke, and Slobodan Petrović. "Reliability in a feature-selection process for intrusion detection." *Reliable Knowledge Discovery*. Springer, Boston, MA, 2012. 203-218.
- [26]. Abdi, Hervé, and Lynne J. Williams. "Principal component analysis." *Wiley interdisciplinary reviews: computational statistics* 2.4 (2010): 433-459.
- [27]. Bro, Rasmus, and Age K. Smilde. "Principal component analysis." *Analytical Methods* 6.9 (2014): 2812-2831.
- [28]. Kantardzic, Mehmed. *Data mining: concepts, models, methods, and algorithms*. John Wiley & Sons, 2011.
- [29]. P. Werbos. *Beyond Regression*. Phd thesis, Harvard University, 1974.

- [30]. Rumelhart, David E., Geoffrey E. Hinton, and Ronald J. Williams. *Learning internal representations by error propagation*. No. ICS-8506. California Univ San Diego La Jolla Inst for Cognitive Science, 1985.
- [31]. McClelland, James L., David E. Rumelhart, and PDP Research Group. "Parallel distributed processing." *Explorations in the Microstructure of Cognition 2* (1986): 216-271.
- [32]. LeCun, Yann, et al. "A theoretical framework for back-propagation." *Proceedings of the 1988 connectionist models summer school*. Vol. 1. CMU, Pittsburgh, Pa: Morgan Kaufmann, 1988.
- [33]. Gardner, Matt W., and S. R. Dorling. "Artificial neural networks (the multilayer perceptron)—a review of applications in the atmospheric sciences." *Atmospheric environment* 32.14-15 (1998): 2627-2636.
- [34]. Zhao, Yi. *Combination of Wireless sensor network and artificial neuronal network: a new approach of modeling*. Diss. Université de Toulon, 2013.
- [35]. Denby, B. "Neural networks and cellular automata in experimental high energy physics." *Computer Physics Communications* 49.3 (1988): 429-448.
- [36]. Teodorescu, Liliana. "Artificial neural networks in high-energy physics." (2008).
- [37]. Peterson, Carsten. "Track finding with neural networks." *Nuclear Instruments and Methods in Physics Research Section A: Accelerators, Spectrometers, Detectors and Associated Equipment* 279.3 (1989): 537-545.
- [38]. Abreu, Paulo, et al. "Classification of the hadronic decays of the Z0 into b and c quark pairs using a neural network." *Physics Letters B* 295.3-4 (1992): 383-395.
- [39]. Denby, Bruce. "Neural networks in high energy physics: a ten year perspective." *Computer Physics Communications* 119.2-3 (1999): 219-231.
- [40]. Abachi, S., et al. "Direct measurement of the top quark mass." *Physical Review Letters* 79.7 (1997): 1197.
- [41]. Abbott, B., et al. "Search for scalar leptoquark pairs decaying to electrons and jets in $\bar{p}p$ collisions." *Physical Review Letters* 79.22 (1997): 4321.
- [42]. Lindsey, Clark S., et al. "Real time track finding in a drift chamber with a VLSI neural network." *Nuclear Instruments and Methods in Physics Research Section A: Accelerators, Spectrometers, Detectors and Associated Equipment* 317.1-2 (1992): 346-356.
- [43]. Köhne, J. K., et al. "Realization of a second level neural network trigger for the H1 experiment at HERA." *Nuclear Instruments and Methods in Physics Research Section A:*

- Accelerators, Spectrometers, Detectors and Associated Equipment* 389.1-2 (1997): 128-133.
- [44]. Won, Eunil. "A hardware implementation of artificial neural networks using field programmable gate arrays." *Nuclear Instruments and Methods in Physics Research Section A: Accelerators, Spectrometers, Detectors and Associated Equipment* 581.3 (2007): 816-820.
- [45]. <https://belle.kek.jp/>
- [46]. Won, Eunil, Hyuncheong Ha, and Yoshihito Iwasaki. "Upgrade of the level 1 global trigger system in the Belle experiment." *IEEE Transactions on Nuclear Science* 55.1 (2008): 122-125.
- [47]. Ferreira, Pedro, et al. "Artificial neural networks processor—a hardware implementation using a fpga." *International Conference on Field Programmable Logic and Applications*. Springer, Berlin, Heidelberg, 2004.
- [48]. Amin, Hesham, K. Memy Curtis, and Barrie R. Hayes-Gill. "Piecewise linear approximation applied to nonlinear function of a neural network." *IEE Proceedings-Circuits, Devices and Systems* 144.6 (1997): 313-317.
- [49]. Mitra, Subhrajit, and Paramita Chattopadhyay. "Challenges in implementation of ANN in embedded system." *2016 International Conference on Electrical, Electronics, and Optimization Techniques (ICEEOT)*. IEEE, 2016.
- [50]. Forssell, Mats. "Hardware Implementation of Artificial Neural Networks." (2014).

4 FPGA Implementation of ANN for Reconstructing Incident Angles

In order to tag and remove hits induced by charged particles coming from the beam background, our group in IPHC proposed to integrate Artificial Neural Networks (ANNs) into a CMOS Pixel Sensor (CPS). Background particles possess low momenta, leading to the generation of large incident angles and elongated cluster shapes. Incident angles can be used for identifying particles and reconstructing tracking. Due to the design of the prototype chip requires a lot of time and resources, ANNs were implemented in a Field Programmable Gate Array (FPGA) device to reconstruct incident angles for the feasibility study. An offline methodology was employed for gathering raw data and training weights, as shown in figure 4.1.

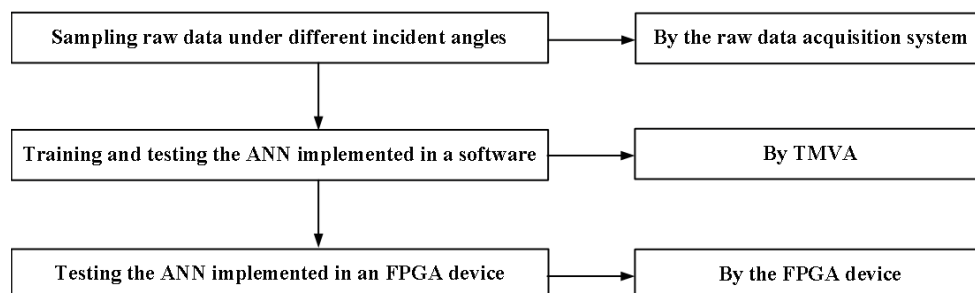


Figure 4.1: Main procedures of the offline methodology. The training and the test process in TMVA have been accomplished by my colleague Luis Alejandro PEREZ PEREZ.

- An independent raw data acquisition system was established to collect raw data of a CPS under different incident angles.
- The Toolkit for Multivariate Data Analysis (TMVA) [1] was used to train

and test the ANN structure. This part has been accomplished with my colleague *Luis alejandro PEREZ PEREZ*.

- A FPGA device was used to implement the ANN and all preprocessing modules. The ANN implementation was tested and analysed.

The feasibility study is described in the chapter. Firstly, the raw data acquisition system is illustrated; Next, the FPGA implementation of the ANN and preprocessing modules are described and explained in detail; Finally, test results of the ANN implementation are shown, incident angles reconstructed are compared with the results reconstructed by the ANN implemented in the TMVA and analysed.

4.1 Raw Data Acquisition System

The raw data acquisition system is used to collect raw data (training datasets and test datasets) and corresponding incident angles supplied to the training process and the test process. Cluster information is extracted from each frame of raw data.

1. In the training process. According to the supervised learning, features extracted from clusters and specified target results (corresponding incident angles) are fed into the ANN to train weights.
2. In the test process. Features are fed into the ANN to reconstruct an incident angle based on weights.

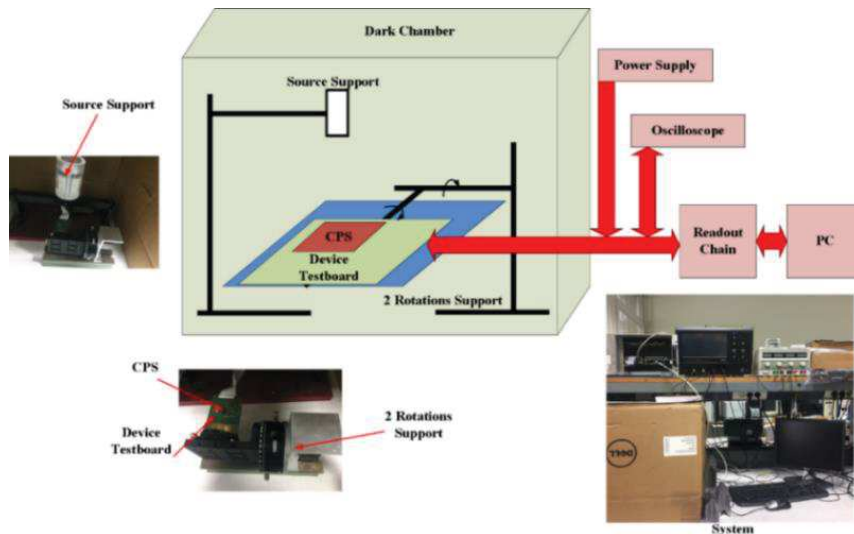


Figure 4.2: Schematic diagram of the raw data acquisition system.

The data acquisition system supports a CPS to expose under the radiation of a β^- source ^{90}Sr . Cluster information will be produced if charged particles hit on the CPS. The schematic diagram and main components of the system are shown in figure 4.2.

- A dark chamber (box) was used to supply the dark environment to prevent the light influence from the surrounding.
- A CMOS pixel sensor (MIMOSA 18) was bonded on the device test board (see section 4.1.1).
- A 2 rotations support was employed to tune angles between the CPS and the reference plane (see section 4.1.2).
- A readout chain was used to transmit data and signals. Raw analog data is read out from the CPS, converted to digital data and transferred to PC (see section 4.1.3).
- A source support was used to place the β^- source ^{90}Sr .

4.1.1 CMOS Pixel Sensor

MIMOSA18 is a CMOS pixel sensor fabricated in the AMS 0.35 μm OPTO process with a standard epitaxial layer thickness of 14 μm ($\sim 10 - 15 \Omega \cdot \text{cm}$). The total charge of a hit is related to the thickness of the epitaxial layer, about ~ 80 e-h pair/ μm can be generated by charged particles. The standard epitaxial layer results in the typical total charge of $O(1000e^-)$ [2].

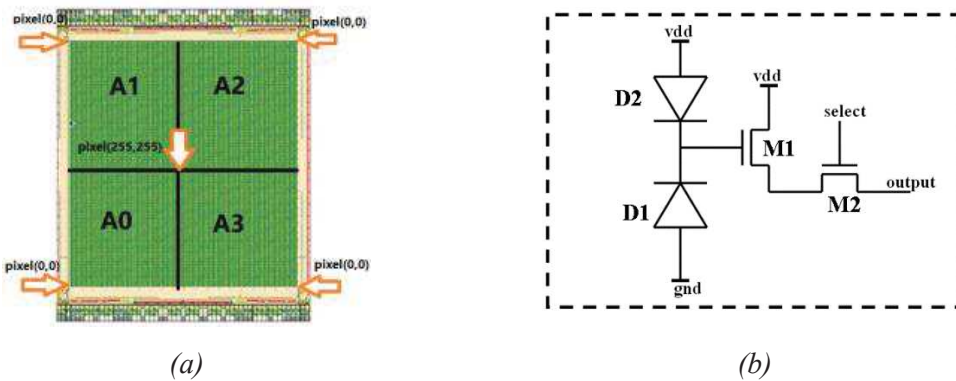


Figure 4.3: CMOS pixel sensor MIMOSA 18 (a) Layout of MIMOSA 18 (b) The pixel structure of the MIMOSA18 [3].

As shown in figure 4.3(a), a MIMOSA 18 sensor consists of 4 submatrices (A0~A3). Each submatrix contains 256×256 pixels with a pitch of 10 μm and provides

an active area of $5 \times 5 \text{ mm}^2$. One submatrix of the sensor is activated in the raw data acquisition system.

A pixel architecture used in MIMOSA 18 is illustrated in figure 4.3(b). It is composed of 2 transistors and 2 diodes. An N-well diode (D1) is used to collect the charges created in the epitaxial layer. The size of the collecting diode is $4.4 \times 3.4 \text{ }\mu\text{m}^2$. The other diode (D2) which is under forwarding bias is used to supply the voltage bias. One transistor (M1) of a source follower is connected to the charge collecting N-well diode, the other transistor (M2) is controlled by the signal “select” [3].

4.1.2 2 Rotations Support

A 2 rotations support was employed to place the MIMOSA 18. In the case that the source ^{90}Sr is fixed, incident angles of charged particles are tuned by adjusting two angles (α , β) between the CMOS pixel sensor and the reference plane.

In the section, the principle of the 2 rotations support is explained to show the correlation between the incident angle (θ) and angles (α , β). In addition, detailed settings of the 2 rotations support are given.

Principles

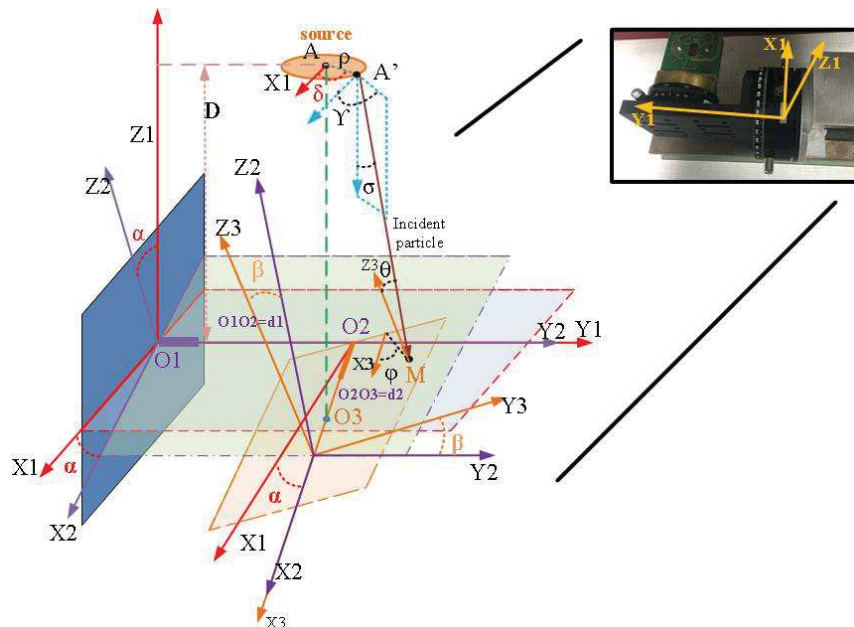


Figure 4.4: Schematic of the 2 rotations support.

The schematic of the 2 rotations support is shown in figure 4.4, where “source” means the position of the ^{90}Sr , point “A” indicates the centre of the source, point “A”

indicates the emitted location of a charged particle from the source.

Three coordinate systems in figure 4.4 are described as: “ $X1Y1Z1$ ” presents the reference coordinate system. Coordinate system “ $X2Y2Z2$ ” fixed at point “ O_1 ” is formed by rotating “ $X1Y1Z1$ ” α degrees around $Y1$ -axis. Coordinate system “ $X3Y3Z3$ ” fixed at point “ O_2 ” is formed by rotating “ $X2Y2Z2$ ” β degrees around $X2$ -axis.

Plane “ $X3Y3$ ” represents the location of the CMOS pixel sensor. Point “ M ” on plane “ $X3Y3$ ” means a hit point on the CMOS pixel sensor, vector $\overrightarrow{A'M}$ is the trajectory vector of the incident particle, “ θ ” is the incident angle of a charged particle, “ φ ” is the angle between the positive direction of $X3$ -axis and the projected vector of $\overrightarrow{A'M}$ on plane “ $X3Y3$ ”.

➤ Expression of an incident angle

Assuming a vector in coordinate system “ $X1Y1Z1$ ” can be present as $\overrightarrow{x_1} + \overrightarrow{y_1} + \overrightarrow{z_1}$. According to the relation of these coordinate system, the vector presentation in other coordinate systems can be converted as follows:

- Convert from “ $X1Y1Z1$ ” coordinate system to “ $X3Y3Z3$ ”:

$$\begin{pmatrix} \overrightarrow{x_3} \\ \overrightarrow{y_3} \\ \overrightarrow{z_3} \end{pmatrix} = \begin{pmatrix} \cos(\alpha) & 0 & -\sin(\alpha) \\ \sin(\alpha) \sin(\beta) & \cos(\beta) & \cos(\alpha) \sin(\beta) \\ \sin(\alpha) \cos(\beta) & -\sin(\beta) & \cos(\alpha) \cos(\beta) \end{pmatrix} \begin{pmatrix} \overrightarrow{x_1} \\ \overrightarrow{y_1} \\ \overrightarrow{z_1} \end{pmatrix}. \quad (4-1)$$

- Convert from “ $X3Y3Z3$ ” coordinate system to “ $X1Y1Z1$ ”:

$$\begin{pmatrix} \overrightarrow{x_1} \\ \overrightarrow{y_1} \\ \overrightarrow{z_1} \end{pmatrix} = \begin{pmatrix} \cos(\alpha) & \sin(\alpha) \sin(\beta) & \sin(\alpha) \cos(\beta) \\ 0 & \cos(\beta) & -\sin(\beta) \\ -\sin(\alpha) & \sin(\beta) \cos(\alpha) & \cos(\alpha) \cos(\beta) \end{pmatrix} \begin{pmatrix} \overrightarrow{x_3} \\ \overrightarrow{y_3} \\ \overrightarrow{z_3} \end{pmatrix}. \quad (4-2)$$

The incident angle “ θ ” and angle “ φ ” can be calculated as

$$\cos\theta = \frac{\|\overrightarrow{A'M_{z3}}\|}{\|\overrightarrow{A'M}\|}, \quad (4-3)$$

$$\cos\varphi = \frac{\|\overrightarrow{A'M_{x3}}\|}{\sqrt{\|\overrightarrow{A'M_{x3}}\| \times \|\overrightarrow{A'M_{x3}}\| + \|\overrightarrow{A'M_{y3}}\| \times \|\overrightarrow{A'M_{y3}}\|}}, \quad (4-4)$$

where

$\overrightarrow{A'M_{z3}}$ is the vector projected by vector $\overrightarrow{A'M}$ on plane “ $X3Y3$ ”.

$\overrightarrow{A'M_{x3}}$ is the vector projected by vector $\overrightarrow{A'M}$ on plane “ $Y3Z3$ ”.

$\overrightarrow{A'M_{y3}}$ is the vector projected by vector $\overrightarrow{A'M}$ on plane “X3Z3”.

➤ **Expression of $\overrightarrow{A'M}$ and $\overrightarrow{A'M_{z3}}$**

The unit vector of vector $\overrightarrow{A'M}$ in coordinate system “X1Y1Z1” is expressed as

$$\vec{\mu} = (\sin(\sigma) \cos(\gamma) \quad \sin(\sigma) \sin(\gamma) \quad -\cos(\sigma)) \begin{pmatrix} \vec{x}_1 \\ \vec{y}_1 \\ \vec{z}_1 \end{pmatrix} = (a \quad b \quad c) \begin{pmatrix} \vec{x}_1 \\ \vec{y}_1 \\ \vec{z}_1 \end{pmatrix}, \quad (4-5)$$

where

σ is the angle between $\overrightarrow{A'M}$ and the negative direction of Z1-axis.

γ is the angle between $\overrightarrow{A'M}$ and the positive direction of X1-axis.

$\overrightarrow{A'M}$ is presented as

$$\overrightarrow{A'M} = (at \quad bt \quad ct) \begin{pmatrix} \vec{x}_1 \\ \vec{y}_1 \\ \vec{z}_1 \end{pmatrix}, \quad (4-6)$$

where

t is the flight time of the charged particle from the emission point “A” to the hit point “M” on the CMOS pixel sensor.

The expression of $\overrightarrow{A'M}$ in the coordinate system “X3Y3Z3” is derived from the formula (4-1) and presented as

$$\overrightarrow{A'M} = (\vec{x}_3 \quad \vec{y}_3 \quad \vec{z}_3) \begin{pmatrix} at\cos(\alpha) - ct\sin(\alpha) \\ at\sin(\alpha)\sin(\beta) + bt\cos(\beta) + ct\cos(\alpha)\sin(\beta) \\ at\sin(\alpha)\cos(\beta) - bt\sin(\beta) + ct\cos(\alpha)\cos(\beta) \end{pmatrix}. \quad (4-7)$$

The projected vector of $\overrightarrow{A'M}$ on plane “X3Y3” is expressed as

$$\overrightarrow{A'M_{z3}} = (\vec{x}_3 \quad \vec{y}_3 \quad \vec{z}_3) \begin{pmatrix} 0 \\ 0 \\ at\sin(\alpha)\cos(\beta) - bt\sin(\beta) + ct\cos(\alpha)\cos(\beta) \end{pmatrix}. \quad (4-8)$$

➤ **Expression of fly time (t)**

Vector $\overrightarrow{MO_3}$ on plane “X3Y3”, and it is passed by the normal vector \vec{Z}_3 . The two vectors are perpendicular to each other. They are written as

$$\overline{MO}_3 \times \overline{Z}_3 = 0. \quad (4-9)$$

According to formula (4-1), \overline{z}_3 is written as

$$\overline{z}_3 = \begin{pmatrix} \sin(\alpha)\cos(\beta) & -\sin(\beta) & \cos(\alpha)\cos(\beta) \end{pmatrix} \begin{pmatrix} \overline{x}_1 \\ \overline{y}_1 \\ \overline{z}_1 \end{pmatrix}, \quad (4-10)$$

Vector \overline{MO}_3 is calculated as follows:

$$\overline{O}_1\overline{O}_3 = \overline{O}_1\overline{O}_2 + \overline{O}_2\overline{O}_3 = d_1\overline{y}_1 + d_2\overline{x}_2 = \begin{pmatrix} \overline{x}_1 & \overline{y}_1 & \overline{z}_1 \end{pmatrix} \begin{pmatrix} d_2\cos(\alpha) \\ d_1 \\ -d_2\sin(\alpha) \end{pmatrix}, \quad (4-11)$$

where

O_3 is the projected position of the central point “A” on plane “X3Y3”.

d_1 is the distance between point “ O_1 ” and point “ O_2 ”.

d_2 is the distance between point “ O_2 ” and “ O_3 ”.

$$\overline{O}_3\overline{A} = \begin{pmatrix} \overline{x}_1 & \overline{y}_1 & \overline{z}_1 \end{pmatrix} \begin{pmatrix} 0 \\ 0 \\ D + d_2\sin(\alpha) \end{pmatrix}, \quad (4-12)$$

$$\overline{O}_1\overline{A} = \overline{O}_1\overline{O}_2 + \overline{O}_2\overline{O}_3 + \overline{O}_3\overline{A} = \overline{O}_1\overline{O}_3 + \overline{O}_3\overline{A} = \begin{pmatrix} \overline{x}_1 & \overline{y}_1 & \overline{z}_1 \end{pmatrix} \begin{pmatrix} d_2\cos(\alpha) \\ d_1 \\ D \end{pmatrix}, \quad (4-13)$$

where

D is the distance of normal vector from point “A” to the plane “X1Y1”.

Position of “ O_3 ” projected by point “A” on plane “X3Y3” varies with the angle α and β . However, considering “ D ” is large enough, the variety of d_2 can make little difference in $\overline{O}_3\overline{A}$.

$$\overline{AA'} = \begin{pmatrix} \overline{x}_1 & \overline{y}_1 & \overline{z}_1 \end{pmatrix} \begin{pmatrix} \rho\cos(\delta) \\ \rho\sin(\delta) \\ 0 \end{pmatrix}, \quad (4-14)$$

$$\overline{O}_1\overline{A'} = \overline{O}_1\overline{A} + \overline{AA'} = \begin{pmatrix} \overline{x}_1 & \overline{y}_1 & \overline{z}_1 \end{pmatrix} \begin{pmatrix} d_2\cos(\alpha) + \rho\cos(\delta) \\ d_1 + \rho\sin(\delta) \\ D \end{pmatrix}, \quad (4-15)$$

where

δ is the angle between the vector $\overrightarrow{AA'}$ and the XI -axis.

ρ is the radius of the source.

$$\overrightarrow{O_1M} = \overrightarrow{O_1A'} + \overrightarrow{A'M} = (\overrightarrow{x_1} \ \overrightarrow{y_1} \ \overrightarrow{z_1}) \begin{pmatrix} d_2 \cos(\alpha) + \rho \cos(\delta) + at \\ d_1 + \rho \sin(\delta) + bt \\ D + ct \end{pmatrix}. \quad (4-16)$$

$$\overrightarrow{MO_3} = \overrightarrow{O_1O_3} - \overrightarrow{O_1M} = (\overrightarrow{x_1} \ \overrightarrow{y_1} \ \overrightarrow{z_1}) \begin{pmatrix} -(at + \rho \cos(\delta)) \\ -(bt + \rho \sin(\delta)) \\ -(d_2 \sin(\alpha) + D + ct) \end{pmatrix}. \quad (4-17)$$

where a , b and c in the formula is

$$\begin{cases} a = \sin(\delta) \cos(\gamma) \\ b = \sin(\delta) \sin(\gamma) \\ c = -\cos(\delta) \end{cases}. \quad (4-18)$$

The flight time t of particles is expressed as

$$t = -\frac{(d_2 \cos(\sigma) + \rho \cos(\delta)) \sin(\alpha) \cos(\beta) - \rho \sin(\beta) \sin(\delta) + D \cos(\alpha) \cos(\beta)}{\sin(\sigma) \cos(\gamma) \sin(\alpha) \cos(\beta) - \sin(\sigma) \sin(\gamma) \sin(\beta) - \cos(\sigma) \cos(\alpha) \cos(\beta)}. \quad (4-19)$$

Correlations between incident angle θ and angles α and β are shown in figure 4.5, which is the simulation result based on the formula (4-3). According to the result, the incident angle θ of raw data required can be fixed according to the angles (α , β).

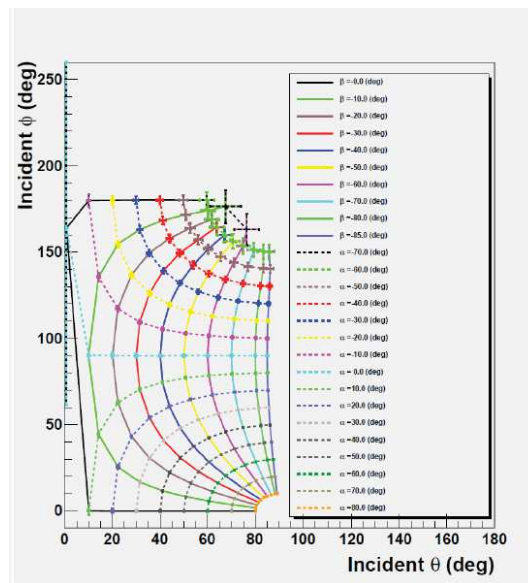


Figure 4.5: Simulation result of the correlation between incident angle ϕ , θ and α , β .

Setting

For training datasets and test datasets, 10 different incident angles were chosen to collect raw data. Detailed information of 10 incident angles (θ) is shown in Table 4-1, including angle φ presenting the angle between the main axis of a cluster and the X -axis.

Table 4-1: The setting of the angle θ , φ , and α , β .

θ (deg)	φ (deg)	α (deg)	β (deg)
0	0	0	0
15	136	-10	-10
30	90	0	-30
44	120	-20	-40
50	90	0	-50
56	127	-30	-50
62	113	-20	-60
64	124	-30	-60
71	111	-20	-70
73	127	-30	-70

In the training process, a large amount of raw data was acquired for each given incident angle θ . In the test process, 500 frames of raw data were acquired for each given incident angle θ .

4.1.3 Readout Chain

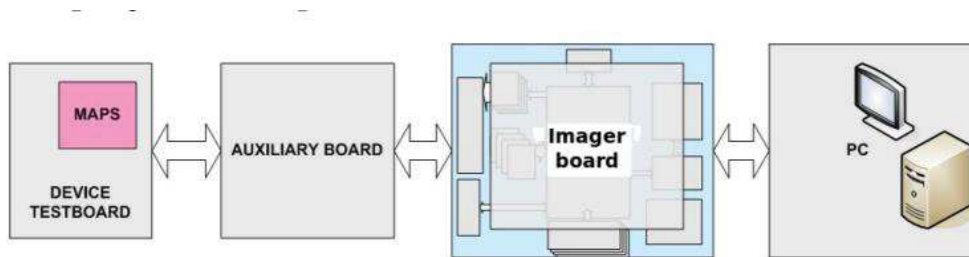


Figure 4.6: Schematic diagram of the MIMOSA 18 readout chain [4].

The readout chain of the raw data acquisition system is shown in figure 4.6, which presents the transmission of raw data and control signals between PC and the MIMOSA18.

The MIMOSA18 (“MAPS”) was mounted on a device test board which is used to

provide the power supply, mechanical support and transmit control signals, such as the clock, the reset, from an auxiliary board.

An auxiliary board is used to transmit analog data from the device test board to an imager board. In order to reduce the data attenuation due to long-distance transportation, the single-end signal from the device test board is amplified and converted to differential forms on the auxiliary board. Then, the differential signal is sent to the imager board via coaxial cables. In addition, the analog signal is sampled from the auxiliary board and monitored on an oscilloscope.

On the imager board, analog data from the auxiliary board is digitized to 12-bit and then sent to the disk of Windows PC through an ethernet link. The imager board is set up in and powered by a VME crate [4][5][6].

In the process of raw data acquisition, the device test board equipped with the MIMOSA 18 chip is placed in a dark chamber. The noise level is 2.2 ADC units, which is the average output of the chip in the dark chamber without irradiation of source ^{90}Sr .

4.2 Implementations in the FPGA

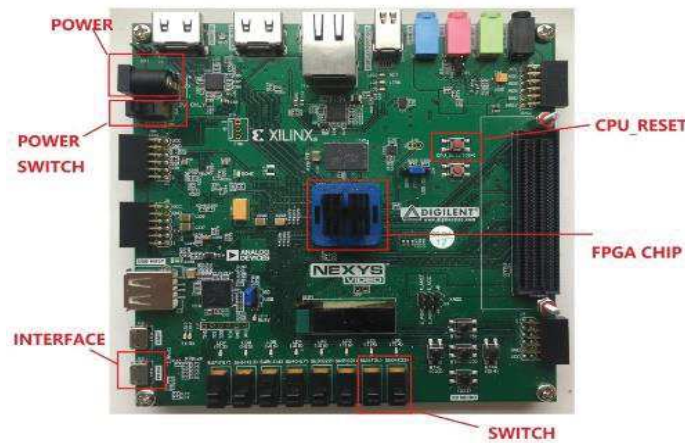


Figure 4.7: FPGA development board (Nexys Video Artix-7 FPGA) used in our study.

A NEXYS VIDEO FPGA development board was used to implement the ANN and preprocessing modules, as shown in figure 4.7. The development board has a Xilinx Artix-7 XC7A200T FPGA chip [7], high-speed USB interfaces, Bank RAMs, DSP modules and other resources.

An 8-bit micro USB interface (see "INTERFACE") was activated to read raw data into the FPGA board and write back reconstructed information to PC frame by frame. A

piece of reconstructed information contains cluster information (pixel charges and their relative positions in a cluster window) and the corresponding incident angle θ_{rec} reconstructed by the ANN.

Raw data read in the FPGA device is processed by Correlated Double Sampling (CDS) firstly of all, generating pixel charges. Two switches (see "SWITCH") on the board are called to supply alternative options on the data width of pixel charges. In my implementation, the two switches are set as "00" for data width is original 12-bit.

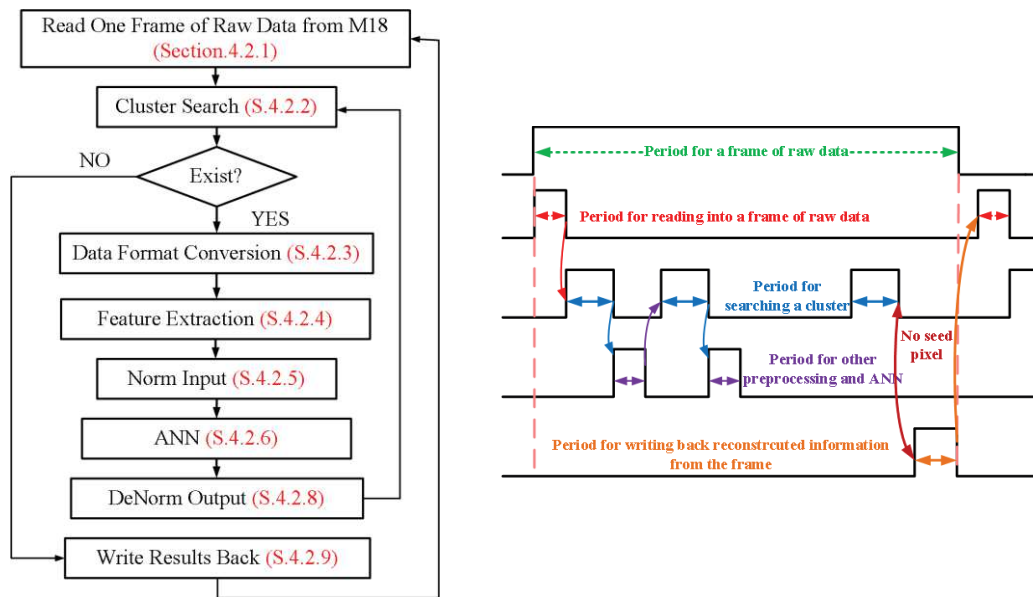


Figure 4.8: Main procedures and timing in the FPGA device.

Main procedures and timing of raw data processed in the FPGA device are shown in figure 4.8:

1. Reading one frame of raw data from PC:

256×256 pixels of 32-bit raw data are fed into the FPGA device and processed the CDS pixel by pixel. 256×256 pixels of 12-bit pixel charges are generated.

2. Cluster search:

Searching clusters in a frame of pixel charges. If there is a seed pixel in this frame, neighbour pixel charges of the seed pixel are collected and next step is started; otherwise, there is no cluster in the frame and the procedure jumps to the last step write reconstructed results of this frame back to PC.

3. Data format conversion:

Due to the exiting of IP core in the design suit of vivado, in order to simplify the implementation procedure in the FPGA, the integer is converted into floating point for the main calculation in the subsequent procedure.

4. Feature extraction:

Four features are extracted to present the cluster. The maximum and the minimum standard deviation of a cluster are calculated in the module named Main Component Analysis (MCA). Total charges of the cluster and the seed pixel charge are calculated within the process of cluster search.

5. Norm input:

The four features are normalized respectively and then fed into the ANN.

6. ANN:

An incident angle is reconstructed based on four normalized features of the cluster and weights fitted in the training process.

7. DeNorm output:

The output of the ANN is denormalized which is the reverse process of the normalization.

8. Write results back:

Reconstructed information (relative positions, pixel charges and the corresponding reconstructed angle θ_{rec}) in a frame is written back to PC.

4.2.1 Interface to Read in Raw Data

Each frame of raw data is stored in binary files by the fixed format, including some configuration contents (head part and end part). Raw data is extracted from the frame and transferred to the FPGA device through the 8-bit micro USB interface. The frame format of the file and the process of data reception in the FPGA are described in this section.

Format of Raw Data

A frame of raw data (256×256 pixels) is composed of three parts as shown in figure 4.9, including the head part, the body part and the end part.

- The head part: It is used to indicate the start of the frame. The head part is

composed of 112 bytes binary data. The number of the frame (“*Num fr*”) is recorded two times from 5th byte to 12th byte as shown in figure 4.9.

- The body part: It is the main content of the frame. The body part contains 256×256 pixels of 32-bit raw data. Only the body part is extracted and transported to the FPGA device. 32-bit raw data of each pixel are expressed in three parts, including two 12 bits data and an 8-bit extra data. Two 12 bits of raw data are two samples of one pixel, respectively, which are supplied to the CDS module.
- The end part: It is used to indicate the end of a frame. The end part is expressed in a fixed number (4 bytes). The first byte is $(EF)_{hex}$, the second byte is $(CD)_{hex}$, the third byte is $(AB)_{hex}$, the last byte is $(89)_{hex}$.

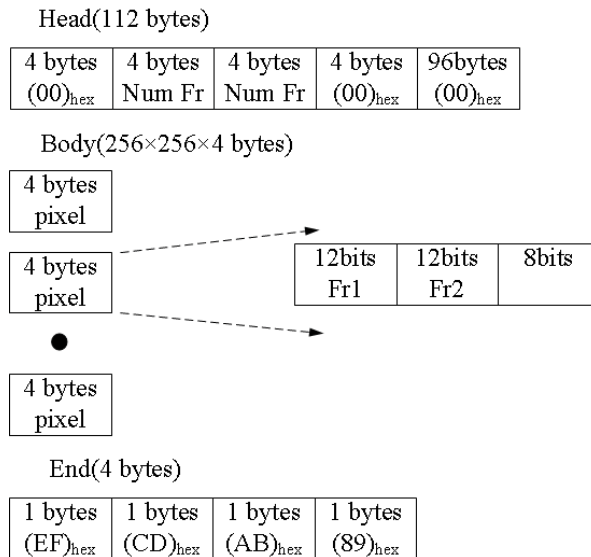


Figure 4.9: Frame format stored in a binary file (256×256 pixels).

The principle of body part extraction is described as follows:

1. The head part is searched and verified in a binary file;
2. Then next $256 \times 256 \times 4$ bytes raw data are read out and written into a memory of PC.
3. Reading out the following 4 bytes, if they are the same with the end part, it means that raw data in the memory is a complete body part and will be transferred to the FPGA; otherwise, the memory is reset and the next head part is searched in the binary file.

Through the frame format design (the head part and the end part), the integrity and

the accuracy of raw data transmitted to the FPGA are guaranteed.

Data Reception in the FPGA

The timing waveform to read raw data of one pixel is illustrated in figure 4.10. Relevant signals are described as follows:

- *Prog_oen*: It is an output signal of the FPGA chip and used to control the micro USB interface to receive data. Signal “*Prog_oen*” needs to be active (low-level voltage) one clock cycle before signal “*prog_rdn*” pulled down when raw data starts to be transferred.
- *Prog_rdn*: It is an output signal of the FPGA chip and used to control the micro USB interface to receive data. Raw data will be received only when signal “*Prog_oen*” and signal “*Prog_rdn*” are both enabled (low-level voltage).
- *Prog_clko*: A 60 MHz clock signal supplied by the micro USB interface chip. This 60 MHz clock is used as the system clock in our design.
- *Prog_d*: It is an 8-bit data bus to transport data between PC to the FPGA device.

In figure 4.10, raw data of the pixel shown is (ABCDEF00)_{hex}, the period for receiving is 6 clock cycles.

1st clock cycle: Reading in the first 8-bit raw data in a register.

2nd clock cycle: Reading in the second 8-bit raw data in a register.

3rd clock cycle: Reading in the third 8-bit raw data in a register.

4th clock cycle: CDS operation. The CMOS pixel sensor MIMOSA18 output integration signals and reset signals, respectively. The two signals are voltages of the same sampling node at different time. In the CDS module, which is achieved in the FPGA device, the offset signal of the pixel charge is removed by subtracting the reset signal from the integration signals. In the case of the negative number (close to number zero) occurring by the subtraction, extra modules are needed to convert and unify the format of the integer value. In order to reduce the complications of the implementation, the pixel charge is limited in positive number as expressed

$$\text{Pixel charge} = |\text{Fr1} - \text{Fr2}|. \quad (4 - 20)$$

The first three 8-bit raw data are two 12-bit pixel charges of Fr1 and Fr2. For the example of the pixel shown in figure 4.10, where Fr1 is (DAB)_{hex}, and Fr2 is (EFC)_{hex}.

The pixel charge equalling to $(151)_{\text{hex}}$ is stored in a memory of the FPGA chip.

5th clock cycle: The resolution of the pixel charge is adjusted. There is a 2-bit switch that can set the resolution of the pixel charge at 4-bit, 5-bit, 8-bits and 12-bit. In our application, the switch [1:0] is set “00” which means the resolution is 12-bit, it is equal to the original resolution of a pixel.

6th clock cycle: Reading in the last 8-bit raw data of the pixel.

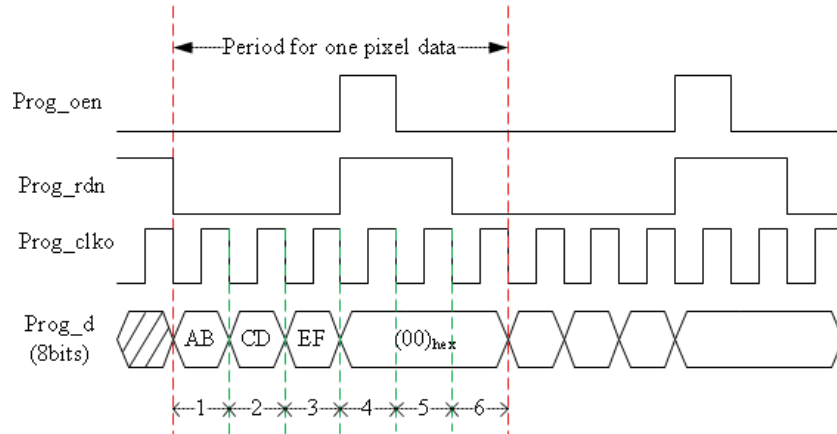


Figure 4.10: Timing waveform to read in raw data of an example from PC to the FPGA device.

4.2.2 Cluster Search

The cluster search process is used to find out clusters in the matrix of pixel charges (12-bit). The algorithm for cluster search is described and the simulation result is illustrated.

Algorithm for Cluster Search

Incident angles are reconstructed based on features of each cluster, including the cluster shape and the charge distribution. The performance of the algorithm for cluster search directly determines the reliability of reconstruction results. Parameters of the algorithm are presented as follows:

- *Noise threshold:* It is set to 5 ADC units. The output of the CMOS pixel without irradiation of source is about 2.2 ADC units due to the background and some electoral noises. The threshold is set above 2×2.2 ADC to filter the pixel charge affected by the background. A cluster is formed by some adjacent fired pixels. If the output amplitude of a pixel is higher than the noise threshold, it is defined as a fired pixel [8].
- *Seed pixel:* It has the largest charge in a cluster and exceeds the seed

threshold. It is used to fix the initial pixel of a cluster and locate the neighbour pixels. In the algorithm, a seed pixel is located at the central position of a 7×7 cluster window, its relative coordinate is (3, 3).

- *Seed threshold*: It is set to equal to 12 ADC units. Seed pixels have the largest charge in a cluster, the threshold is set above 5×2.2 ADC.
- *Cluster window*: It is a 7×7 pixels matrix which is used to limit the maximum area of a cluster.

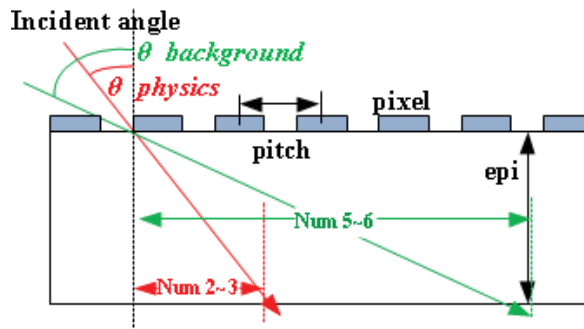


Figure 4.11: Incident angles of charged particles.

As shown in figure 4.11, the maximum incident angle that can be reconstructed depends on the size of the cluster window. It is calculated as

$$\tan\theta_{max} = \frac{num \times pitch}{epi}, \quad (4 - 21)$$

where

pitch is the pixel pitch of the CMOS pixel sensor (10 μm).

epi is the thickness of the epitaxial layer (14 μm).

num is the number of pixels in the horizontal or vertical direction of the cluster window. It equals 7 for the 7×7 cluster window.

According to formula (4-21), the largest value of the reconstructed angle θ_{rec} is 78.6 degrees. For a 5×5 cluster window, θ_{rec} is 74.35 degrees. According to the setting of the raw data acquisition system, the maximum incident angle is 73 degrees. Considering the deviation of incident angles that can be generated during the acquisition process, the 7×7 cluster window is chosen in the feasibility study. It means that a cluster shape which is larger than 7×7 cluster window will be recognized as two or more clusters.

Steps of the algorithm for cluster search in the FPGA device are shown in figure 4.12 and described as follows:

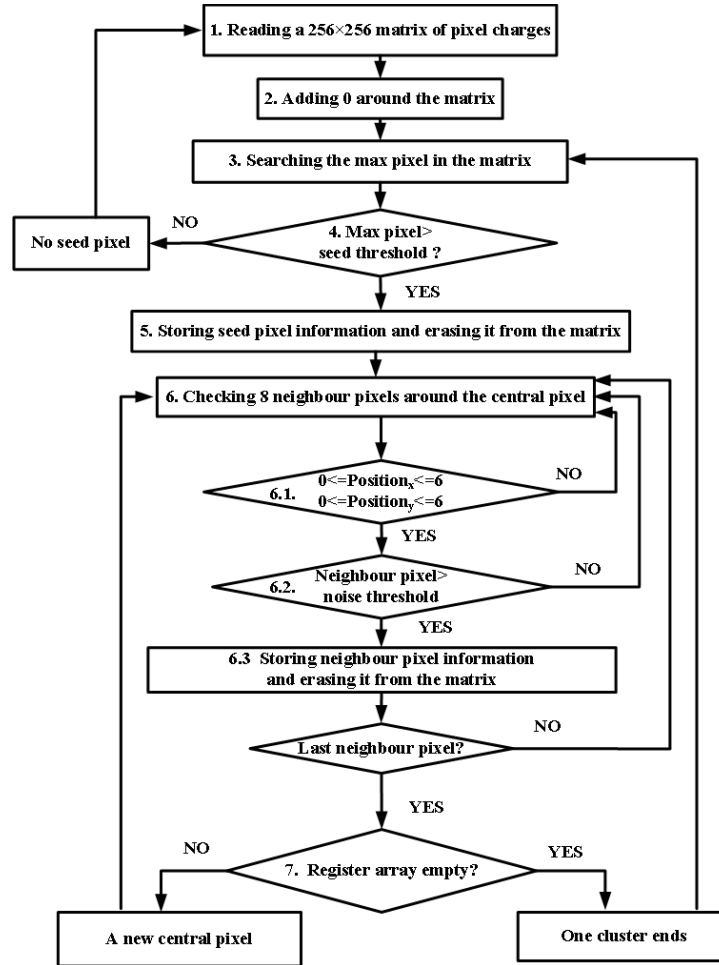


Figure 4.12: Algorithm for cluster search implemented in the FPGA device.

1. Reading a 256×256 matrix of pixel charges

Read in a 256×256 matrix of 12-bit pixel charges from the interface register and store in the memory of the FPGA.

2. Adding 0 around the matrix

To collect a complete cluster, neighbour pixels around a seed pixel need to be checked. Charges of neighbour pixels are extracted from the matrix according to their addresses. If the seed pixel is located at the boundary column, addresses of neighbour pixels on some directions are illegal. In order to avoid the illegal address, four exceptional options need to be set for the seed pixel located at boundary columns (left, right, top and bottom) to stop the algorithm on the direction.

Number 0 is added around the matrix to reduce the complexity of the algorithm on the boundary column. For instance, a seed pixel is located at the left boundary column.

If the algorithm checks its neighbour pixels on the left, their pixel charges are zero which means these neighbour pixels are not fired pixels. The algorithm will stop searching in this direction.

3. Searching the largest pixel charge in the matrix

A “max_value” register is implemented to store the charge and the position of the pixel that has the largest charge of the matrix. The matrix is scanned pixel by pixel and compared with the “max_value” register. The register value is updated if it is fewer than the charge of the scanned pixel. The largest one is recorded in the “max_value” register after scanning a frame of pixel charges.

4. Comparing the maximum pixel charge with the seed threshold

If the “max_value” register is larger than the seed threshold, the pixel stored in the register is recognized as a seed pixel. The algorithm jumps to the follow-up step.

Otherwise, it means that all pixel charges in the matrix are fewer than the seed threshold and there is no more seed pixel in the matrix. The process for cluster search in this matrix is accomplished, then rewinds to step 1 and waits for the next 256×256 matrix of the pixel charge.

5. Storing seed pixel information and erasing it from the matrix

The charge and relative position (3, 3) of the seed pixel are stored in two register arrays (a charge register array and a relative position array) respectively. The relative position is used to guarantee that the neighbour pixel is located within the 7×7 cluster window. The pixel position of seed pixel recorded in the “max_value” register is used to locate neighbour pixels in the matrix.

The seed pixel charge is erased from the matrix to prevent this seed pixel from being counted repeatedly.

6. Checking 8 neighbour pixels around the central pixel

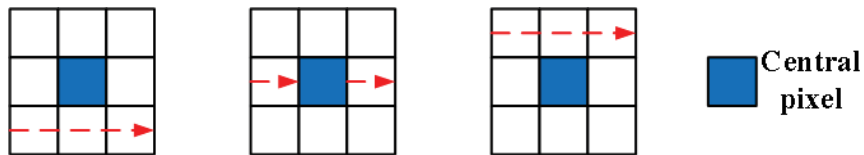


Figure 4.13: Steps of searching neighbour pixels around seed pixel.

8 pixels around the central pixel in a 3×3 window are checked pixel by pixel in a certain sequence (see figure 4.13). The seed pixel is the first central pixel for a cluster each time. A pointer is defined to mark the current central pixel in the charge register array. Charges and relative positions of all fired pixels in the 8 pixels are recorded in the

two register arrays respectively. Then the algorithm leaps to step 7.

Steps to check one neighbour pixel are described in step 6.1, 6.2, 6.3.

6.1 Checking the relative position of the neighbour pixel

If the relative position of the neighbour pixel both on X-axis and Y-axis are in the range of $[0, 6]$, it means that the neighbour pixel is located within the area of the 7×7 cluster window. The algorithm continues to the next step.

Otherwise, the neighbour pixel is out of the cluster window and it is not a part of the cluster. The algorithm returns to step 6 to calculate the relative position of the next neighbour pixel.

6.2 Checking the charge of the neighbour pixel

If the neighbour pixel charge is larger than the noise threshold, it is a fired pixel. The algorithm continues to the next step.

Otherwise, the neighbour pixel is not a fired pixel. The algorithm returns to step 6 to calculate the relative position of the next neighbour pixel.

6.3 Storing neighbour pixel information and erasing it from the matrix.

The pixel charge and the relative position of the neighbour pixel are stored in the two register arrays respectively. Then erase the charge of the neighbour pixel from the matrix to prevent it from being counted repeatedly.

7. Checking the charge register array

It is used to check whether the search process for the cluster is accomplished. After 8 neighbour pixels are scanned, the current central pixel pointer is moved to the next register of the charge register array. If the register is not empty, it means that there is a fired pixel in the 8 neighbour pixels which is chosen as the next central pixel. Then the algorithm returns to step 6 to check 8 neighbour pixels around the new central pixel.

If the register is empty, it means that all fired pixels adjacent to the seed pixel have been recorded and the algorithm stops for this seed pixel. Pixel charges and relative positions stored in the two register arrays are transferred to an output bank RAM. Then the two register arrays are reset. The algorithm leaps to step 3 to find the next seed pixel in the matrix.

Simulation Results

Besides the algorithm with the 7×7 cluster window described before, the algorithm without cluster window and the algorithm with the 5×5 cluster window are all achieved by C code. 500 frames of raw data for each given incident angle (Table 4.1) are taken to test these algorithms. Test results are shown in figure 4.14, where cluster counts are the number of clusters found for each given incident angle.

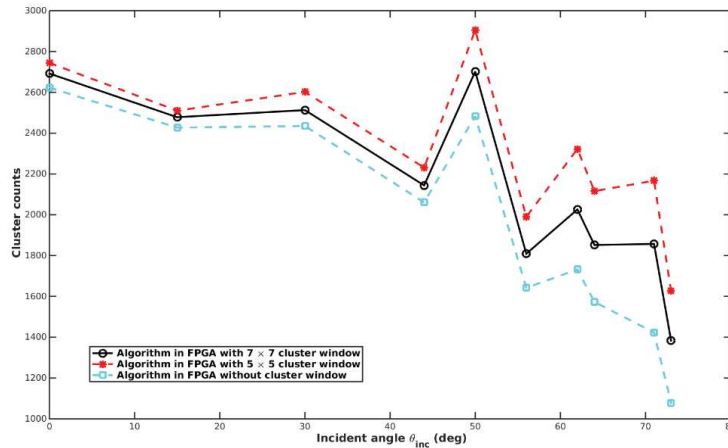


Figure 4.14: Cluster counts found by algorithms with different cluster windows.

The algorithm without cluster window means that there is no limitation for the size of a cluster. A cluster is identified only based on the connectivity between fired pixels and the seed pixel. For instance, a cluster shape that presents an elongated strip shape, even if more than 7 pixels, is defined as one cluster. Cluster counts found by the algorithm are the least among the three algorithms.

For the algorithm with a cluster window, the size limitation of a cluster is considered in addition to the connectivity of fired pixels and the seed pixel. The algorithm with the 5×5 cluster window limits the size of a cluster within 5×5 pixels. Cluster counts found by this algorithm are the most among the three algorithms.

As shown in the test result, cluster counts found by the algorithm with the 7×7 cluster window make a balance between the other two algorithms.

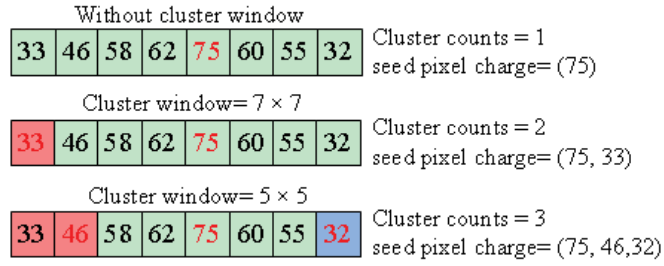


Figure 4.15: Cluster counts of an elongated cluster found by the three algorithms.

Comparing with clusters identified by the algorithm without cluster window, the limitation on the size of a cluster can divide one large cluster into two or more clusters. And with the decrease in the size of the cluster window, more clusters are recognized. For example, there is an elongated cluster which is composed of 8 pixels as shown in figure 4.15. 3 clusters are identified by the algorithm with the 5×5 cluster window, 2 clusters are recognized by the 7×7 cluster window, however, only one cluster is recorded by the algorithm without a cluster window.

As shown in figure 4.14, the number of elongated clusters increases as the incident angle increases, leading to the gap on cluster counts by the three algorithms expands. Taking account in the common cluster size and incident angles, the algorithm with the 7×7 cluster window is implemented in the FPGA device.

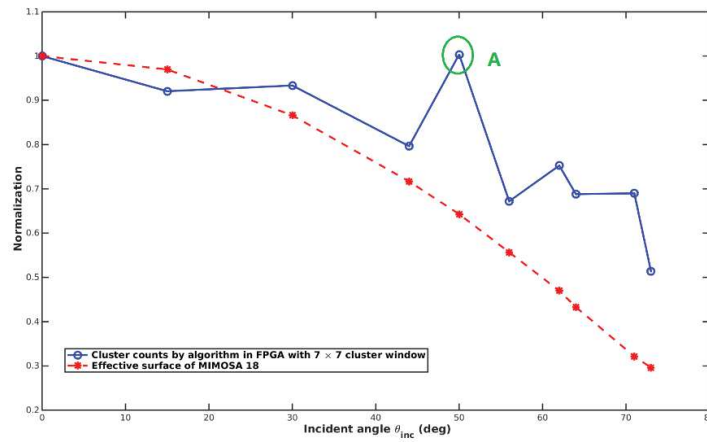


Figure 4.16: Simulation of cluster counts and effective surface.

In the raw data acquisition system, the incident angle is altered by tuned the angle between the MIMOSA 18 and the reference plane. The effective surface of the chip means the size of chip projected on the flat reference plane. The effective detection surface of MIMOSA 18 has some variation for different incident angles (see formula

4-22), resulting in a change in the number of incident particles that can be collected. The cluster count presents the same trend as the effective surface decreases. However, the sharp increase of cluster counts occurs in figure 4.16, as marked point A at incident angle $\theta_{inc} = 50$ degrees. Firstly, because of the reflection of the support below the chip, one particle may re-entrance the sensor again to generate extra clusters. Secondly, due to components around the chip, angle α make the larger influence on the cluster counts than angle β .

$$\frac{\text{effective surface}}{\text{chip surface}} = \cos(\alpha) \times \cos(\beta). \quad (4 - 22)$$

4.2.3 Data Format Conversion

In units following the cluster search module, operands are in the floating-point format, such as trigonometric function values supplied for feature extraction, and weights of the ANN. The 12-bit integer of the pixel charge has to be converted to the floating-point format to ensure a consistent data format. The floating-point conversion may lead some reduction on the data accuracy. However, firstly, convenience of implementation. conversion IP cores are existed which can be used for converting the integer into floating-point. Secondly, the feasibility study try to provide the proof of the principle that tag particles according to the incident angle based on the ANN has been established.

Single-precision floating-point format (binary 32) is one format of the IEEE 754 standard, which is a binary number format standard used in many hardware floating-point units [9][10].

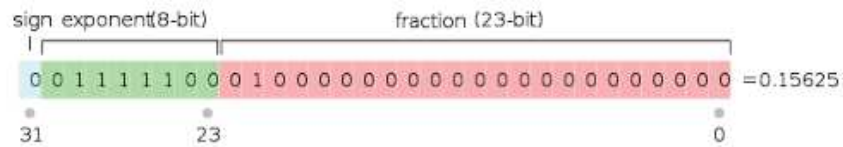


Figure 4.17: Format of Single-precision floating-point [10].

As shown in figure 4.17, the value expressed in the single-precision floating-point format can be calculated as

$$\text{value} = (-1)^s \times 2^{(e-127)} \times (1 + sp), \quad (4 - 23)$$

where

$$s(sign) = b_{31}. \quad (4 - 24)$$

$$e(exponent) = \sum_{i=23}^{30} (b_i \times 2^{i-23}). \quad (4 - 25)$$

$$sp(Significand\ precision) = \sum_{i=0}^{22} (b_i \times 2^{i-23}). \quad (4 - 26)$$

An Intellectual Property (IP) core is called in the FPGA device to convert the 12-bit integer pixel charge to IEEE 754 single-precision floating-point format.

4.2.4 Feature Extraction

Clusters have various expressions on the shape and the charge distribution, depending on different incident angles of charged particles. In order to achieve accurate incident angle reconstruction as much as possible, and taking into account the complexity of the artificial neural network structure, four features of a cluster are chosen and fed into the ANN structure, that is total charges of fired pixels (*TotChar*), the charge of the seed pixel (*SeedChar*), the maximum and the minimum standard deviation (*MaxStd* and *MinStd*) of the cluster.

Total Charges of Fired Pixels

TotChar is the sum of all fired pixel charges of a cluster which is related to the incident angle. It is determined by the distance of an incident particle in the epitaxial layer. The larger the incident angle of a charged particle, the longer it moves in the epitaxial layer and the more pixels are affected.

The average energy loss of charged particles when they pass through matter is described by the Bethe-Bloch formula (see chapter 1). Fluctuations of the energy loss in a thin absorber are described by Landau in 1944 [11]. The number of electron-hole pairs is related to the energy loss (Δ) in the matter. In figure 4.18, energy loss distributions for 500 MeV pions incident on thin a silicon detector is presented, where $f(x, \Delta)$ represents the distribution probability of the energy loss (Δ) when an incident particle traverses a layer of matter with thickness x . As fluctuations of the energy loss in a thin layer are large, the incident angle is not absolutely proportional to the total charge of a cluster. Incident angles cannot be reconstructed only based on the total charge.

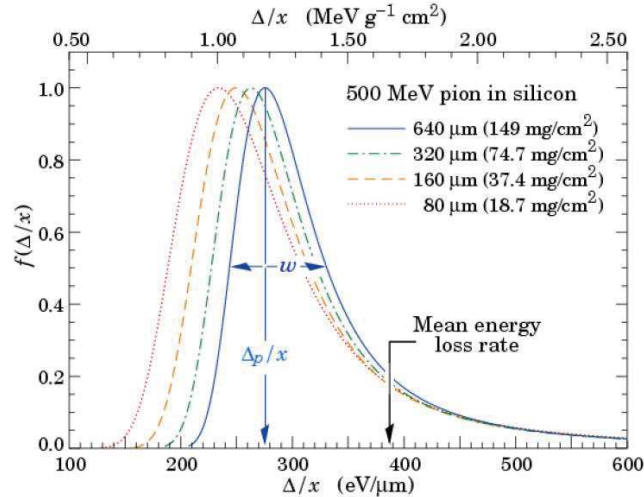


Figure 4.18: Stopping power for positive muons in copper Straggling functions in silicon for 500MeV pions, normalized to unity at the most probable value $\Delta p/x$ [12].

The Charge of the Seed Pixel

SeedChar is the pixel charge of the seed pixel of a cluster. It represents the largest number of electrons attracted in the epitaxial layer by a collection diode. The feature is related to the incident angle.

Maximum Standard Deviation (Minimum Standard Deviation)

As shown in figure 4.19, the particle hit on the CPS with an incident angle θ and generate a cluster, the angle between the main axis of the cluster and the X-axis is angle ϕ . *MaxStd* is the standard deviation along the main axis of the cluster, and *MinStd* is calculated along the vertical direction of the main axis. These two features are affected by the incident angle and reflect the shape and charge distribution of a cluster. An individual unit named Main Component Analysis (MCA) is designed to calculate *MaxStd* and *MinStd*.

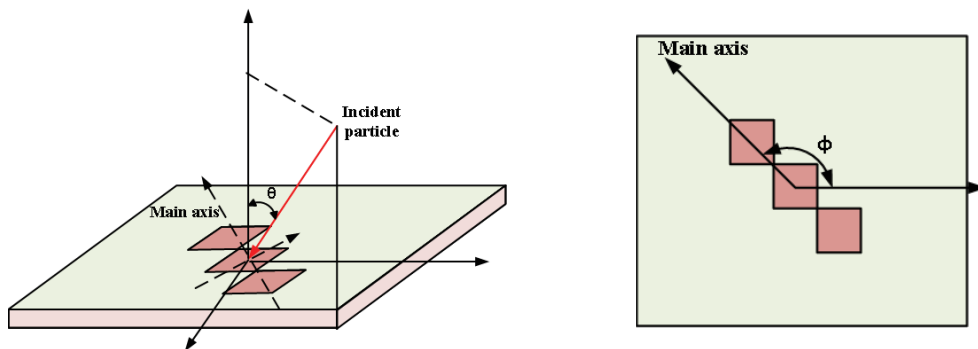


Figure 4.19: The main axis of a cluster.

- The variance of a cluster along X-axis and Y-axis

For a random variable K which is discrete with probability mass function $k_1 \rightarrow p_1, k_2 \rightarrow p_2, \dots, k_i \rightarrow p_i$. p_i is the probability of k_i . The variance of the random variable K can be calculated as

$$\text{Var}(K) = \sum_{i=1}^n p_i (k_i - \mu)^2 = \left(\sum_{i=1}^n p_i k_i^2 \right) - \mu^2, \quad \left(\sum_{i=1}^n p_i = 1 \right), \quad (4-27)$$

where

μ is the expected value of the random variable k , it is presented as

$$\mu = \sum_{i=1}^n p_i k_i. \quad (4-28)$$

In a cluster, positions of fired pixels are discrete with probability mass function $x_1 \rightarrow \frac{Q_1}{Q_t}, x_2 \rightarrow \frac{Q_2}{Q_t}, \dots, x_i \rightarrow \frac{Q_i}{Q_t}$. Q_i is the pixel charge of fired pixel i , Q_t is the total pixel charge of all fired pixels in the cluster. The variance of the cluster along X -axis can be calculated as

$$\text{Var}(X) = \langle X^2 \rangle - \langle X \rangle^2 = \sum_{i=1}^n \left(x_i^2 \times \frac{Q_i}{Q_t} \right) - \left(\sum_{i=1}^n x_i \times \frac{Q_i}{Q_t} \right)^2, \quad \sum_{i=0}^n \frac{Q_i}{Q_t} = 1, \quad (4-29)$$

where

$$\langle X^2 \rangle = \sum_{i=1}^n x_i^2 \times Q_i / Q_t. \quad (4-30)$$

$$\langle X \rangle = \mu = \sum_{i=1}^n x_i \times Q_i / Q_t. \quad (4-31)$$

The variance of the cluster along Y -axis is expressed as

$$\text{Var}(Y) = \langle Y^2 \rangle - \langle Y \rangle^2 = \sum_{i=1}^n \left(y_i^2 \times \frac{Q_i}{Q_t} \right) - \left(\sum_{i=1}^n y_i \times \frac{Q_i}{Q_t} \right)^2, \quad \sum_{i=0}^n \frac{Q_i}{Q_t} = 1. \quad (4-32)$$

where

n is the number of fired pixels in a cluster.

x_i is the distance along X -axis between the position of the fired pixel i the original

point.

y_i is the distance along Y -axis between the position of the fired pixel i the original point.

x_i and y_i are calculated as

$$\begin{cases} x_i = (x_{position} + 0.5) \times pitch_x \\ y_i = (y_{position} + 0.5) \times pitch_y \end{cases}, \quad (4 - 33)$$

where

$x_{position}$ is the relative position of a pixel in the 7×7 cluster window along X -axis.

$y_{position}$ is the relative position of a pixel in the 7×7 cluster window along Y -axis.

0.5 is the half-pixel between the original point and the centre of the first pixel.

$pitch_x$ is the distance between two neighbour pixels along the X -axis, it is $10 \mu\text{m}$ for CMOS pixel sensor MIMOSA 18.

$pitch_y$ is the distance between two neighbour pixels along the Y -axis, it is $10 \mu\text{m}$ for CMOS pixel sensor MIMOSA 18.

As shown in figure 4.20, x_i and y_i of a point “ M ” can be calculated in the following way. The relative position of point “ M ” in the cluster window $(x_{position}, y_{position})$ is $(3,1)$. The distance (x_i) along X -axis between the position of the pixel to the original point is $35 \mu\text{m}$, y_i is $15 \mu\text{m}$ along Y -axis.

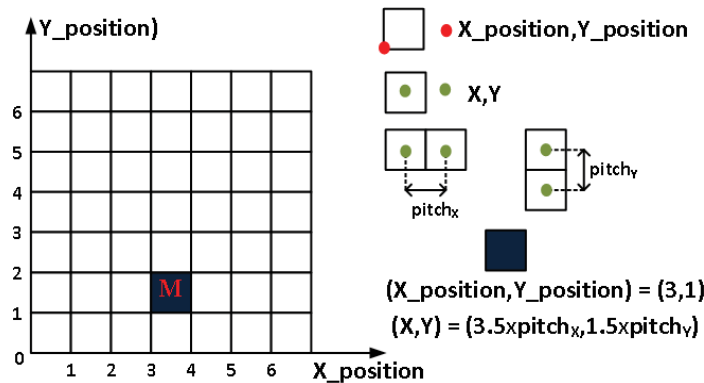


Figure 4.20: Position of a fired pixel in a cluster.

➤ Maximum and minimum standard deviation of a cluster

As shown in figure 4.21, the vector \overrightarrow{OM} in reference coordinate system can be obtained as

$$\overline{OM} = x \times \vec{x} + y \times \vec{y}, \quad (4-34)$$

where x and y are positions of point “M” in the reference coordinate system respectively.

The vector \overline{OM} can be presented as

$$\overline{OM} = x' \times \vec{x}' + y' \times \vec{y}', \quad (4-35)$$

where the \vec{x}' and \vec{y}' are axes of a new coordinate system which is formed by rotating α degrees from the reference coordinate system. x' and y' are positions of point “M” point along X' -axis and Y' -axis in the new coordinate system, respectively.

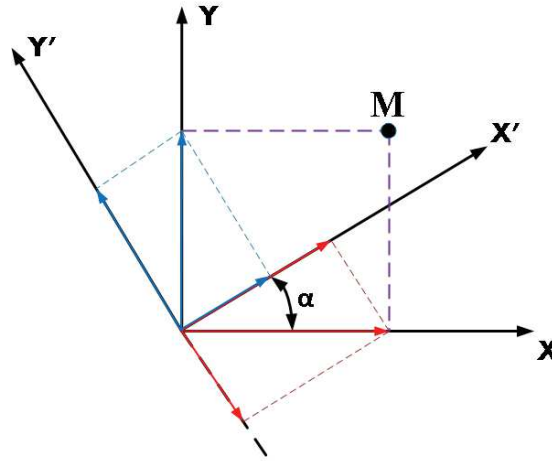


Figure 4.21: Correlation between two coordinate systems.

The position of point M in the new coordinate system can be presented as

$$\begin{cases} x' = x \times \cos(\alpha) + y \times \sin(\alpha) \\ y' = -x \times \sin(\alpha) + y \times \cos(\alpha) \end{cases} \quad (4-36)$$

The variance of the cluster along the X' -axis and Y' -axis can be presented as

$$\text{Var}(X') = \langle X'^2 \rangle - \langle X' \rangle^2, \quad (4-37)$$

$$\text{Var}(Y') = \langle Y'^2 \rangle - \langle Y' \rangle^2, \quad (4-38)$$

where

$$\langle X' \rangle = \frac{\sum_{i=1}^n (x'_i \times Q_i)}{Q_t} = \cos(\alpha) \times \langle X \rangle + \sin(\alpha) \times \langle Y \rangle. \quad (4-39)$$

$$\langle X'^2 \rangle = \frac{\sum_{i=1}^n (x_i'^2 \times Q_i)}{Q_t} = \cos^2(\alpha) \langle X^2 \rangle + \sin^2(\alpha) \langle Y^2 \rangle + \sin(2\alpha) \langle XY \rangle. \quad (4-40)$$

$$\langle Y' \rangle = \frac{\sum_{i=1}^n (y'_i \times Q_i)}{Q_t} = -\sin(\alpha) \times \langle X \rangle + \cos(\alpha) \times \langle Y \rangle . \quad (4 - 41)$$

$$\langle Y'^2 \rangle = \frac{\sum_{i=1}^n (y_i'^2 \times Q_i)}{Q_t} = \sin^2(\alpha) \langle X^2 \rangle + \cos^2(\alpha) \langle Y^2 \rangle - \sin(2\alpha) \langle XY \rangle . \quad (4 - 42)$$

Variations of the cluster along X' -axis and Y' -axis are functions about angle α , which can be described as

$$\begin{aligned} \text{Var}(X') &= \langle X'^2 \rangle - \langle X' \rangle^2 = f_{x'}(\alpha) \\ &= 2 \cos(\alpha) \sin(\alpha) (\langle XY \rangle - \langle X \rangle \langle Y \rangle) + \cos^2(\alpha) \times \text{Var}(X) + \sin^2(\alpha) \times \text{Var}(Y) , \end{aligned} \quad (4 - 43)$$

$$\begin{aligned} \text{Var}(Y') &= \langle Y'^2 \rangle - \langle Y' \rangle^2 = f_{y'}(\alpha) \\ &= 2 \cos(\alpha) \sin(\alpha) (\langle X \rangle \langle Y \rangle - \langle XY \rangle) + \sin^2(\alpha) \times \text{Var}(X) + \cos^2(\alpha) \times \text{Var}(Y) . \end{aligned} \quad (4 - 44)$$

β is the angle that generates the maximum variance and indicates the main axis of the cluster. β is presented as

$$f_{x'}(\beta) = \max(f_{x'}(\alpha)) . \quad (4 - 45)$$

Consider the resource in the hardware, it is challenging to calculate the exact angle β and main axis of the cluster. The lookup table method is a competitive candidate for finding the maximum or minimum value, especially for the complex calculation.

For the MCA achieved by C code in the training process, angle β can be calculated by the inverse trigonometric function. In our design implemented in the FPGA device, the value of trigonometric functions is stored in a lookup table, the maximum variance is found by sweeping angles α ([0,180 degrees]) in a step of 10 degrees. The lookup table with a step of 10 degrees reduces the accuracy of features and make a little influence on the reconstruction result.

MaxStd and *MinStd* are generated as

$$\text{MaxStd} = \sqrt{f_{x'}(\beta)} . \quad (4 - 46)$$

$$\text{MinStd} = \sqrt{f_{y'}(\beta)} . \quad (4 - 47)$$

4.2.5 Normalized Features

Data normalization is a fundamental preprocessing step for data mining and machine learning [13]. It is used to remove biases among dimensions of the data vectors, make every feature have the same weight level, and avoid large difference among feature values. In addition, the range of the data needs to match the activation function used in the ANN. The output range of the activation function is $[-1, 1]$. The function for feature values normalization is expressed as

$$\min(x_i) \leq x_i \leq \max(x_i) , \tag{4 - 48}$$

$$-1 \leq \frac{x_i - \min(x_i)}{\max(x_i) - \min(x_i)} \times 2 - 1 \leq 1, \tag{4 - 49}$$

where

x_i is the input feature i ,

$\min(x_i)$ is the minimum value of the input feature supplied by the training procedure.

$\max(x_i)$ is the maximum value of the input feature supplied by the training procedure.

4.2.6 ANN Implementation

A typical one hidden layer Multi-Layer Perceptron (MLP) is implemented in the FPGA device to reconstruct incident angles.

MLP Structure

The MLP structure contains three layers (input layer, hidden layer and output layer), as shown in figure 4.22.

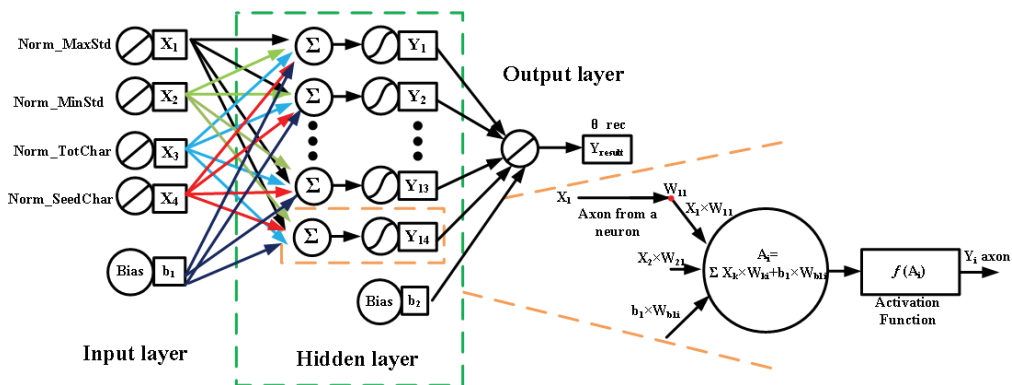


Figure 4.22: Structure of the artificial neural network.

Input layer contains four input neurons and one bias neuron. Input neurons are used to take four normalization features (*Norm_SeedChar*, *Norm_TotChar*, *Norm_MaxStd* and *Norm_MinStd*) extracted from each cluster into the network. The value of the bias neuron in the input layer is 1, which is used to shift the activation function.

In the hidden layer, there are 14 hidden neurons and one bias neuron. The number of hidden neurons is determined by the training procedure in the TMVA. It is an optimization result that takes into account resources and reconstruction efficiency. The bias value in the hidden layer is 1. As shown in figure 4.22, there are two steps to calculate the output of a hidden neuron:

1st step: Calculating values of summing junctions.

Input neurons including the bias neuron, are multiplied with corresponding weights, then add all the results together. The process is written as

$$A_i = \sum_1^{k=4} x_k \times w_{ki} + b_1 \times w_{b1i}, \quad (4 - 50)$$

where

- A_i is the result of the summing junction of hidden neuron i .
- x_k is the feature of input neuron k .
- w_{ki} is the weight between input neuron k and hidden neuron i .
- b_1 is the bias neuron in the input layer, it is set as 1.
- w_{b1i} is the weight between the bias neuron in the input layer and hidden neuron i .

2nd step: Calculating outputs of hidden neurons.

Results of summing junctions are processed by an activation function. The procedure and the activation function (hyperbolic tangent function) are written as

$$y_i = f(A_i), \quad (4 - 51)$$

$$f(x) = \tanh(x) = \frac{e^x - e^{-x}}{e^x + e^{-x}}, \quad (4 - 52)$$

where

- y_i is the value of hidden neuron i .
- $f(x)$ is the activation function. The output range of the hyperbolic tangent function is $[-1,1]$ [14].

The output layer composed of one output neuron gives the reconstructed result. Values of all hidden neurons, including the bias neuron in the hidden layer, are multiplied with the corresponding weights; and then added together. In our design, there is no activation function for the output neuron. The process is expressed as

$$y_{result} = \sum_{i=1}^{i=14} y_i \times w_i + b_2 \times w_{b2}, \quad (4 - 53)$$

where

y_{result} is the output of the output neuron.

y_i is the output of hidden neuron i .

w_i is the weight between hidden neuron i and the output neuron.

b_2 is the bias neuron in the hidden layer. It is set as 1.

w_{b2} is the weight between the bias neuron in the hidden layer and the output neuron.

The MLP structure contains a total of 21 neurons and 85 weights. All weights of the network are supplied by the training procedure performed by the TMVA.

Circuit implementation

The circuit implementation of the MLP structure is shown in figure 4.23. IP cores and hardware resources in the FPGA device are used. Description of main modules and signals are as follows:

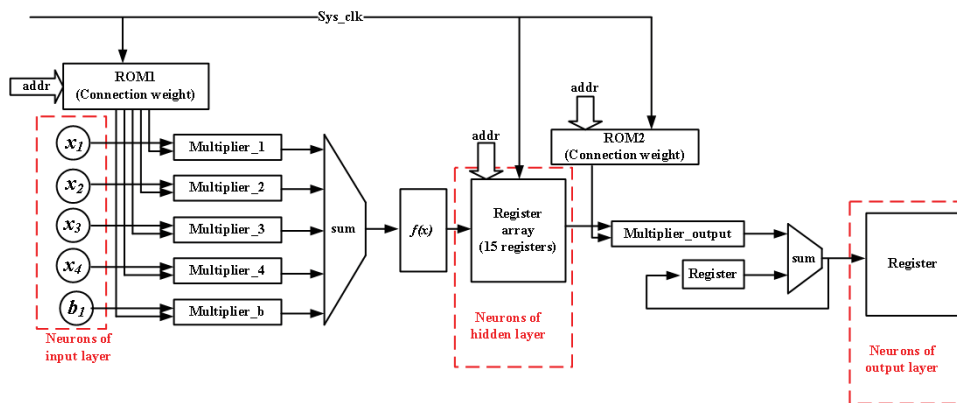


Figure 4.23: Digital circuit of the artificial neural network.

- Sys_clk : It is the 60MHz system clock supplied by the Micro-USB interface chip.
- $ROM1$: It is a memory module. $ROM1$ is used to store 14×5 weights

between input neurons and hidden neurons. Weights are output from the *ROM1* according to the address supplied by an address signal. Weights between 5 input neurons and 1 hidden neuron are output each time.

- *Multiplier array*: It is composed of 5 floating-point multiplier IP cores. Input neurons are multiplied corresponding weights in this module. It is controlled by the enabled signal and the system clock.
- *Sum_1*: It is an adder. The *sum_1* module is used to add 5 results of the multiplier array together. The result of one summing junction is calculated each time in the module.
- *f(x)*: It is the activation function module which is implemented by some complex mathematic IP cores, including exponent units, sum units and subtractor units.
- *Register array*: It is composed of 15 registers. The register array is used to store the values of neurons in the hidden layer, including 14 hidden neurons and the bias neuron.
- *ROM2*: It is a memory module. ROM2 is used to store 15 weights between hidden neurons and the output neuron. One weight is output from the ROM2 each time according to an address signal.
- *Multiplier_output*: It is a floating-point multiplier IP core. *Multiplier_output* is used to multiply the output of a hidden neuron by its weight between it and the output neuron.
- *Sum_2*: It is an adder. *Sum_2* is used to add 15 outputs of the *multiplier_output* unit together.

4.2.7 DeNormalized Module

The output result from the network needs to be translated into an incident angle. DeNormalized module is used to accomplish the inverse process of the normalization step. It is expressed as

$$-1 \leq normY_{result} \leq 1 \quad (4 - 54)$$

$$Y_{result} = \frac{normY_{result} + 1}{2} (Y_{resultmax} - Y_{reusttmin}) + Y_{resultmin} \quad (4 - 55)$$

where

$norm Y_{result}$ is the value of the output neuron.

Y_{result} is the degrees of the incident angle after translation.

$Y_{resultmax}$ is the maximum degree of the incident angle (73 degrees).

$Y_{resultmin}$ is the minimum degrees of the incident angle (0 degrees).

4.2.8 Interface to Output

Reconstructed information, containing cluster information (relative position and pixel charge) and the reconstructed incident angle, is transported from the FPGA device through the 8-bit micro USB interface to PC. The format of reconstructed information and the transmission timing sequence are described, respectively.

Format of reconstructed information

The software developed on Windows receives and extracts the reconstructed data according to the format. An example of the reconstructed information format is shown in figure 4.24. It is composed of 4 parts.

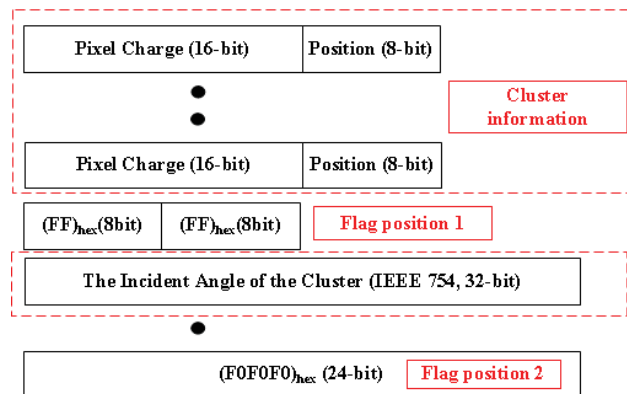


Figure 4.24: Reconstructed information format of a cluster.

- *Cluster information:* It shows parameters of fired pixels that constitute the cluster. Each fired pixel is expressed in 24-bit binary data, including the pixel charge (16-bit) and the relative position (8-bit).
- *Flag position 1:* The number of fired pixels in each cluster is uncertain, a flag is set to indicate the end of cluster information. *Flag position 1* is composed of 16 bits of data, expressing as (FFFF)_{hex}.
- *The incident angle of a cluster:* It is the incident angle reconstruct by the ANN. It is expressed in the format of single-precision floating-point and composed of 32-bit data.

- *Flag position 2*: It is used to indicate the end of a piece of reconstructed information. It is composed of 24-bit data, expressing as (F0F0F0)_{hex}.

Transmission timing sequence

In the FPGA device, a 24-bit bank memory is used to store reconstructed information of one frame. The transmission timing sequence of one memory cell from the FPGA to PC is shown in figure 4.25. Signals are illustrated as follows:

- *Prog_wrn*: It is an output signal of the FPGA chip and used to control the process of reconstructed information transmission from the micro USB interface to PC, which will begin when the signal is low-level voltage.
- *MEM_en*: It is an output signal of the FPGA chip and used to control the output memory. Address of the memory cell will be locked and the data in a memory cell will be prepared when *MEM_en* is low-level voltage.
- *Prog_clk*: It is the 60 MHz clock and supplied by the micro USB interface chip.
- *Prog_d*: It is an 8-bit data signal to transport data from the FPGA device to PC.

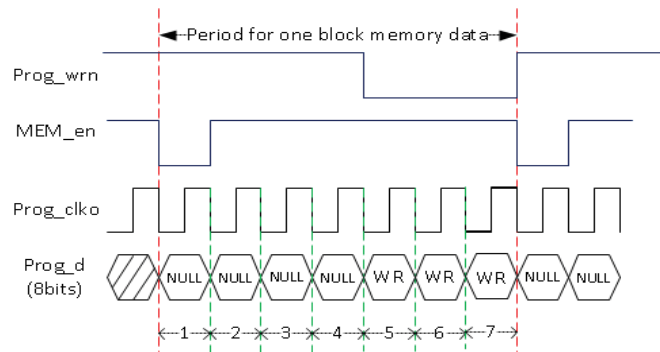


Figure 4.25: Timing of transporting the output result of one memory cell.

As shown in figure 4.25, 7 clock cycles are needed to transfer data of one output memory cell (3-byte).

1st clock cycle: Signal *MEM_en* is enabled to locate the address of the output memory cell, indicating the start of reading out one memory cell result.

2nd - 4th clock cycle: Three clock cycles are used to prepare the data of the output memory cell.

5th clock cycle: The signal *prog_wrn* is enabled and the signal *prog_d* starts to output the first byte data. The second byte and the third byte data is output continually

in the 6th and 7th clock cycle.

4.3 Test results

Reconstructed results are stored in PC as binary files. Cluster information and reconstructed incident angles are extracted and converted as the text file by the software designed based on Windows PC. Figure 4.26 shows reconstructed results of a frame of raw data which was taken under the incident angle of 15 degrees.

The content of the reconstructed result is shown in figure 4.26 (a). The blue part is cluster information. The charge (“charge”) and the relative position (“position”) of a fired pixel are presented in each line. “IEEE 754 result” is the original expression of the reconstructed angle in the format of single-precision floating-point. “Float result” is the degree of the incident angle converted from the “IEEE 754 result” by the software.

The reconstructed incident angles of the two clusters are 43.75 degrees and 36.41 degrees, respectively. These two clusters shapes and reconstructed results have been validated by results reconstructed by the ANN implemented in the TMVA.

```

Frame number is : 4500
#####
Charge is : 257 (XY) position is : 0X33
Charge is : 13 (XY) position is : 0X22
Charge is : 21 (XY) position is : 0X32
Charge is : 34 (XY) position is : 0X23
Charge is : 10 (XY) position is : 0X43
Charge is : 13 (XY) position is : 0X24
Charge is : 14 (XY) position is : 0X34
Charge is : 7 (XY) position is : 0X15
Hit number is : 1
IEEE 754 result is : 0X422EFB07
Float result is : 43.745144
This cluster finish
Charge is : 30 (XY) position is : 0X33
Charge is : 18 (XY) position is : 0X34
Charge is : 11 (XY) position is : 0X44
Hit number is : 2
IEEE 754 result is : 0X4211A72E
Float result is : 36.413261
This cluster finish
#####
Total cluster of this frame is : 2
This frame finish
    
```

(a)

0	0	0	0	0	0	0
0	7	0	0	0	0	0
0	0	13	14	0	0	0
0	0	34	257	10	0	0
0	0	13	21	0	0	0
0	0	0	0	0	0	0
0	0	0	0	0	0	0

(b)

0	0	0	0	0	0	0
0	0	0	0	0	0	0
0	0	0	18	11	0	0
0	0	0	30	0	0	0
0	0	0	0	0	0	0
0	0	0	0	0	0	0
0	0	0	0	0	0	0

(c)

Figure 4.26: Reconstructed results of a frame of raw data (a) The content of reconstructed results (b) First cluster shape (c) Second cluster shape.

4.3.1 Analysis and Discussion

500 frames of raw data for each given incident angle were collected to test the ANN implemented in the FPGA device. The raw data was also fed into the ANN implemented in the TMVA to produce and provide the reference result.

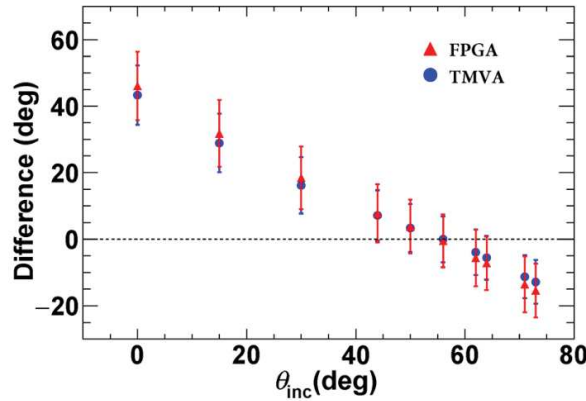


Figure 4.27: Difference between the mean value of reconstructed angles and the incident angle.

The difference between the mean value of reconstructed angles $\overline{\theta_{rec}}$ and the incident angle θ_{inc} (see formula (4-56)) is shown in figure 4.27, where the reconstructed angle generated by the ANN implemented in the FPGA is expressed in red and generated by the ANN implemented in the TMVA is plotted in blue.

$$\overline{\theta_{rec}} - \theta_{inc} = \frac{1}{n} \sum_{i=1}^n (\theta_{rec_i}) - \theta_{inc} , \quad (4 - 56)$$

where

n is the cluster counts of 500 frames for a given incident angle θ_{inc} .

θ_{rec_i} is the reconstructed angle of cluster i .

It can be found that angles reconstructed by two methodologies basically have the same mean value, which indicates that the ANN implemented in the software has been transplanted into the FPGA device. However, they are not identical and the result from the FPGA device present high-level value on the standard deviation. It is contributed by various reasons. For example, the data accuracy in the intermediate procedure of the FPGA device is not matched with the software. For the MCA module of the FPGA device, considering the resource and timing, the maximum standard deviation is

searched by rotating the angle φ at a step of 10 degrees, while in the TMVA, a relatively accurate value can be calculated by complex mathematical functions.

However, the difference between $\overline{\theta_{rec}}$ and θ_{inc} both for the FPGA and for the TMVA have not yet reached a precise level to make it possible to predict the real incident angle. Ideally, the difference between $\overline{\theta_{rec}}$ and the incident angle θ_{inc} should float near the X -axis ($y=0$). Firstly, the ANN structure needs to be trained by more raw data to optimize the number of hidden neurons. Then, four features used in the thesis may not be enough to present cluster information related to the incident angle. For example, replenishing a feature of the pixel number in the main axis. Finally, structures of the CPS can be optimized, such as the pixel pitch. With the decrease of the pixel pitch, the pixel density and resolution will be improved, differences among clusters generated particles with different incident angles will be easier and reconstructed results will be more accurate.

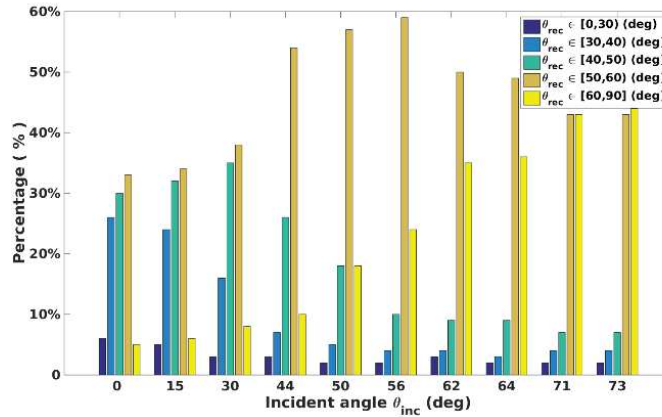


Figure 4.28: Distribution of reconstructed angles θ_{rec} versus incident angles θ_{inc} .

The distribution of reconstructed angles θ_{rec} by the ANN implemented in the FPGA device is shown in figure 4.28. As the incident angle θ_{inc} increases, the percentage of reconstructed angles θ_{rec} between 60 to 90 degrees increases and the percentage of reconstructed angles θ_{rec} between 30 to 50 degrees decreases.

The range of effective reconstructed angles that we concern is from 50 to 75 degrees. Firstly, cluster shapes generated by particles with incident angles below 50 degrees do not vary obviously. In addition, these incident angles can be directly reconstructed from hits information of a double-sided ladder [15]. On the other hand, due to the limitation of the 7×7 window, the ANN inputs extracted from the cluster exhibits similar features if the incident angle is above 78 degrees.

The percentage of large reconstructed angles increases and the percentage of small reconstructed angles decreases, as the incident angle increases. The variation of reconstructed angles has the same trend as that of incident angles. Before the optimization, the ANN cannot achieve reconstructing every high-precise incident angle, while significantly different distributions can be found in the figure.

4.4 Summary

The feasibility study for CMOS pixel sensors with on-chip artificial neuron networks was validated by an offline methodology.

An independent raw data acquisition system was established for hit information collection under different incident angles (total 10 incident angles). 500 frames were sampled for each given incident angle to test the performance of the ANN implemented in the FPGA device.

A FPGA development board was employed for the implementation of the preprocessing modules and the ANN. Main modules implemented in the FPGA device were described in detail. These modules will be improved for achieving into a CMOS pixel sensor. For example, the floating-point leads to some loss on data accuracy, the algorithm for cluster search implemented in the FPGA device occupy large resource and low efficiency, the feature extraction module can be achieved by some operators.

Reconstructed results by the FPGA device have been validated by result reconstructed by the ANN implemented in the TMVA. The feasibility study implemented in the FPGA provides the proof of the principle that tag particles according to the incident angle based on the ANN has been established. Even though the ANN did not achieve high-precise reconstruction as shown, reconstructed results present obvious same trend as the variety of incident angles. With the optimization of the ANN structure and more training processes, the performance of the ANN will be improved. Meanwhile, the decrease of the pixel pitch in fabrication will make the gap of the clusters generated by particles with different incident angles expand, leading to the precision improvement of the ANN.

4.5 Bibliography

- [1]. Hoecker, Andreas, et al. "TMVA-Toolkit for multivariate data analysis." *arXiv preprint physics/0703039* (2007).
- [2]. IPHC, "Test preliminaire de mimosa18"
- [3]. Dulinski, Wojciech, et al. "Beam telescope for medium energy particles based on thin, submicron precision MAPS." *2007 IEEE Nuclear Science Symposium Conference Record*. Vol. 2. IEEE, 2007.
- [4]. Maczewski, Lukasz. "Measurements and simulations of MAPS (Monolithic Active Pixel Sensors) response to charged particles-a study towards a vertex detector at the ILC." *arXiv preprint arXiv:1005.3710* (2010).
- [5]. Koziel, Michal. *Development of radiation hardened pixel sensors for charged particle detection*. Diss. Strasbourg, IPHC, 2011.
- [6]. Claus, G., et al. "A portable system for monolithic active pixel sensors characterization." *IEEE Symposium Conference Record Nuclear Science 2004*. Vol. 3. IEEE, 2004.
- [7]. <https://store.digilentinc.com/nexys-video-artix-7-fpga-trainer-board-for-multimedia-applications/>
- [8]. Jansen, Hendrik, et al. "Performance of the EUDET-type beam telescopes." *EPJ Techniques and instrumentation* 3.1 (2016): 7.
- [9]. Kahan, William. "IEEE standard 754 for binary floating-point arithmetic." *Lecture Notes on the Status of IEEE 754.94720-1776* (1996): 11.
- [10]. https://en.wikipedia.org/wiki/Single-precision_floating-point_format
- [11]. Landau, Lev Davidovich. "On the energy loss of fast particles by ionization." *J. Phys.* 8 (1944): 201-205.
- [12]. http://meroli.web.cern.ch/Lecture_StragglingFunction.html
- [13]. Ogasawara, Eduardo, et al. "Adaptive normalization: A novel data normalization approach for non-stationary time series." *The 2010 International Joint Conference on Neural Networks (IJCNN)*. IEEE, 2010.
- [14]. Manohar, T. Gowri, and VC Veera Reddy. "Load forecasting by a novel technique using ANN." *ARPN Journal of Engineering and Applied Sciences* 3.2 (2008): 19-25.

- [15]. Nomerotski, A., et al. "PLUME collaboration: Ultra-light ladders for linear collider vertex detector." *Nuclear Instruments and Methods in Physics Research Section A: Accelerators, Spectrometers, Detectors and Associated Equipment* 650.1 (2011): 208-212.

5 An On-chip Algorithm for Cluster Search

A CMOS pixel sensor with on-chip artificial neural networks (ANN) was proposed to tag and remove hits generated by particles coming from the beam background. As a part of the preprocessing module, implementation of cluster search is used to locate and collect cluster information. In order to meet requirements of the Application-Specific Integrated Circuit (ASIC) design, an on-chip algorithm for cluster search is proposed and analysed in the chapter.

Firstly, the motivation of the algorithm is expressed, the principle and detail steps of the algorithm are presented. Then, the algorithm extended for 256 columns is achieved by C code and simulated. Next, the algorithm is discussed for three examples of special cluster cases. Finally, the implementation of the algorithm is illustrated and analysed, power consumption and the occupied surface of the implementation are simulated.

5.1 Motivation

In the design of the CMOS pixel sensor with on-chip artificial neural networks, the module for cluster search is used to find out and collect cluster information from a frame of pixel charges. Then each piece of cluster information is fed into the module of feature extraction.

The module for cluster search implemented in the FPGA has been validated by

comparing to the design implemented in the Toolkit for Multivariate Data Analysis (TMVA). However, it is unacceptable to transplant the implementation in the FPGA device directly to the ASIC design. The main reasons are as follows:

1. Large storage resource

In the FPGA device, an entire frame of pixel charges has to be stored to seek the maximum pixel charge. For a frame of pixel charge from the MIMOSA 18, which means a 256×256 pixels array employing a 12-bit ADC for charge quantization, the required memory volume is $256 \times 256 \times 12$ bits (7.86×10^5 bits).

2. Data processing period

- **Slow:** In order to locate a seed pixel, all pixels are scanned and compared one by one to find out the maximum one, which means at least 256×256 clock cycles are required. The total processing period is proportional to the size of the pixel matrix.
- **Uncertain:** Just one seed pixel can be located for each time of scanning. However, the number of seed pixels in a frame is uncertain. The total processing period is related to the number of seed pixels in each frame.

Some algorithms for cluster search have been proposed and implemented based on FPGA device [1][2]. These algorithms can check the connective among pixels of a cluster, but it means low speed (process pixel by pixel). Considering requirements of the ASIC design, including power consumption, size and real-time performance, I proposed an on-chip algorithm for cluster search which can process pixel values in parallel.

5.2 Algorithm for Cluster Search

The algorithm is implemented following the column-level ADC in each column. Pixel charges are fed into the implementation row by row, then cluster information is located and collected. The scale of the implementation for cluster search is determined

according to the column number of the pixel matrix. For example, 256 same implementations of the algorithm need to be established for a 256-column CMOS pixel sensor.

In section 5.2.1, the principle of the algorithm is illustrated. In section 5.2.2, the algorithm is extended to 7 columns and detail steps of the algorithm is demonstrated based on an example of a 7×7 cluster.

5.2.1 Algorithm for One Column

Seed pixel selection is the first step for cluster search. For the algorithm proposed in this chapter, a seed pixel is defined as that it has the largest charge in a cluster window and is located in the centre of the cluster window (7×7 pixels). The principle to locate a seed pixel is :

1. If the charge of a pixel is not fewer than the charge of 3 pixels located above (see a1, a2, a3 in figure 5.1) and below (see b1, b2, b3) of it, respectively, it is a column seed pixel.
2. If the column seed pixel is not fewer than all the maximum pixel charge of columns located on the left (L1, L2, L3) and right (R1, R2, R3), respectively, it is a seed pixel.

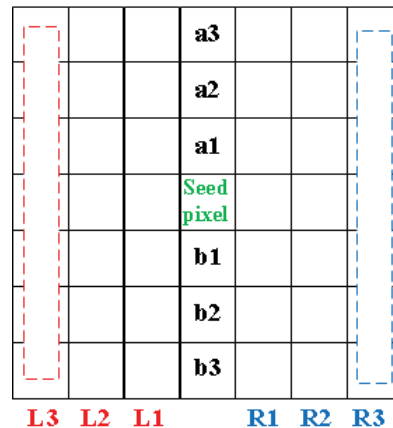


Figure 5.1: Definition of a seed pixel in a cluster.

The flowchart of the algorithm implemented in one column is shown in figure 5.2, where the cluster window is set as 7×7 pixels.

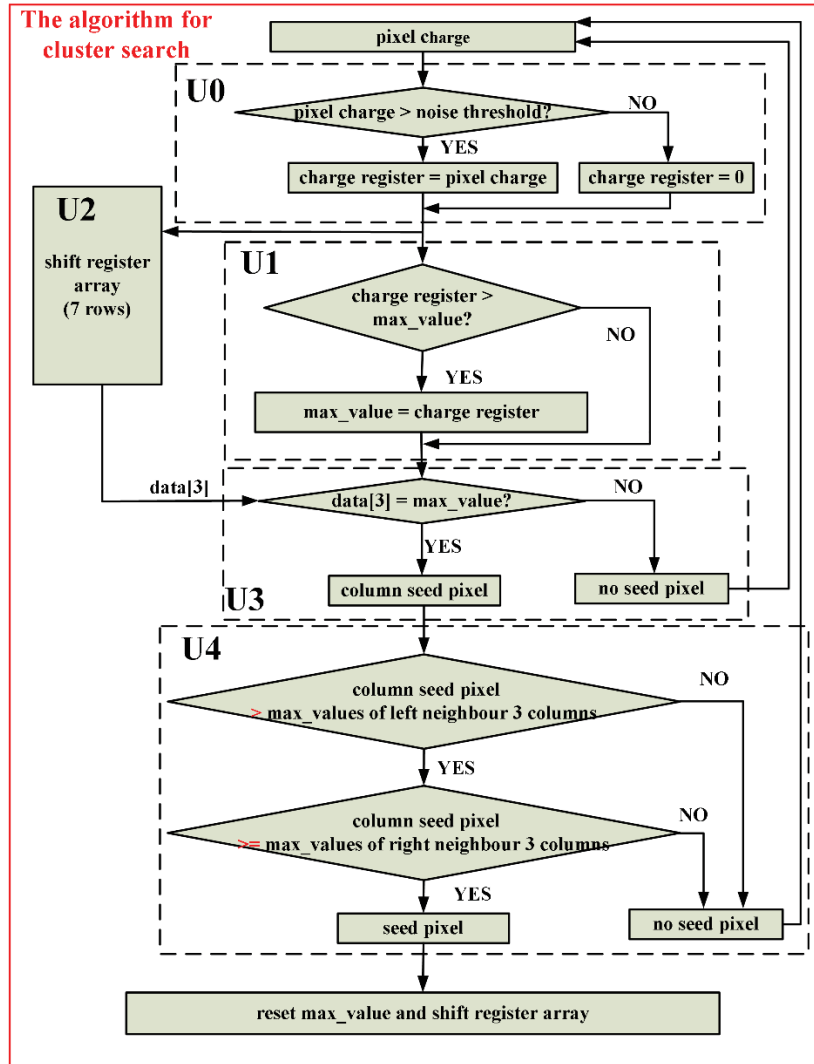


Figure 5.2: Flowchart of the algorithm proposed.

1. Filtering fired pixels by the noise threshold.

The process is implemented in module U0. A pixel charge, which has been processed by CDS, is read from the column-level ADC. If the pixel charge is larger than the noise threshold, it will be stored in a charge register as a fired pixel. Otherwise, the pixel charge will be dropped. The noise threshold provided by the raw data acquisition system is 5 ADC units, which corresponds to approximately twice the average noise of MIMOSA 18.

2. Finding a column seed pixel.

Pixel charges processed by the U0 are fed into U1 and stored in U2. U1 is composed of a max_value register which recorded the largest pixel charge in the last 7 pixels. U2 is a shift register array composed of 7 registers. Pixel charges stored in U2 are shifted row by row. The number of shift registers is determined by the size of the window. U3 is a comparator to compare the data [3] of U2 to the max_value register.

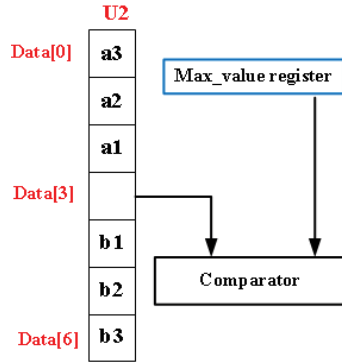


Figure 5.3: Comparison between the data [3] and the max_value register.

A column seed pixel is captured as follows:

- (1) **Recording the largest pixel charge.** The process is implemented in module U1. Register max_value is initialized as a seed threshold and updated when a larger pixel charge is fed into, in order to filter fake seed pixels.
- (2) **Finding the column seed pixel.** The process is implemented in module U3. In U2, the charge of the pixel in the middle position of 7 pixels of a column is stored in data [3] (from data [0] to data [6]). In U3, Data [3] is compared with the max_value register (see figure 5.3). Data [3] is asserted as a column seed pixel if it is equal to the max_value register, further of the algorithm is operated determine whether there is a seed pixel; otherwise, there is no seed pixel.

3. Finding a seed pixel.

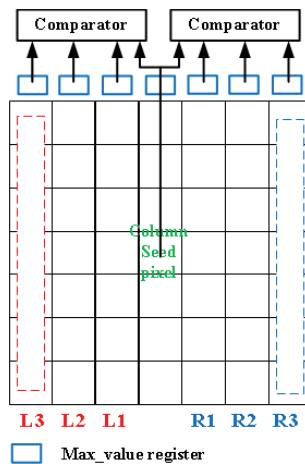


Figure 5.4: Comparison between the column seed pixel and the neighbour max_value registers.

In U4, the column seed pixel is compared with 3 max_value registers that are located on the left (L1, L2, L3) and right (R1, R2, R3), respectively (see figure 5.4). If its charge is larger than all 3 max_value registers in column L1, L2, L3 and not fewer than all 3 max_value registers in column R1, R2, R3, the column seed pixel is a seed pixel. A 7×7 cluster of centred on seed pixel is found. The max_value registers (blue boxes in figure 5.4) and the shift register arrays of the 7 columns are reset.

5.2.2 Steps for a Cluster

In the section, the algorithm for 1 column is extended to 7 columns and illustrated step by step through processing an example of a 7×7 cluster.

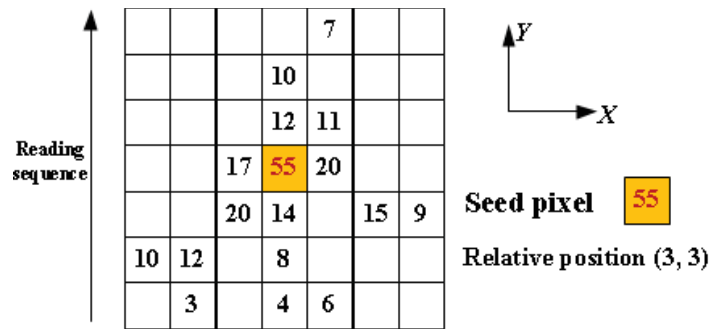


Figure 5.5: Information of an example cluster.

An example of a 7×7 cluster is shown in figure 5.5. The seed pixel remarked as the yellow has 55 ADC units and is located at the relative position of (3, 3). The cluster is fed into the algorithm from bottom to top row by row.

Detailed steps to find a cluster are shown in figure 5.6, where the noise threshold is set as 5 ADC units, and seed threshold is set as 12 ADC units. Pixel charges (12 bits) from column-ADCs are filtered by the noise threshold and then stored in "Charge register".

In figure 5.6, the max_value register of each column is presented as a blue box. It is used to store the maximum pixel charge of the shift register array of each column. The initial value of each max_value register is seed threshold (12 ADC units). It is updated according to the pixel charge reading from the charge register. The red number in the blue box means the max_value register has been updated.

In figure 5.6, 7 columns of shift register arrays are used to receive and store pixel charges from charge registers. A red number in data [3] of the shift register arrays means there is a column seed pixel, which has the same value as the max_value

register. The green number in the central position of the shift register arrays indicates a seed pixel.

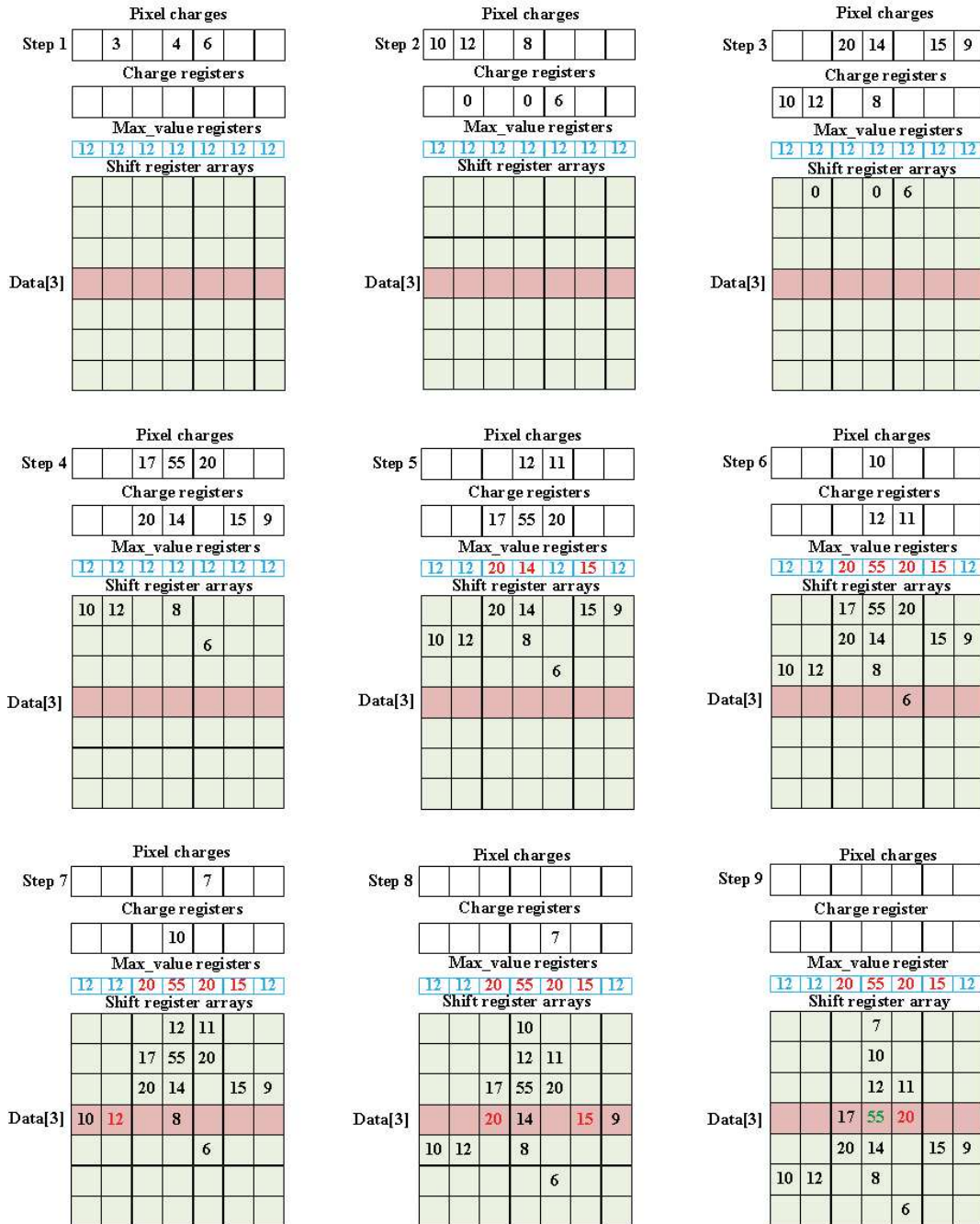


Figure 5.6: Processing steps of the example cluster.

Detailed steps of this algorithm for 7 columns are as follows:

Step 1, max_value registers are reset as the seed threshold, charge registers and shift register arrays are reset as 0. Pixel charges at the bottom row of the cluster are read in the module as the first row.

Step 2, charge registers are updated by comparing pixel charges of the first row

with the noise threshold. Just one charge register is updated as 6 ADC units and other pixel charges of the first row are fewer than the noise threshold.

Step 3, max_value registers and the first row of the shift register arrays are updated according to charge registers. Max_value registers do not be updated since all values are fewer than the initial value of max_value registers (12 ADC units). Then charge registers are updated by pixel charges of the second row.

Step 4, values stored in shift register arrays are shifted from top to bottom and the top row is filled by values of charge registers. Values of max_value registers are not varied. Then charge registers are updated by pixel charges of the third row.

Step 5, max_value registers of column [2], column [3] and column [5] are updated as 20 ADC units, 14 ADC units, 15 ADC units, respectively. In max_value registers (see blue boxes in figure 5.6), the number marked in red indicates that it has been updated.

Step 7, in shift register arrays, the pixel charge stored in data [3] of column [1] is recognized as a column seed pixel and marked in red. The pixel charge is equal to the max_value register. But it cannot be a seed pixel since it is not larger than 3 max_value registers of its left columns (L3, L2, L1).

Step 8, two column seed pixels are found in column [2] and column [5] and marked as red in shift register arrays. For the column seed pixel in column [2], its value (20 ADC units) is fewer than the max_value register (55 ADC units) of column R1 (column [3]), so it cannot be a seed pixel. It is the same explanation that the column seed pixel with 15 ADC units in column [5] is not a seed pixel.

Step 9, the pixel stored in data [3] of the column [3] marked in green indicates that it is a seed pixel. It is a column seed pixel as it is equal to the max_value register, and it is a seed pixel since it has the largest value compared with a total of 6 max_value registers of the left and right columns (L1-L3, R1-R3).

5.2.3 Supplementary Explanation

Two issues of the algorithm are explained in detail, charges of column seed pixels and two "seed pixels" in one cluster.

1. Charges of column seed pixels

As shown in step 7 of figure 5.6, data [3] of column [1] (12 ADC units) is a column seed pixel but it is not larger than the seed threshold (12 ADC units), and it is

not a seed pixel. In order to explain the correlation between the column seed pixel charge and the seed threshold clearly, three situations are presented and analysed.

- Column seed pixel charge < seed threshold (12 ADC units).

Impossible. A column seed pixel means that data [3] is equal to the max_value register. The minimum value of the max_value register is the seed threshold (12 ADC units).

- Column seed pixel charge = seed threshold (12 ADC units).

If the pixel charge stored in data [3] is 12 ADC and the max_value register keeps the initial value (12 ADC units). The pixel stored in data [3] is defined as a column seed pixel since it is equal to the max_value register.

However, it cannot be a seed pixel. The column seed pixel is defined as a seed pixel only if it is larger than all 3 max_value registers of left columns and not fewer than all 3 max_value registers in right columns. The minimum value of these six registers is 12 ADC units. The column seed pixel cannot be a seed pixel.

As shown in step 7 of figure 5.6, the pixel stored in data [3] of column [1] is recognized as a column seed pixel but not a seed pixel.

- Data [3] > 12 ADC units.

If the pixel charge stored in data [3] is equal to the max_value register, it is defined as a column seed pixel.

Meanwhile, if it is larger than all 3 max_value registers of left columns and not fewer than all 3 max_value registers of right columns, it is a seed pixel.

2. Two "seed pixels"

A seed pixel has the largest pixel charge compared with other pixels around it in the 7×7 cluster window. A pixel that has the same value as the seed pixel is allowed to be located in the first quadrant of a coordinate axis which is centred on the seed pixel. The case is shown and explained in two aspects according to the location of the pixel.

- The pixel located above (a1, a2, a3) the seed pixel.

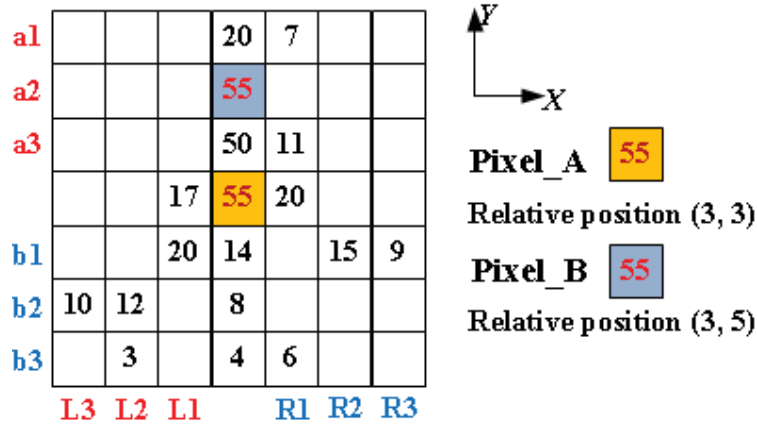


Figure 5.7: Two "seed pixels" in the same column, pixel A is the seed pixel, pixel B is a part of the cluster.

As shown in figure 5.7, an example of a 7×7 cluster has a seed pixel with 55 ADC unit. A pixel (pixel_B) located above the seed pixel has the same pixel charge.

The cluster is read in row by row from the bottom to the top. The pixel_A which is read in the algorithm firstly will be identified as a seed pixel, and the pixel_B read later will be recognized as part of the cluster. The seed pixel is determined according to the reading sequence if two or more pixels have the same value with the seed pixel in the column.

- The pixel located on the right (R1, R2, R3) of the seed pixel.

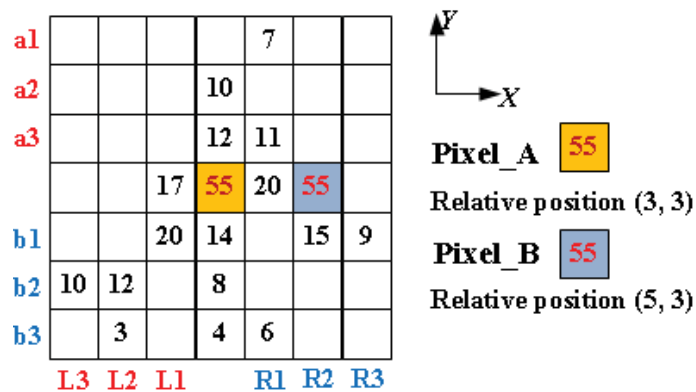


Figure 5.8: Two "seed pixels" in the same row, pixel A is the seed pixel, pixel B is a part of the cluster.

As shown in figure 5.8, an example of a 7×7 cluster has a seed pixel

with 55 ADC units. A pixel (pixel_B) located in the right has the same pixel charge.

According to the original definition of a seed pixel, it has to be larger than all 6 max_value registers of the left and right columns (L1-L3, R1-R3). There is no seed pixel in this 7×7 cluster window since the charge of pixel_A is not larger than the max_value register of column [5] which is also equal to 55 ADC units, the cluster would be lost by the definition. It is same for the pixel_B.

In order to prevent missing some clusters, the definition of the seed pixel is optimised and expressed in module U4 of the algorithm. A seed pixel is larger than 3 max_value registers of left columns (L1, L2, L3) and not fewer than 3 max_value registers in right columns (R1, R2, R3). According to the definition in the algorithm, pixel_A in the column [3] recognized as a seed pixel as it is not fewer than the pixel_B. Pixel_B in the column [5] cannot be recognized as a seed pixel since it is not larger than the pixel_A.

5.3 Simulation Results

In order to analyse the performance of the algorithm proposed in the chapter, the algorithm was extended for a 256-column input and achieved by the C code.

As described in chapter 4, 500 frames of raw data for each given incident angle (total 10 angles) were collected and preprocessed to test the ANN implemented in the FPGA. Matrices of pixel charges are also used to test the algorithm proposed in the chapter. Each frame of pixel charges is 256×256 pixels.

In the section, algorithms with different cluster windows, seed thresholds are simulated, and they are compared with the algorithm implemented in the FPGA device. The cluster count means the number of clusters found in 500 frames of pixel charges for a given incident angle

5.3.1 Cluster Windows

A cluster window is used to limit the maximum area of a cluster. It is necessary

for the algorithm proposed to define a seed pixel and collect cluster information. A seed pixel has the largest pixel charge in a cluster window instead of the whole 256×256 pixels matrix.

By the algorithm proposed, the range of incident angles that can be detected is proportional with the size of a cluster window. As shown in figure 4.11 and formula (4-21), the maximum incident angle that can be detected is 78.6 degrees by the 7×7 cluster window. The sharp increase at incident angle $\theta_{inc} = 50$ degrees has been explained in figure 4.16.

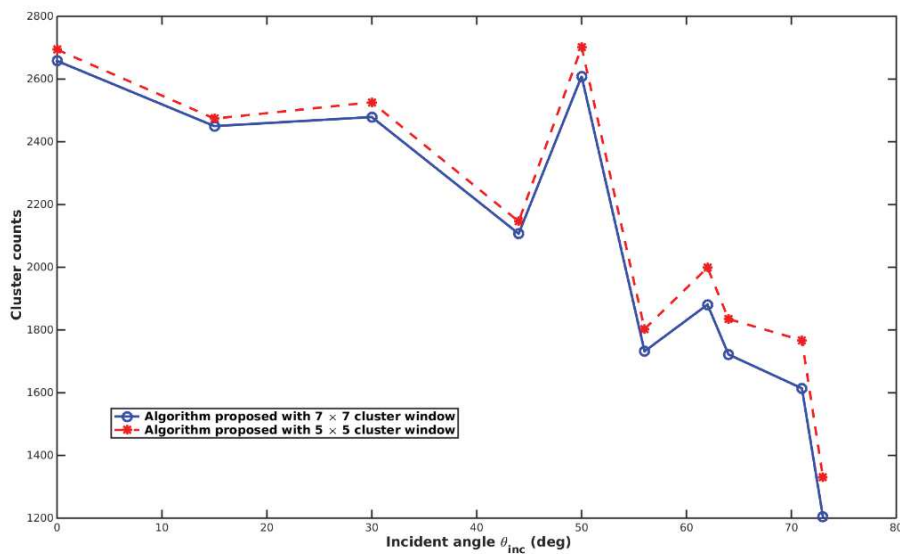


Figure 5.9: Simulation results of cluster counts found by algorithms proposed in this chapter with different cluster windows (7×7 and 5×5 cluster window).

Cluster counts found by algorithms with different cluster windows are shown in figure 5.9. It can be observed that cluster counts defined by different cluster windows (5×5 and 7×7 cluster window) [3][4] have the same variety trend. Cluster counts found by the two algorithms decrease as the incident angle θ_{inc} increases.

Cluster counts found by different cluster windows do not differ significantly for the incident angle θ_{inc} less than 55 degrees. As the incident angle θ_{inc} increases, more and more clusters owning elongated shapes appear. Some of the clusters between 5×5 pixels and 7×7 pixels are recognized by the 5×5 cluster window as two or more clusters. As shown in figure 5.9, the gap between the cluster counts of the two algorithms is expanded for a large incident angle.

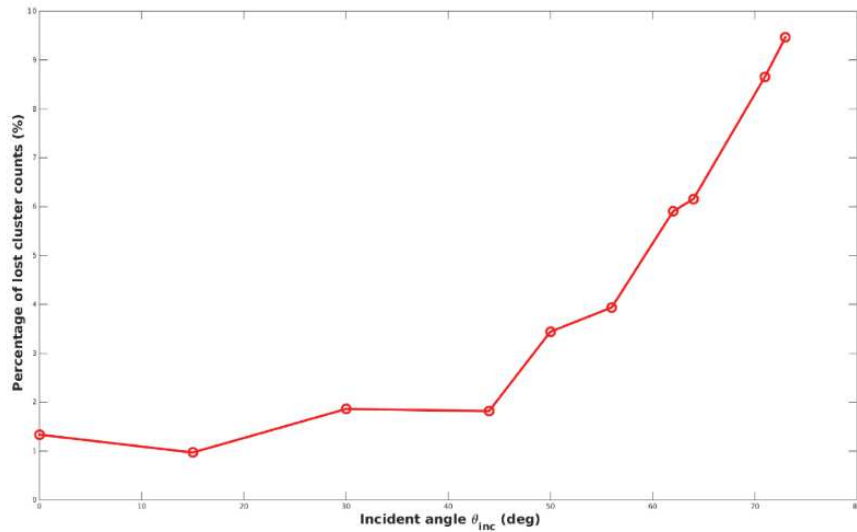


Figure 5.10: Simulation results of the percentage of lost cluster counts between algorithms with the 7×7 and the 5×5 cluster window.

In figure 5.10, the percentage of the gap between the cluster counts of the two algorithms is shown. There is just about 2% difference between cluster counts for the incident angle θ_{inc} less than 44 degrees. The percentage starts to increase significantly for the incident angle θ_{inc} larger than 50 degrees, even reaching 10% at 73 degrees.

The algorithm with the 5×5 cluster window needs less power consumption and hardware resources than the algorithm with the 7×7 cluster window. For instance, only 5 registers are needed to consist of one column of the shift register array.

The 7×7 cluster window used in the algorithm is chosen according to parameters of the CMOS pixel sensor (MIMOSA 18, $\sim 10\text{-}15 \Omega \cdot \text{cm}$). The algorithm with the small window means the reduction on the occupied surface and power consumption. It is possible for the implementation of the algorithm with the small cluster window with the development of CMOS technology. It is improved in aspects as following:

- Increase the resistivity of the epitaxial layer. Increase the resistivity of the epitaxial layer. Electrons generated can be more concentrated in the high resistivity epitaxial layer (MIMOSA 26, $\sim 400 \Omega \cdot \text{cm}$) [5].
- Expand the pitch of sensors. A larger pitch means that fewer pixels are needed to cover a given area.

5.3.2 Seed Thresholds

The seed threshold limits the minimum charge of a seed pixel. The number of

clusters is directly affected by the seed threshold. Seed thresholds of the algorithm are set at different levels to simulate.

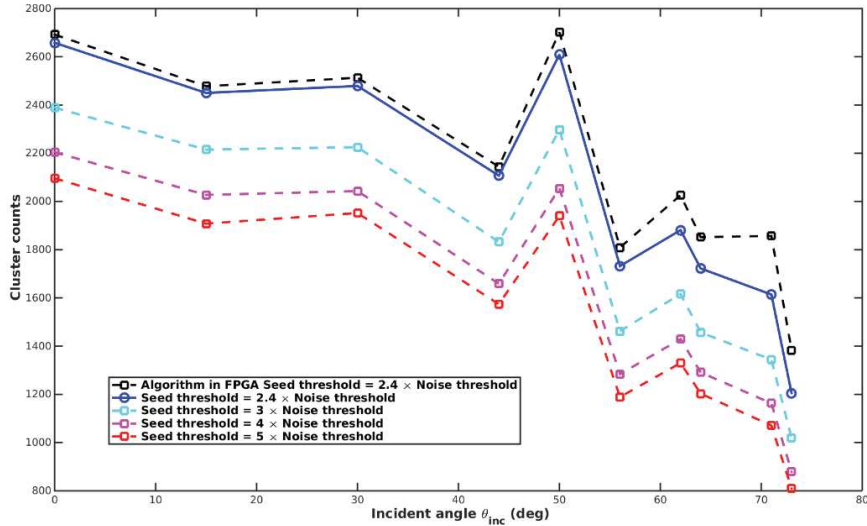


Figure 5.11: Simulation results of cluster counts by algorithms with different seed thresholds.

In figure 5.11, cluster counts found by algorithms with different seed thresholds ($2.4 \times$ noise threshold, $3 \times$ noise threshold, $4 \times$ noise threshold and $5 \times$ noise threshold) are presented, respectively. As the reference result, cluster counts found by the algorithm implemented in the FPGA (seed threshold = $2.4 \times$ noise threshold) is shown. Cluster counts by different seed thresholds have the same decrease trend with increasing the incident angle. It can be observed that, as the seed threshold increases, cluster counts decrease. Cluster counts have the most obvious decrease when the seed threshold increase from $2.4 \times$ noise threshold units to $3 \times$ noise threshold units.

5.3.3 Algorithm in the FPGA VS. Algorithm Proposed

The algorithm for cluster search implemented in the FPGA device has been validated by the design implemented in the TMVA. Main steps of the algorithm with the 7×7 cluster window are as follows:

1. Scanning pixel charges of a 256×256 matrix, finding out a seed pixel which has the maximum charge, and storing in a register array;
2. Erasing the seed pixel charge from the matrix;
3. Checking 8 neighbour pixels around the seed pixel in a 3×3 cluster window. Find fired pixels from the 8 neighbour pixels, store their relative positions and

- pixel charges in a register array;
4. Erasing these fired pixel charges from the matrix;
 5. Repeating step 3-4 around pixels stored in the register array until there is no new pixel or the search area exceeds the 7×7 cluster window²;
 6. Outputting this cluster information and reset the register array;
 7. Finding the next seed pixel in the 256×256 matrix, or read in the next matrix of pixel charges if there is no seed pixel.

As shown in figure 5.12, cluster counts by the algorithm proposed and the algorithm implemented in the FPGA device (with 7×7 cluster window and without cluster window) for each given incident angle are simulated. The algorithm without the cluster window means no limitation on the cluster size, the cluster is defined just by the connectivity between fired pixels and the seed pixel.

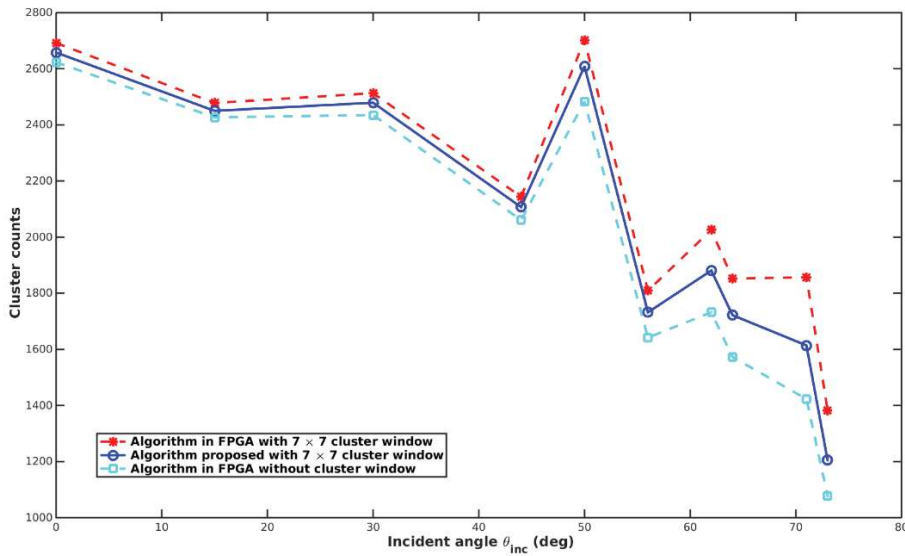


Figure 5.12: Simulation results of cluster counts found by the algorithm proposed VS. implemented in the FPGA device.

Cluster counts by these algorithms have the same trend. Due to the influence of the size change of the effective detection surface, cluster counts decrease as the incident angle increases.

There is no significant difference among cluster counts obtained by the three

² . For the algorithm without the cluster window, this step will stop only when there is no new pixel stored in the register array.

algorithms for the incident angle less than 55 degrees. As the incident angle θ_{inc} increases, especially larger than 55 degrees, cluster counts have a significant difference between the two algorithms implemented in the FPGA device. The number of clusters owning elongated shape increases with the growth of incident angle θ_{inc} . An elongated cluster defined by the algorithm without the cluster window will be recognized as two or more clusters by an algorithm with a 7×7 cluster window.

As shown in figure 5.12, the algorithm proposed reaches the same level of cluster counts as the other two algorithms. The algorithm proposed limits the cluster in a 7×7 area, leading to that its cluster counts are larger than those found by the algorithm without the cluster window. The algorithm proposed has no modules to check neighbour pixels of a seed pixel, leading to missing separated clusters located in one cluster window. These issues are discussed detailly in the next section.

5.4 Discussion

In order to make a deep understanding of the algorithm proposed and explain the difference between the algorithm proposed and the algorithm implemented in the FPGA further, these algorithms are discussed for three examples of special cluster cases, including large clusters, separated parts located in a cluster window and overlap parts of two clusters.

5.4.1 Large Clusters

Compared with the algorithm with the 7×7 cluster window implemented in the FPGA device, the algorithm proposed can reduce the possibility that one large cluster is recognized as two or more clusters.

5.4.2 Separated Parts

Due to no extra design to check connectivity among pixels, the algorithm proposed recognizes separated parts located in one cluster window as one cluster, leading to the reduction on cluster counts.

14				7		
15	18		10			
			12	11		
		17	55	20		
		20	14		15	9
10	12		8			
	3		4	6		

Figure 5.14: Example of separated parts in a matrix of 7×7 pixels.

An example of separated parts located in a 7×7 cluster window is shown in figure 5.14. In general, the example will be recognized as two clusters. One cluster composed of three pixels on the left top corner of this matrix. The other cluster is composed of a seed pixel (55 ADC units) and other fired pixels.

The two clusters will be found by two algorithms (without the cluster window and with a 7×7 cluster window) implemented in the FPGA device. The connectivity between fired pixels and the seed pixel as one of the conditions is taken into account to define a cluster.

By the algorithm proposed, only one cluster is found. The cluster contains a seed pixel (55 ADC units) and other all fired pixels in the matrix (including 3 pixels on the left top corner). Considering hardware resources and operation time of the algorithm, the design for detecting connectivity is dropped.

In fact, it is uncertain about the attribution of these three pixels located on the left top corner. They are recognized as an individual cluster since they are separated from the seed pixel. On the other hand, they are recognized as a part of the cluster if one or some blue pixels in the matrix have charges exceeding the noise threshold.

5.4.3 Overlap Parts

Due to the limitation of resources and the complexity of conditions, both the algorithm proposed and the algorithm implemented in the FPGA have no effective reaction on the parts overlapped by two cluster.

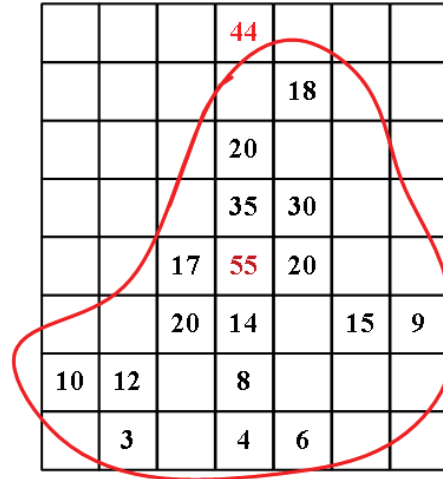


Figure 5.15: Example of overlap parts in a matrix of 8×7 pixels.

An example of the overlap part of two clusters is shown in figure 5.15. There are two seed pixels (55 ADC units and 44 ADC units) in the matrix of 8×7 pixels.

By the algorithm in the FPGA device without the cluster window, one cluster is found in the 8×7 matrix. The cluster is composed of a seed pixel (55 ADC units) and the other fired pixels, including the pixel marked with red (44 ADC units).

By the algorithm in the FPGA device with the 7×7 cluster window, two clusters are found. One cluster is composed of a seed pixel (55 ADC units) and other fired pixels. The other cluster is composed of a single pixel with 44 ADC units.

Two clusters are found by the algorithm proposed in the chapter. One cluster is composed of a seed pixel (55 ADC units) and the other fired pixels in the matrix (within the red line). The other cluster is a single seed pixel marked by red (44 ADC units). All pixels located between two seed pixels belong to the first cluster. In the algorithm proposed, only 7 rows of pixel charges are stored in the shift register array, the pixel located out of the size cannot be taken into account. In addition, the search result is related to the reading sequence, it makes totally different results if pixel charges are read from top to bottom of the matrix.

For the 7×7 cluster window, charges of these pixels located between these two

seed pixels should be allocated into two clusters based on values of the two seed pixels. However, it means additional hardware resources and power consumption to store more pixel charges and allocate overlap parts into two or more clusters. Considering the balance between the possibility and hardware resources, this situation would not be taken into account.

5.5 Algorithm Implementation

In the section, firstly, the implementation of the 64-column algorithm achieved by Hardware Description Language (HDL) is described. Next, Operation timing of the signals and data is illustrated. Then, the implementation of a 256-column algorithm achieved by C language is described and tested. Finally, the power consumption and occupied surface of the 64-column implementation are synthesized targeted at the TowerJazz 0.18 μm process.

5.5.1 Implementation of the 64-column Algorithm

The implementation of the algorithm proposed is based on modules of the 2^N -column matrix. An example structure of two 32-column ($N=5$) modules implemented for a 64-column input is shown in figure 5.16. Pixel charges are read in from 64 column-level ADCs row by row and then fed to the two 32-column modules. Each 32-column module has two levels (level 1 and level 2).

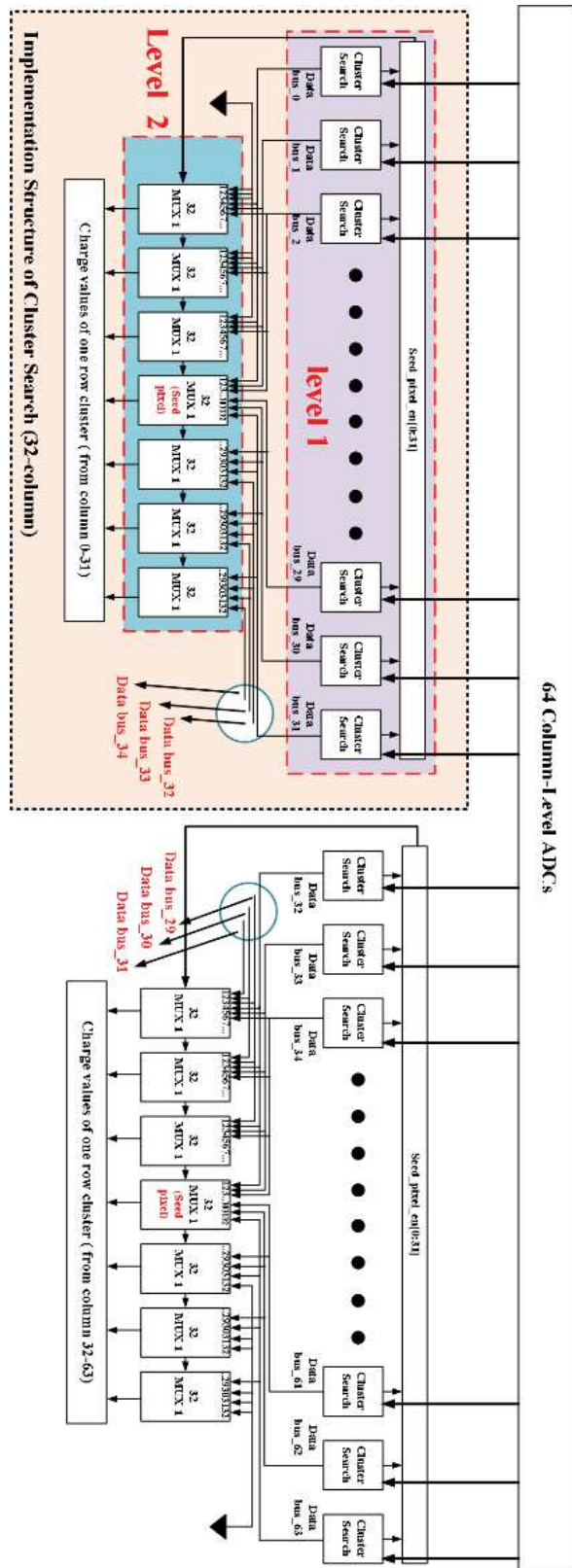


Figure 5.16: Schematic of the algorithm implemented in 64 columns.

Implementation of level 1

Level 1 consists of 32 cluster search units, each of which is the implementation of

the algorithm for cluster search proposed in the chapter. The pixel charge from a column-level ADC is fed into the unit and a signal named "seed_pixel_en" is outputted. A high-level pulse of one clock cycle will be generated on its signal "seed_pixel_en" if a seed pixel is found in the column.

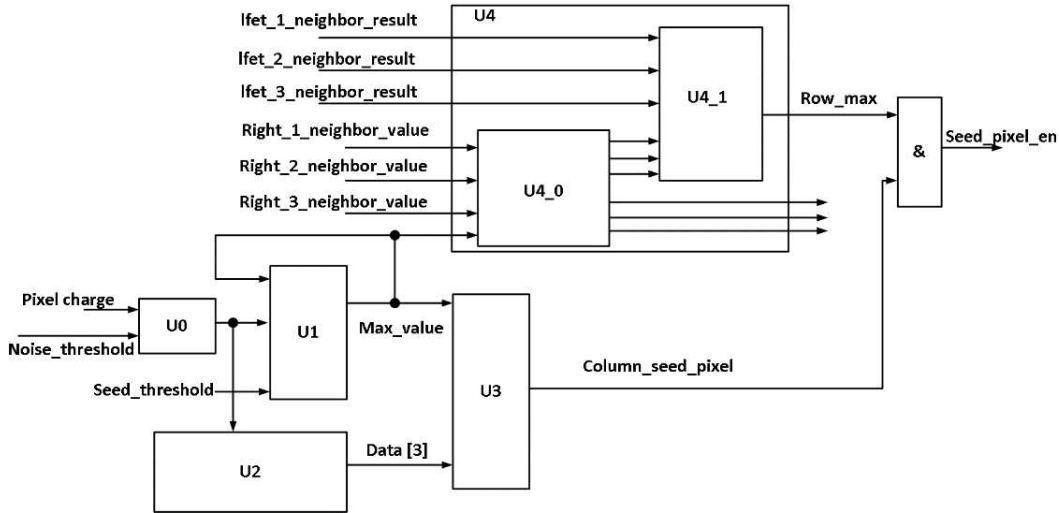


Figure 5.17: Implementation of the cluster search unit.

The implementation circuit of the cluster search unit is shown in figure 5.17. The input of the unit is the pixel charge. The noise threshold and the seed threshold are fixed in registers. The output of the unit is the signal “seed_pixel_en”.

The pixel charge is filtered by the noise threshold in U0, then inputted to U1 and U2. U2 is a register array that is used to store 7 consecutive pixel charges of a column. U1 is used to record the maximum pixel charge stored in U2.

In U3, the maximum pixel charge stored in U1 is compared with data [3] of U2. A column seed pixel is found if the maximum pixel charge is equal to data [3], then a pulse of one clock cycle will be generated on the signal "column_seed_pixel".

In U4_0, 3 max_value registers (“right_1_neighbour_value”, “right_2_neighbour_value” and “right_3_neighbour_value”) of right columns are inputted and compared with the max_value register of this column. 3 comparison results are outputted to U4_1. 3 comparison results (“left_1_neighbour_result”, “left_2_neighbour_result” and “left_3_neighbour_result”) between 3 max_value registers of left columns and the max_value register of this column are inputted. “AND” operation is applied among the six comparison results in module U4_1. The result of “AND” operation is equal to 1 if the max_value register of this column is larger than 3 max_value registers of the left columns and not fewer than 3 max_value registers of

right columns. Then a pulse of one clock cycle would be generated on the signal “row_max”.

If a pulse signal is simultaneously generated on the signal "row_max" and the signal "column_seed_pixel", a pulse of one clock cycle will be created on the signal “seed_pixel_en”, which means that the seed pixel is found.

Implementation of level 2

In theory, one module to collect 7×7 cluster information is required for each column, which means a total of 32 modules are needed following level 1. In order to reduce power consumption and the occupied surface, and considering the hit density in a matrix [6], an extra multiplexer array is implemented between the level 1 and collection modules resulting in that just one module for cluster collection is needed for 32 columns. As shown in figure 5.16, level 2 is a multiplexer array which is composed of seven (for the 7×7 cluster window) units of the 32-1 multiplexer. The 32-1 multiplexer at middle position is used to detect the seed pixel and collect pixel charges of the middle column of a cluster, and other 6 multiplexers are used to choose and collect pixel charges of left and right columns of the seed pixel (L1-L3, R1-R3).

In level 2, 3 additional data buses are connected with the ground at the left side. They are used to supply pixel charges of 3 left columns if signal “seed_pixel_en” of column [0] is active. It is the same for other 3 additional data buses on the right side of the right multiplexer array.

In level 2, 3 data buses at the right side are connected with data_bus_32, data_bus_33, and data_bus_34. They are used to supply pixel charges of 3 right columns if signal “seed_pixel_en” of column [31] is active. It is the same reason for connections between data_bus_29, data_bus_30, data_bus_31 and the right multiplexer array.

The case that a boundary pixel is also taken into account in the design of level 1. These designs guarantee to collect complete pixel charges of a cluster if a seed pixel is located at the boundary column of the pixel charge matrix.

5.5.2 Timing

In level 2, signals “seed_pixel_en” of 32 columns are received and scanned from left to right. In the case that pulses are detected on more than one signal “seed_pixel_en”

at the same time, the pulse of the column which is scanned firstly is chosen as a seed pixel, and the other pulses are abandoned.

In figure 5.18 shows an example of related signal waveforms when two seed pixels are found in the same row of 32 columns. "Column 4 input" and "Column 18 input" are pixel charges coming from column-level ADCs. Red numbers in these signals mean that there are two seed pixels in the two columns, one seed pixel charge is 40 ADC units and the other is 50 ADC units. Pulses on signals "Column 4 seed_pixel_en" and "Column 18 seed_pixel_en" mean that two seed pixels are found by level 1 at the same time. There are 4 clock cycles from pulses on signal "Column 4 input" to pulses on signal "Column 4 seed_pixel_en". The delay is used to search for seed pixels and generate pulses. Signals "Column output" is the output of a cluster search unit. The seed pixel in column [4] is chosen as a seed pixel. The seed pixel in column [18] is abandoned since the pulse on signal "seed_pixel_en" of column [4] is scanned firstly. A high-level pulse of 7 clock cycle is generated on signal "MUX_en" to read out cluster information when a pulse on the signal "seed_pixel_en" is detected.

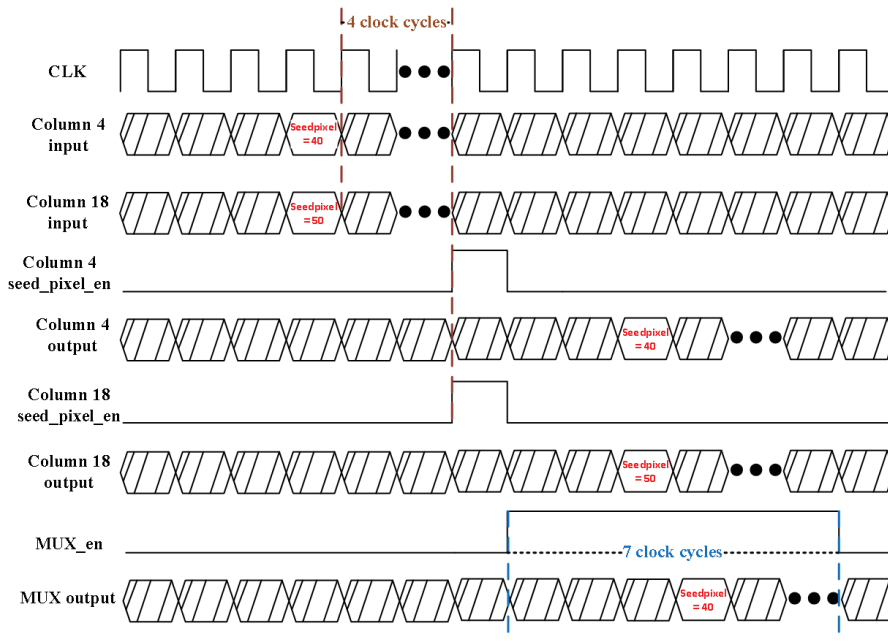


Figure 5.18: Timing of generating two seed pixels at one row.

New pulses will be abandoned if they are generated within the 7 clock cycles active time of signal "MUX_en". It means that new seed pixels cannot be collected if they are located within 6 rows away from the seed pixel which is outputted last time. The implementation of the multiplexer array affects the cluster count. It is simulated in the next section.

5.5.3 Simulation of the 256-column Implementation

Implementation of the 64-column algorithm with the multiplexer array is extended to 256 columns and achieved by C code. 500 frames of pixel charges for each given angle are fed into to simulate the design. In addition to modules of the 32-column matrix shown in figure 5.16, modules of the 16-column matrix and the 64-column matrix are also implemented for comparison. Cluster counts found by different modules are shown in figure 5.19. The implementation proposed without multiplexer refers to an ideal situation.

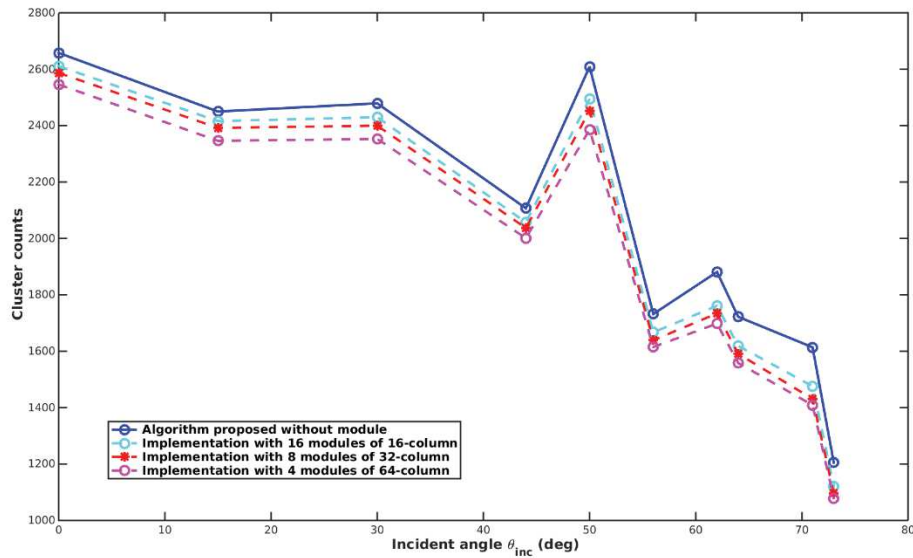


Figure 5.19: Simulation of cluster counts found by the algorithm with different modules.

Due to the influence of the read-out sequence and the reset control, there is a difference in simulation results between implementations with multiplexers and without multiplexer (the ideal situation). As shown in figure 5.19, for the incident angle larger than 50 degrees, the difference is extended as the more elongated clusters are generated in the matrix. By the design without multiplexer, an elongated cluster will be divided into two or more clusters that all are collected, by the design with multiplexers, just one seed pixel is allowed in one row of 32 columns (or 64 columns).

Cluster counts simulated decrease as the column number of inputs of a multiplexer module increases. As shown in figure 5.19, the cluster counts simulated with the module of the 64-column matrix is the least in simulation results. In fact, the implementation with modules of the 32-column matrix and the 7×7 cluster window

means that only one cluster can be collected in a pixel matrix of 10 rows by 32 columns. The implementation with modules of the 64-column matrix can collect one cluster in a pixel matrix of 10 rows by 64 columns.

5.5.4 Synthesized Result of the 64-column Implementation

The occupied surface and power consumption of the 64-column implementation (shown in figure 5.16) are synthesized using Cadence EDA tools targeted at the TowerJazz 0.18 μm process, as shown in Table 5-1. The column height (occupied surface) and the column power (power consumption) are average values. The column pitch is set to 50 μm .

Table 5-1: Simulation results of the occupied surface and power consumption of the 64-column implementation.

Window	Multiplexer	ADC (bits)	Clock (MHz)	Column height (μm)	Column power (mW)
7×7	16-1	8	100	200.58	0.85
		8	200	200.15	1.83
		4	100	102.86	0.46
		4	200	103.39	0.88
7×7	32-1	8	100	197.81	0.86
		8	200	197.24	1.77
		4	100	101.08	0.43
		4	200	102.24	0.88
5×5	32-1	8	100	159.39	0.68
		8	200	159.2	1.45
		4	100	81.56	0.37
		4	200	82.92	0.71
7×7	64-1	8	100	196.83	0.87
		8	200	196.09	1.76
		4	100	101.26	0.43
		4	200	101.63	0.9

As shown in Table 5-1. The occupied surface and power consumption can be

reduced if the 5×5 window is used instead of the 7×7 window. The trade-off between power consumption and search efficiency of the two designs, in addition, the comprehensiveness and accuracy of cluster information that is supplied to the MCA module, are considered in our design.

Both the occupied surface and power consumption can be reduced obviously if a low-frequency clock or a low-resolution ADC is employed. Almost the occupied surface and power consumption are reduced to about 50% if the ADC resolution is changed from 8 bits to 4 bits. Power consumption can be reduced to half if a 100 MHz system clock is taken instead of 200MHz, but no obvious difference is observed in term of the occupied surface.

In detail, the most power consumption of this design is devoted by shift register arrays, almost 50% in the design with the 7×7 cluster window. A shift register array needs to operate 7 times of data shifting per clock cycle. The design with the 5×5 cluster window contributes less power consumption than that with the 7×7 cluster window since fewer shift registers are needed store pixel charges.

There is no significant difference on the occupied surface (column height) and power consumption (column power) among implementations with modules of the 16-column matrix, the 32-column matrix and the 64-column matrix.

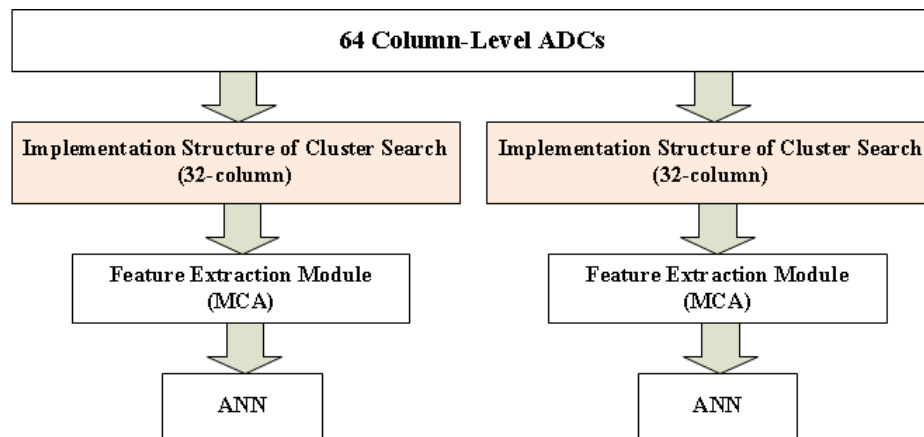


Figure 5.20: Schematic of MCA and ANN modules implemented for modules of the 32-column matrix.

However, considering the feature extraction (MCA) module and ANN module following the design of cluster search, more occupied surface and power consumption are needed if modules of the 16-column matrix are used in the implementation. As shown in figure 5.20, for a 64-column implementation, two feature extraction modules and two ANN modules are used for the design with modules of the

32-column matrix. Only one feature extraction module and one ANN module are needed if modules of the 64-column matrix are used in the implementation. Four times the occupied surface and power consumption are needed for the feature extraction module and the ANN module if modules of the 16-column matrix are used.

5.6 Summary

The algorithm for cluster search implemented in the FPGA device is impossible to transplant to the ASIC design since a lot of memory resource and operation time are needed. An on-chip algorithm for cluster search is introduced which can find seed pixels and locate clusters in a cluster window in real-time. The algorithm with different cluster windows and different seed thresholds are achieved by C code and simulated. Cluster counts found by the algorithm is compared with those found by the algorithm implemented in the FPGA device and reach the same level of cluster counts as the algorithm in the FPGA.

The algorithm can be integrated into the CMOS pixel sensor and executed in real-time. In the implementation of the algorithm, the multiplexer array is employed following the module of cluster search to reduce the power consumption and occupied surface of the MCA and ANN modules.

In the term of implementation, power consumption can be reduced by optimizing the control system. The power gating technology can be used to shut off the current of modules that are not used. The modules will be activated only when a seed pixel is found, a majority part of power consumption would be reduced since there are a few seed pixels in one frame.

5.7 Bibliography

- [1]. Johnston, Christopher T., and Donald G. Bailey. "FPGA implementation of a single pass connected components algorithm." *4th IEEE International Symposium on Electronic Design, Test and Applications (delta 2008)*. IEEE, 2008.
- [2]. Rosenfeld, Azriel, and John L. Pfaltz. "Sequential operations in digital picture processing." *Journal of the ACM (JACM)* 13.4 (1966): 471-494.
- [3]. Kohrs, R., et al. "First test beam results on DEPFET pixels for the ILC." *Nuclear Instruments and Methods in Physics Research Section A: Accelerators, Spectrometers, Detectors and Associated Equipment* 565.1 (2006): 172-177.
- [4]. Miho Yamada, "Development of Vertex Detector for ILC", *SOI Satellite Meeting*, Strasbourg, France May. 9th, 2017.
- [5]. Hu-Guo, Christine, I. P. H. C. Collaboration, and I. R. F. U. Collaboration. "Development of fast and high precision CMOS pixel sensors for an ILC vertex detector." *arXiv preprint arXiv:1007.2634* (2010).
- [6]. Strom, D. "Aspects of the sid detector design for the international linear collider." *Astroparticle, Particle And Space Physics, Detectors And Medical Physics Applications*. 2008. 511-520.

6 Conclusions and Perspectives

Conclusions

The International Linear Collider (ILC) is an e^+/e^- linear colliding experiment project that will allow studying extensively the Higgs Boson properties. It is foreseen to start commissioning phase about 2030. In order to meet high precision tagging requirements, especially for short lived particles, excellent vertexing system will be developed. One of the two detectors, the International Large Detector (ILD) will be equipped in the ILC. The vertex detector is located at the most inner layer to measure the primary interaction vertex and secondary vertices from decay particles under cooperation from other tracking detectors. For the last decade, CMOS pixel sensors, also named Monolithic Active Pixel Sensors (MAPS), proposed and extensively researched by the PICSEL group in IPHC, have been employed for charged particle tracking and imaging.

In the vertex detector of the ILC, a large amount of extra hits will be generated by electrons coming from the beam background. Momenta of these background electrons typically lie in the range of 10-100 MeV/c, which is lower than particles coming from physics events. Due to the effect of multiple scattering, in the multi-layer structure of vertex detectors in the ILD, challenges are obviously presented for track reconstruction of low momentum particles.

The thesis focused on the development of a CMOS pixel sensor with on-chip Artificial Neural Networks (ANNs) to tag and remove hits generated by background particles (typical low momenta). The existence of the magnetic field in the detector

leads to particles make helix paths. In addition, low momenta of particles lead to large incident angles with respect to the normal of the sensor planes. Considering the MAPS equipped in the vertex detector, when a charged particle traverses the epitaxial layer of the MAPS, electron-hole pairs are created by the ionization process (typical ~ 80 e-h/ μm). Electrons are collected by the collection diode of each pixel. Because of diffusion, electrons will be collected by several independent pixels. These independent pixels constitute a charge cluster which expresses hit information. Particles from beam background (typical low momenta) hit on the vertex detector, resulting in the generation of rather elongated cluster shapes.

Artificial Neural Networks (ANNs) are computational modules that are inspired by biological neural networks. Our group proposed to integrate ANNs into the CMOS pixel sensor for reconstructing the incident angle based on each cluster.

1. The implementation in a FPGA device.

For the feasibility study, preprocessing modules and the ANN structure have been implemented in a FPGA development board and validated by the ANN implemented in the TMVA. Both implementations are operated in an offline method, which means that procedures of data acquisition and process are separated.

A raw data acquisition system is established to collect raw data from an existing sensor MIMOSA 18, which is exposed under the illumination of β^- source ^{90}Sr . Incident angles of raw data can be varied by adjusting the angle between the system and the reference plane. Raw data was collected for each given incident angle (total 10 incident angles) to train weights of the ANN by the TMVA.

I implemented preprocessing modules and the ANN in a NEXYS VIDEO FPGA development board by Hardware Description Language (HDL). Raw data collected is fed into the FPGA device from PC frame by frame. In the FPGA, raw data per pixel (32-bit) is processed by the Correlated Double Sampling (CDS) to generate a 12-bit pixel charge. Preprocessing modules mainly contain cluster search and feature extraction. The cluster search module is used to find out seed pixels and locate clusters (7×7 pixels) in a frame of pixel charges based on each seed pixel. Feature extraction modules are used to produce features to represent a cluster.

The ANN module implemented in the FPGA device is a Multi-Layer Perceptron (MLP) structure. The input layer is composed of four input neurons for taking the cluster features into the network and one bias neuron. The four characteristics that were

selected are the total charge of a cluster and the charge of the seed pixel, the maximum and minimum standard deviations of charge distribution projected on an axis. These four features are processed by normalization then fed into the ANN to reconstruct the incident angle based on weights of the ANN. The hidden layer following the input layer has 14 calculation neurons and 1 bias neuron. The activation function used in the ANN is hyperbolic tangent.

In order to test the design implemented in the FPGA device, I have sampled 500 frames of raw data for each given incident angle. The raw data was fed into both the ANN in the TMVA and implementation in the FPGA device. Reconstructed angles are recorded and analysed.

Firstly, the feasibility study of transplanting the ANN design into hardware has been validated. Mean values of angles reconstructed by TMVA and FPGA basically are at the same level and show the same trend of the real incident angle. In addition, the distribution of angles reconstructed by the FPGA device (θ_{rec}) shows that as the incident angle of raw data increases, the proportion of large angles in the reconstruction results increase, while the proportion of small angles decreases. Reconstructed results present obvious same trend as the variety of incident angles and proof of the principle that tag particles according to the incident angle based on the ANN has been established.

Meanwhile, mean values reconstructed by TMVA and FPGA are not completely coincident, because of the difference in the data precision for hardware and software. For example, in the Main Analysis Component (MCA) module which is used for calculation of the maximum and minimum standard deviation, the lookup table design is employed to provide values of the trigonometric function. Taking into account the power consumption and processing time, the lookup table is at a step of 10 degrees, while precision trigonometric values are supplied in the software.

According to the distribution of reconstructed angle, designs both in the FPGA and the TMVA have not yet reached a precise level to predict the real incident angle, the ANN structure and the training procedure still need to be optimized.

2. An on-chip algorithm for cluster search.

The module for cluster search implemented in the FPGA device cannot be transplanted into the ASIC design directly. Firstly, a large number of memory resources are needed to store the entire one frame of pixel charges; secondly, lots of resources and time are needed to detect neighbour pixels. I propose an algorithm for cluster search. It

can be integrated into the CMOS pixel sensor and collect clusters in real-time.

Instead of searching seed pixels in a matrix pixel by pixel, the algorithm seeks a seed pixel in real-time in the read-in process of pixel charges row by row. The seed pixel is admitted by comparing with pixels located above and below it and with largest pixels located in the left and right columns of a certain window range.

I achieved the algorithm for 256-column by C code and simulated it. 500 frames of raw data for each given incident angle are used to test the algorithm. The simulation result shows that the algorithm reaches the same counting level as other algorithms including the algorithm implemented in the FPGA device.

A unit of cluster search algorithm was designed according to the algorithm described, which was implemented in each column of input. Consider the power consumption and occupied surface of feature extraction and ANN modules following cluster search modules, the implementation of the algorithm for multi-columns was optimized. I achieved the implementation based on the modulo of 2^N -column matrix, which means channels of feature extraction and ANN module are $input-column/2^N$.

I implemented the optimized design in a 64-column input and synthesis these implementations targeted at the TowerJazz 0.18 μm CMOS process. There is no significant difference among implementations with the modulo of 16-column ($N=4$), 32-column ($N=5$) and 64-column ($N=6$) in term of the occupied surface and power consumption. However, considering the feature extraction and ANN module following the implementation of cluster search, more occupied surface and power consumption are needed if the modulo of 16-column is used. The occupied surface and power consumption can be reduced if the 5×5 window is used instead of the 7×7 window. Both the occupied surface and power consumption could be reduced obviously if a low-frequency clock or a low-resolution ADC is employed.

The algorithm proposed can be integrated into the CMOS pixel sensor and executed on pixel charges row by row in real-time. Simulation results show that the algorithm achieves the consistent level on cluster counts with the algorithm for cluster search implemented in the FPGA. Meanwhile, the algorithm makes improvement on processing speed and reduction on the resource occupied. However, optimization and improvement on power consumption and the occupied surface of the implementation can be enhanced.

Perspectives

On the basis of the research of the thesis, the concept of a CMOS pixel sensor with on-chip artificial neural networks will be further studied from the following two aspects:

1. Optimize the ANN to improve reconstruction precision.

The concept of CMOS pixel sensor with on-chip artificial neural networks is validated by the ANN implemented in the FPGA device. However, neither of the two reconstruction results can reach the exact prediction level, compared with real incident angles.

More raw data will be acquired to retrained weights of the MLP structure used in the thesis in order to improve the reconstruction precision.

The ANN architecture can be optimized. For example, taking into account the trade-off between performance and resource of the design, more input neurons can be introduced to present features of a cluster as complete as possible. Correspondingly, the number of hidden neurons will also be adjusted accordingly. Even variety activation functions and hidden layers can be employed and analysed.

New High-Level Synthesis (HLS) tools will be employed for the implementation of the neural network. For example, the neural network structure is trained by TensorFlow in Python, the hardware implementation of the neural network is synthesized and optimized by Cadence Stratus HLS based on the module in Python. The tool increases the efficiency and reduces the complexity of the hardware implementation of a neural network.

2. Develop on-chip functional modules to realize the entire hardware design.

With respect to the implementation, some improvements can be carried out based on the fabrication process targeted in the thesis (0.18 μm).

On the aspect of design. For the design of cluster search, the timing control can be optimized to increase efficiency. For example, the application of power gating technology can be used to reduce power consumption. For the module of feature extraction, the implementation of the FPGA device is achieved by some intellectual property mathematical function module, especially for the calculation of maximum and minimum standard deviation. In order to reduce power consumption and improve the operation speed, on-chip algorithms for feature extraction will be studied and developed to integrate into the CMOS pixel sensor.

On the aspect of the material. The module of cluster search which is described in

chapter 5 is the first level preprocessing modules followed the column-ADC. Due to low resistivity of the epitaxial layer in the CPS (MIMOSA 18) which is used for raw data acquisition, large shapes of clusters are produced, and the 7×7 cluster window is employed. In CMOS pixel sensors equipped with the high resistivity epitaxial layer, cluster shapes generated by charged particles will be lessened to 5×5 even 3×3 cluster window, resulting in reduction on power consumption and occupied surfaces.

With the application of advanced fabrication processes (65 nm even 28 nm), contributions will be made on the optimization and improvement of the hardware implementation of the entire design.

A higher circuit density will be provided by the 65 nm fabrication process. The cluster search module and feature extraction module can be achieved in distributed units as integrated into pixels. The occupied surface of readout electronics will be optimized, and the processing speed will be improved. On the aspect of power consumption, the low power supply supported by the 65 nm fabrication process makes a reduction on power consumption of the design.

Cluster search implementation

Seed pixels are located by comparing pixels row by row by the algorithm described in chapter 5. However, by the advanced fabrication processes, comparators can be integrated into pixels to tag fired pixels and compare signals from neighbour pixels. All seed pixels and clusters in the pixel array will be extracted at the same time instead of row by row. Combining with the low hit density of charged particles on the pixel array, just comparators from a few pixels (fired pixels) are excited for cluster search, leading to reduction of power consumption.

With the application of high resistivity material of the epitaxial layer, windows for cluster search reduce to 5×5 pixels. A seed pixel can be located as follows:

1. Digital pixel charge processed by CDS of each pixel compares with the noise threshold to define all fired pixel;
2. Comparators of all fired pixels are activated to compare with the seed threshold to pick out possible seed pixels;
3. Comparators of these possible seed pixels are activated to compare with fired pixels in 8 neighbours;
4. If the pixel charge of a possible seed pixel is not fewer than its 8 neighbour pixels, it is the seed pixel of the 3×3 cluster window, otherwise, it is a fake seed pixel.

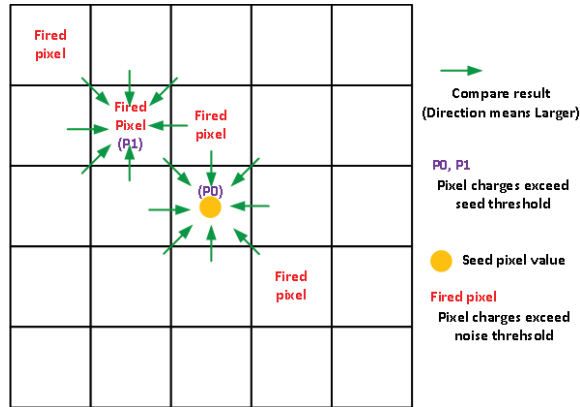


Figure 6.1: Schematic diagram of a seed pixel in a 3×3 cluster window. A cluster is composed of one seed pixel ($P0$) and 4 fired pixels. Two possible seed pixels ($P0$ and $P1$) are compared with their 8 neighbours in the 3×3 cluster window. Due to charge of $P1$ is fewer than $P0$, just pixel $P0$ is defined as a seed pixel in the 3×3 cluster window.

5. Release the seed pixel charge of the 3×3 cluster window into registers of fired pixels among its 8 neighbours to replace their charges and repeat step 4 for these fired pixels.
6. If all these fired pixels (seed pixel charge) are not fewer than charges of 8 neighbours around them, the seed pixel is upgraded as the seed pixel of a 5×5 cluster window.

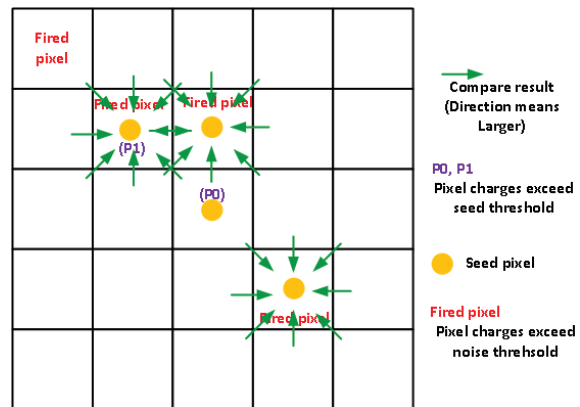


Figure 6.2: Schematic diagram of a seed pixel in a 5×5 cluster window. Charges of the 3 fired pixels in the 3×3 cluster window are replaced by seed pixel charge. Processed by step 4, charges of the fired pixels are larger than their neighbours, pixel $P0$ is extracted as the seed pixel in the 5×5 cluster window.

The pixel implementation of the algorithm is shown in figure, 6.3, ADC and comparators achieved in each pixel are omitted. In step1 and 2, 1 comparator is needed for identification of the fired pixel (noise threshold) and the possible seed pixel (seed threshold), respectively. The result of the comparison with the seed threshold

determines whether a comparator to neighbours is activated. In step 3, other comparators are for comparison between the possible seed pixel and 8 neighbour pixels. The 8 comparison results are processed “and” operation. In step 4, the pixel charge is chosen by mux 9-1 module and sent into comparators. In step 5, mux 9-1 modules of neighbour fired pixels are used to receive the seed pixel charge and sent to 8 comparators for step 6. The structure can be used for algorithms with different cluster window. For a 7×7 cluster window, just repeating the step 5 and 6 again.

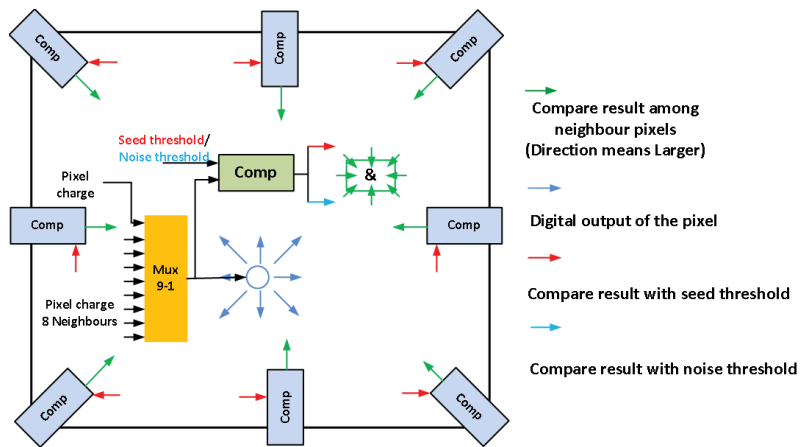


Figure 6.3: Schematic structure of a pixel for cluster search.

Feature extraction implementation

The MCA module implemented in the FPGA device is transplanted from the design in the software. However, MCA implementation which relies on trigonometric functions means low accuracy or large resource. For example, in software, the angle between the main axis of the cluster and the reference axis can be calculated. In the FPGA, a look-up table is implemented to find out the main axis of the cluster at a step of 10 degrees.

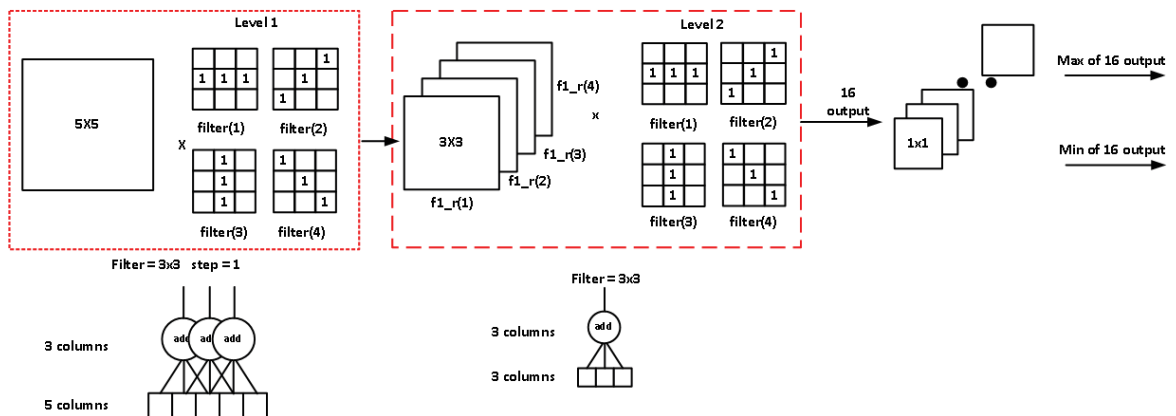


Figure 6.4: Steps of on-chip feature extraction.

Inspired by the technology of edge detection used in the image processing, such as the Sobel operator and the Canny operator, some operators can be optimized and applied for feature extraction and then implemented in ASIC design. Due to the concise structure, less power consumption and calculation units are needed.

As shown in figure 6.4, the implementation is processed based on each cluster. Firstly, four operators are flowed on a cluster (5×5) at a step of 1 pixel and make convolution, respectively. Four 3×3 submatrices are generated, then convolution processes are repeated on these submatrices. Finally, 16 values are created. The maximum and minimum value will be picked out to present features of a cluster. The 4 operators represent the direction and pixel values are summed along the direction after convolution. In the process of convolution, pixels closed to the seed pixel are taken into more times which means the high weight of the pixel. The program of the algorithm with a step of 2 pixels is illustrated on an example of 7×7 pixels as shown in figure 6.5.

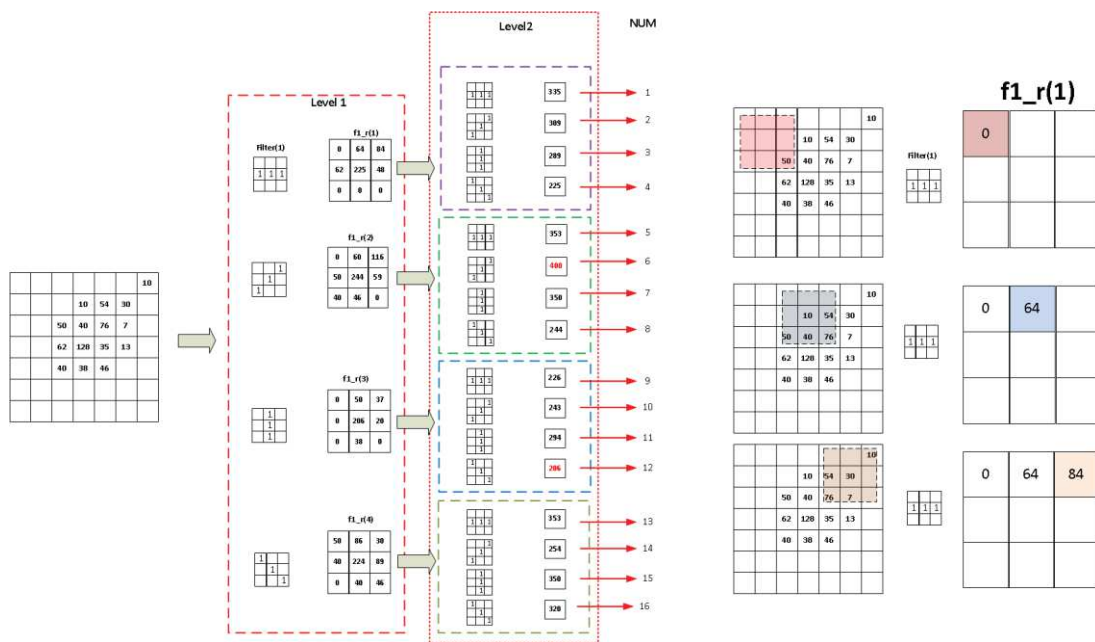


Figure 6.5: Example of on-chip feature extraction. The convolution operation is processed between the four operators and a cluster at a step of 2 pixels. Four submatrices are created and presented in level 1. The convolution operation is processed again between the four operators and these submatrices at a step of 1 pixel. 16 values are produced in level 2. Convolution procedures of three values in submatrix in level 1 is shown.

In addition, with the advanced fabrication processes, some complex artificial neural network structures can be attempted to implement, such as the Convolutional Neural Network (CNN). For the MLP structure used in chapter 4, four features extracted from a cluster (7×7 pixels) are fed into the network to present features of the

cluster. For the CNN, the cluster will be taken into the network as an image of 7×7 (or 5×5) pixels. Convolution and pooling operation will be processed by different layers of the network. With the development of the fabrication process and the 3D integration technology, implementing CNN structures on hardware becomes a possibility.

Furthermore, the training procedure which currently is accomplished in the software will be considered to migrate into the chip. The weight training and structure optimization will be processed on the chip, resulting in the CMOS pixel sensor with on-chip ANNs be portability and achieved in various structures according to the training dataset.

Development of a CMOS pixel sensor with on-chip artificial neural networks

Résumé

Dans le détecteur de vertex de l'ILC (International Linear Collider), un nombre élevé d'impacts supplémentaires seront générés par des électrons résultant de processus liés au bruit de fond des faisceaux. Leur impulsion se trouve typiquement est inférieure à celle des particules issues d'événements associés à des processus physiques. Notre groupe à l'IPHC a proposé d'explorer le concept d'un capteur à pixels CMOS avec des ANNs intégrés pour marquer et supprimer les pixels touchés (hits) générés par ces électrons.

Au cours de ma thèse de doctorat, je me suis concentré sur l'étude d'un capteur à pixels CMOS avec des ANNs intégrés portant sur les aspects suivants:

1. L'implémentation de modules de prétraitement et d'un ANN dans un composant FPGA pour l'étude de faisabilité;
2. Un algorithme pour la recherche de clusters, qui fait partie des modules de prétraitement, a été proposé en vue d'être intégré dans la conception de l'ASIC.

Mots-clés: Physique des Hautes Energies, Capteurs à Pixels CMOS, Réseaux Neuronaux Artificiels, FPGA, Recherche de Cluster

Résumé en anglais

In the vertex detector of the ILC (International Linear Collider), a large number of extra hits will be generated by electrons coming from the beam background. Momenta of these background electrons typically are lower than particles coming from physics events. Our group in IPHC has proposed the concept of a CMOS pixel sensor with on-chip ANNs to tag and remove hits generated by background particles.

During my PhD thesis, I focused on the study of a CMOS pixel sensor with on-chip ANNs from the following aspects:

1. The implementation of preprocessing modules and an ANN in an FPGA device for the feasibility study;
2. An on-chip algorithm for cluster search which is a part of preprocessing modules has been proposed to integrate into the ASIC design.

Keywords: High Energy Physics, CMOS Pixel Sensors, Artificial Neural Networks, FPGA, Cluster Search